1993

Suspended sediment concentration profiles in the bottom boundary layer

Jingping Xu
College of William and Mary - Virginia Institute of Marine Science

Order Number 9326237

Suspended sediment concentration profiles in the bottom boundary layer

Xu, Jingping, Ph.D.

The College of William and Mary, 1993

U·M·I
300 N. Zeeb Rd.
Ann Arbor, MI 48106

SUSPENDED SEDIMENT CONCENTRATION PROFILES IN THE BOTTOM BOUNDARY LAYER

A Dissertation

Presented to

The Faculty of the School of Marine Science

The College of William and Mary in Virginia

In Partial Fulfillment

Of the Requirements for the Degree of

Doctor of Philosophy

---

by

Jingping Xu

1993

APPROVAL SHEET

This dissertation is submitted in partial fulfillment of

the requirements for the degree of

Doctor of Philosophy

Jingping Xu

Approved, March 1993

L. Donelson Wright, Ph.D.
Committee Chairman/Advisor

John D. Boon, III, Ph.D.

Albert Y. Kuo, Ph.D.

Robert J. Diaz, Ph.D.

Ole S. Madsen, Sc.D.
Massachusetts Institute of Technology
Cambridge, Massachusetts

This thesis is dedicated with love to Jane and Lucy

TABLE OF CONTENTS

ACKNOWLEDGMENTS vi

LIST OF TABLES vii

LIST OF FIGURES viii

LIST OF SYMBOLS x

ABSTRACT xv

1. INTRODUCTION 2

2. METHODOLOGY AND DATA ANALYSIS 6

2.1 Introduction 6

2.2 Description of the research site 7

2.3 Instrument settings 11

2.4 Analysis of Hydrodynamics data 13

2.4.1 Derivation of u_c 13
2.4.2 Derivation of θ 14
2.4.3 Derivation of a_b, u_b and T 17

2.5 Preliminary analysis of the OBS data 17

3. A WAVE-CURRENT-SEDIMENT INTERACTION

BOUNDARY LAYER MODEL 24

3.1 Introduction 24

3.2 Governing equations 29

3.3 Eddy viscosity model 31

3.4 Solutions 36

3.4.1 About the continuity of the stability parameter 39

3.4.2 Solutions of current and mean concentration 40

3.5 The reference concentration model 47

4. BOTTOM ROUGHNESS UNDER WAVE-CURRENT-SEDIMENT INTERACTION ... 49

4.1 Introduction 49

4.2 Existing roughness models 50

4.3 Test of roughness models using field data 56

4.4 A new roughness model 63

5. EFFECTS OF STRATIFICATION AND SEDIMENT COMPOSITION

ON SUSPENDED SEDIMENT CONCENTRATION PROFILES 73

5.1 Introduction 73

5.2 Effect of stratification 74

5.3 Effect of sediment composition 76

5.4 Summary and discussions 92

6. REFERENCE CONCENTRATION AND SUSPENSION COEFFICIENT 105

6.1 Introduction 105

6.2 Computation of suspension coefficient 106

6.3 Results and discussions 107

6.4 Computation of γ_0 using the concentration of silt and clay 112

6.5 Summary 116

7. CONCLUSION 117

LITERATURE CITED 124

VITAE 131

ACKNOWLEDGEMENTS

I would like to thank my parents for making everything possible from the very beginning. I am grateful to Don Wright for his support, enthusiasm, and contribution to my scientific, as well as personal growth. It is hard to conceive of a better mentor and friend. Thanks go to each of my committee member for their time and efforts for the review of this thesis. I would like to thank Ole Madsen for providing inspirations, scientific guidance and pleasant humors. I would also like to thank John Boon, Al Kuo and Bob Diaz for their contributions to my education through their courses and many insightful conversations. Thanks also go to Jerome Maa for introducing me to numerical approaches and data acquisition instruments. I would like to acknowledge the help of Linda Schaffner, Suzette Kimball, Dan Hepworth and Woody Hobbs for their assistance. Special thanks go to Bob Gammisch and Frank Farmer, who made the field work successful by designing, building and maintaining the equipments. Finally, I would like to thank my wife, Jane, for her support and encouragement. This research was supported by Virginia Institute of Marine Science and the National Science Foundation, Marine Geology and Geophysics Grant OCE-9017828.

LIST OF TABLES

2.1 Input parameters used in the boundary layer model 18

2.2 Measured concentrations from the tripod 23

4.1 Output from the model 58

5.1 Composition of bed sediment at the Duck site 83

5.2 Compositions of two "synthesized" samples with skewed grain size distribution 99

6.1 Calculated suspension coefficient using mean grain size 108

6.2 Calculated suspension coefficient using silt and clay 114

LIST OF FIGURES

2.1 Location map showing the research site 8

2.2 Sketch showing shore-normal bathymetric profile 9

2.3 Under water camera images taken from bottom 10

2.4 VIMS instrumented tripod 12

2.5 Concept sketch of direction of current and wave propagation 16

2.6 Time series of: (a) burst-averaged OBS data; and
(b) rms near-bottom orbital velocity 21

2.7 Time series of corrected OBS data 22

3.1 Concept sketch of wave-current-sediment boundary layer 25

3.2 The three-layer eddy viscosity model by Madsen and Wikramanayake (1991) 32

3.3 Sketch of the continuous shear velocity 41

4.1 Calculated and measured concentration profiles under low energy condition 60

4.2 Calculated and measured concentration profiles under moderate energy condition ... 61

4.3 Calculated and measured concentration profiles under high energy condition 62

4.4 Examples of calculated velocity profiles under low, moderate and high
energy conditions 64

4.5 Calculated concentration profiles using the new roughness model, low energy 69

4.6 Calculated concentration profiles using the new roughness model,
moderate energy 70

4.7 Calculated concentration profiles using the new roughness model, high energy 71

4.8 Examples of calculated velocity profiles using the new roughness model 72

5.1 Comparison of neutral and stratified profiles, low energy 77

5.2 Comparison of neutral and stratified profiles, high energy 78

5.3 Profiles of stability parameter from 2 energy conditions 79

5.4 Histogram of 4 sediment sample from the Duck site 84

5.5 Calculated profiles showing the effect of sediment composition, low energy 87

5.6 Calculated profiles showing the effect of sediment composition, high energy 88

5.7 Profiles of equivalent settling velocity from 2 energy conditions 89

5.8 Percentage of each grain size plotted vs elevation 90

5.9 Profiles of percentage of all grain size classes 91

5.10 Calculated concentration profiles showing the combined effect (of stratification and sediment composition) under low and high conditions 94

5.11 Calculated profiles of equivalent settling velocity 95

5.12 Percentage of each grain size plotted vs elevation 96

5.13 Three different distributions of sediment 100

5.14 Effect of skewness on concentration profile, low energy 101

5.15 Effect of skewness on concentration profile, high energy 102

5.16 Effect of skewness on equivalent settling velocity profile, low energy 103

5.17 Effect of skewness on equivalent settling velocity profile, high energy 104

6.1 Calculated suspension coefficient using mean grain size 109

6.2 Calculated suspension coefficient using silt and clay 115

LIST OF SYMBOLS

a_b, A_b	Bottom excursion amplitude
B	Rouse number
B_i	Rouse number for each individual grain size
C	Suspended sediment concentration
$<C>$	Reynolds average of concentration
C_b	Bed sediment concentration (=0.65, volumetric)
C_m	Mean concentration
C_{mi}	Mean concentration for each individual grain size
$C_m(z_0)$	Mean concentration at elevation z_0
C_p	Periodic concentration
C_r	Reference concentration (=$C_m(z_0)$)
C_s	Measured concentration at elevation z_s
C'	Turbulent fluctuation of concentration
D	Mean water depth
d	Grain diameter
f_w	Friction factor
f_w'	Skin friction factor
g	Gravitational acceleration
h	Height above the reference elevation

h_{mo} Significant wave height

h_{tm} Thickness of sediment transport layer

i Index (i=1...N)

k Wave number

k_0 Deep water wave number

k_b Total bed roughness

k_{bd} Grain roughness

k_{bm} Sediment motion roughness

k_{br} Ripple roughness

L Monin-Obukhov length

L_c Monin-Obukhov length above wave boundary layer

L_{cw} Monin-Obukhov length within wave boundary layer

N Limit of index value

P Pressure

P_{atm} Pressure of atmosphere

P_c Pressure, current component

P_w Pressure, wave component

P' Turbulent pressure

<P> Reynolds average of pressure

P(t) Instantaneous pressure

q_t Sediment transport rate

s Relative sediment density

s_a Normalized excess shear stress

S_* Dimensionless fluid-sediment parameter

S_u^2 Variance of u_i

S_v^2 Variance of v_i

S_{uv}^2 Covariance of u_i and v_i

$S_{u'}^2$ Variance of u_i'

$S_w(\omega)$ Spectrum of bottom orbital velocity

t Time

T Wave period

T(t) Local wave period

u Velocity at East-West direction

$\bar{u}$ Burst average of u_i

$<u>$ Reynolds average of velocity

u' Turbulent velocity in East-West direction

u_b Near bottom orbital velocity

u_{bm} Maximum near bottom orbital velocity

u_c Mean current velocity

u_{cr} Mean measured velocity at the reference elevation z_{cr}

u_i Measured instantaneous velocity in East-West direction

u_* Shear velocity

u_{*c} Shear velocity above wave boundary layer

u_{*cw} Shear velocity within wave boundary layer

$\vec{u}$ Vector of velocity

$\vec{u}_c$ Vector of velocity, current component

$\vec{u}_w$ Vector of velocity, wave component

v	Velocity at North-South direction
$\bar{v}$	Burst average of v_i
v_i	Measured instantaneous velocity in North-South direction
w	Vertical velocity
w'	Turbulent vertical velocity
w_f	Settling velocity
w_{fi}	Settling velocity of each individual grain size
x	Coordinate, East-West direction
Z	Dimensionless parameter
z	Coordinate, vertical
z_0	Roughness length ($k_b/30$)
z_1, z_2	Elevations used in the eddy viscosity model
z_r	Reference height ($=z_0$)
z_a	Elevation at which C_a is measured
Δt	Sampling interval
α	Free parameter used in the eddy viscosity model
β	Empirical constant
γ	Empirical constant
γ_0	Suspension coefficient
δ_s	Sheet flow thickness
δ_w	Thickness of wave boundary layer
ε	Shear velocity ratio ($=u_{*c}/u_{*cw}$)
η	Ripple height

$\eta(t)$	Surface displacement
θ	Angle between current direction and wave propagation (Chapter 2)
θ	Dimensionless parameter (Chapter 4)
θ_c	Direction of mean current
θ_w	Direction of wave propagation
κ	von Karman constant
λ	Ripple length
ν	Kinematic viscosity of water
ν_t	Eddy viscosity in neutral flow
ν_{tm}	Eddy viscosity in stratified flow
ν_{ta}	Eddy diffusivity in stratified flow
ρ	Density of the mixture
ρ_s	Density of the sediment
ρ_w	Density of the water
σ_w	Variance of wave orbital velocity
τ_c	Critical shear stress
τ_{tm}'	Maximum skin friction shear stress
ψ_b	Break-off Shields parameter
ψ_c	Critical Shields parameter
ψ_m'	Maximum skin friction Shields parameter
Ω	Empirical constant
ω	Wave frequency ($=2\pi/T$)

ABSTRACT

Near-bottom suspended sediment concentrations and velocities were measured on the inner shelf off Duck, N.C. from late October to early November, 1991. This period embraced both fair and storm conditions. Four bottom roughness models are tested using field data together with a wave-current boundary layer model. Bottom roughness plays a significant role in calculations of sediment concentration profiles and current velocity profiles. The importance of each of the three parts in the roughness models (grain roughness, ripple roughness, and sediment motion roughness) vary depending on forcing conditions. A new bottom roughness model is established and tested. The calculated concentration and velocity profiles using the new roughness model compare well to the measured concentration and velocity profiles.

The effects of stratification and sediment composition on vertical profiles of current velocity and mean sediment concentration were also investigated. Stratification and sediment composition can have opposing effects. Since natural sediments always consists of multiple grain size components, the equivalent settling velocity is not a constant in the water column. The effects of multiple grain sizes on sediment concentration are more important in fair weather than in storms. Conversely, stratification is most effective during storms. Stratification damps the vertical turbulent transport of mass and momentum (reduces the turbulent eddy viscosity) and causes an increased shear in the current velocity profile. The limit above which stratification must be considered is represented by the stratification stability parameter ($z/L = 0.03$, where L is the Monin-Obukhov length).

The resuspension coefficient γ_0 was calculated from these data using a wave-current boundary layer model in association with two roughness models. The relation between γ_0 and excess shear stress reported by Drake and Cacchione(1989), Vincent et al (1991) (i.e. resuspension coefficient decreases when excess shear stress increases) was reproduced from using both the Grant and Madsen (1982) and the new roughness models. The decrease of γ_0 with increasing excess shear stress in that relation appears to be partially caused by the over-estimate of the sediment motion (movable bed) roughness and under-estimate of the resuspension coefficient when using the Grant and Madsen (1982) roughness model. The neglect of stratification and multiple grain size effects in the calculation of γ_0 may also be responsible for the decline in resuspension coefficient with increasing excess shear stress. When the fraction of silt and clay is used in calculating the γ_0 values, the γ_0 values show no trend of being a function of the shear stress.

Jingping Xu
Department of Physical Science
Virginia Institute of Marine Science
Thesis Supervisor: L. D. Wright, PhD
Title: Professor of Geological Oceanography
Virginia Institute of Marine Science

SUSPENDED SEDIMENT CONCENTRATION PROFILES IN THE BOTTOM BOUNDARY LAYER

1. INTRODUCTION

When wave and/or current shear stress reach a critical value, the movable sediments on the continental shelf are suspended into water column and then transported. The place where these processes take place is called bottom boundary layers. Boundary layer models based on mass and momentum conservation and diffusion theory have been developed for steady (current) flow (Dyer, 1983; Komar, 1976), for oscillatory (wave) flow (Jonsson, 1980; Nielsen, 1985; Kajiura, 1968; Trowbridge and Madsen, 1984a, 1984b), and for wave-current combined flow (Smith, 1977; Grant and Madsen, 1979, 1986; Madsen and Wikramanayake, 1991). Laboratory studies (Rouse, 1939; Vanoni, 1946; Smith, 1977) have shown that these boundary layer models can successfully describe the equilibrium vertical distribution of flow velocity and , only in current boundary layer, sediment concentration.

Sediment transport can be classified into suspended load and bedload modes. For each mode, there are normally two ways to model the sediment transport: (1) tractive models (Bjiker, 1971; Swart, 1976); and (2) energetic models (Inman and Bagnold, 1963; Bailard and Inman, 1981; Bailard, 1981, 1982; Bowen, 1981; Komar, 1971, 1977; Thornton, 1973). Energetic models relate the sediment transport rate to the flow power and sediment properties regardless what the sediment concentration profile and velocity profile are. Unlike the energetic models, the tractive sediment transport models calculate the vertical concentration profile and velocity profile and integrate the products of these two. This dissertation deals

with some crucial dynamics affecting the calculation of these two profiles.

In order to determine the magnitude of sediment suspension and transport, bottom shear stress must be obtained. Following the work of Kajiura (1964) and Jonsson (1966), bottom shear stress is estimated by relating the shear stress to the near-bottom orbital velocity (combined velocity in cases where currents are present) using a friction factor. Under the assumption of fully rough turbulent flow, this friction factor depends only on the relative bottom roughness which is defined as the ratio of the length scale of orbital motion at the bottom to the length scale of bottom roughness. Since the first length scale is normally given by the wave measurement and linear wave assumption, it is obvious that bottom roughness is the crucial parameter to be determined.

In a tractive model, the reference concentration must be determined before calculating the concentration profile. All reference concentration models (Yalin, 1977; Smith, 1977; Vincent et al, 1981; Shi et al, 1985) agree on a formula that relates the reference concentration to the excess shear stress through a constant suspension coefficient. However, dispute exists on how to define the reference height. Most investigators (Smith, 1977; Smith and McLean, 1977a, 1977b; Vincent et al, 1991) have used the reference height equal to the apparent hydraulic roughness length, i.e., total roughness divided by 30. But recently, it was claimed to be more appropriate to use a reference height equal to the thickness of the bedload layer (Kim, 1991; Mclean, 1992). Through a conceptual mechanics-based sediment transport model, Madsen (1991) derived a relationship by which the bedload layer thickness (the maximum vertical particle position) can be calculated. Wiberg and Rubin (1989) also derived an empirical formulation to estimate the bedload layer thickness. Madsen et al, (1993, in

press) used 7 times d_{50} as the reference height. Because of lack of general agreement on how to calculate the thickness of bedload layer, reference height is still assumed to be equal to the hydraulic roughness length in this study. The suspension coefficient is initially assumed to be equal to 2×10^{-3} but it is more closely examined later in this thesis.

Stratification and settling velocity, among others, are two important factors in calculation of sediment concentration and velocity profiles(Glenn and Grant, 1987; McLean, 1992). After sediments are suspended into the water column, the flow field can, under proper conditions, become stably stratified because of the density gradients created by the presence of suspended sediments. This stable stratification can inhibit the vertical turbulent diffusion of mass and momentum.

The effect of grain size distribution needs to be considered when the bottom sediments have multiple grain size composition. In natural sediments, there are always more than one grain size class. If one grain size, e.g., the mean or modal grain size, is used in the concentration profile computation, sediment concentration can be underestimated (McLean, 1992). This effect will be investigated in more detail using data from all weather conditions. Equivalent settling velocity profiles will also be calculated.

The objective of this study is to provide a more thorough understanding of sediment-transport-related properties affecting sediment concentration and flow field utilizing a combination of modeling and field data. In Chapter 2, the methodology and instruments are described. Data analysis used to obtain the input variables for the models described in posterior chapters are also presented. In Chapter 3, a wave-current-sediment interaction

boundary layer model, in conjunction with a combined boundary layer model by Madsen and Wikramanayake (1991) is introduced. This model provides a tool to calculate the dynamics used to compute the shear stress and flow and concentration fields. Chapter 4 discusses the existing roughness models and a new roughness model is proposed. These roughness models are tested using field data. A new roughness model is developed. In Chapter 5, effects of stratification and sediment composition (settling velocity) are examined and a qualitative relationship between these two effects is developed. In Chapter 6, the resuspension coefficient is studied using the new roughness model along with the boundary layer model and measured concentrations and velocities. Chapter 7 gives the conclusions which include: (1) a bottom roughness model; (2) effect of stratification and sediment composition on the profiles of velocity and suspended sediment concentration; and (3) the estimation of resuspension coefficient.

2. METHODOLOGY AND DATA ANALYSIS

2.1 Introduction

Two Virginia Institute of Marine Science (VIMS) instrumented benthic boundary layer tripods were deployed on the inner shelf off the U.S. Army Corps of Engineers Field Research Facility (FRF) at Duck, North Carolina from late October to November of 1991 (Figure 2.1). One tripod system consisted of a tripod frame supporting a Seadata Model 635 directional wave gage incorporating a pressure transducer and a single Marsh-McBirney 2-axis electromagnetic current meter, an array of five optical backscatterance sensors for measuring suspended sediment concentration, and a digital sonar altimeter. This tripod was deployed on the 8 m isobath. Another (more comprehensive) tripod system was deployed at 13 m. This system also supported a five-element optical backscatterance (OBS) array, a digital sonar altimeter and a Seadata Model 635 directional wave gage as well as three additional Marsh-McBirney electromagnetic current meters which permitted four-level velocity profiles to be obtained. The tripods were deployed from the R/V *Cape Hatteras* on 16 October 1991. A few days after the deployment, on 20 October, a typical autumn frontal system passed over the coast bringing northeasterly winds that generated a southerly setting current and waves with heights of 1.5 m and periods of 7 - 8 seconds. This moderate northeaster provided a valuable typical case for comparison with the more severe storm (the "Halloween Storm") that began on 26 October and eventually subsided on 1 November. The tripod deployed in 8 meter isobath was lost. The tripod at 13 meter was also broken up on the evening of 30

October. However, the uppermost portion of this tripod including broken sensors and cylinders containing data loggers washed ashore 3 km to the south of the deployment site on 2 November. The data from the Seadata Model 635 system were too badly corrupted to be useable and the digital sonar altimeter and its recorder were missing. The tape containing data from the other three electromagnetic current meters was intact and nearly full of high quality data. In addition, after treatment to remove a corrosive film caused by flooding of the OBS data logging canister, the magnetic disk containing the OBS data was made readable and all of the data were recovered. In this chapter, the general picture of bottom (sediment composition, roughness and bioturbation) is presented, the instrument settings, data (from the 13 meter tripod) acquisition and analysis are described.

2.2 Description of the research site

The Duck FRF site (36°11.1'N, 75°44.4'W) has been a place where many field experiments have been conducted (Mason, et al, 1987; Green, 1987; Kim, 1991; Wright, et al, 1986, 1991, 1992). The tripod in this study was deployed in 13 meters water depths. Shore-normal bathymetric profile shows that the inner shelf is concave upward over the region and the bathymetry is uniform alongshore (Green, 1987). Figure 2.2 shows a sketch of shore-normal bathymetry profile. The bed sediment at this site is composed of about 80% of fine to very fine sand and 20% of silts and clays. Both divers' observations and photographs from a profiling camera (Diaz and Schaffner, 1988) indicated the existence of ripples on the bottom at all times except when severe storms occur. Ripple lengths were 15 to 20 cm and ripple heights 2 to 5 cm (Figure 2.3). The user's guide to the FRF (Birkemeier, et al, 1985) shows the annual average significant wave height at the end of the Pier is 0.9 meters and the annual average peak period is 8.7 seconds. Waves are lowest from April to September, and

Figure 2.1 Location map showing the research site

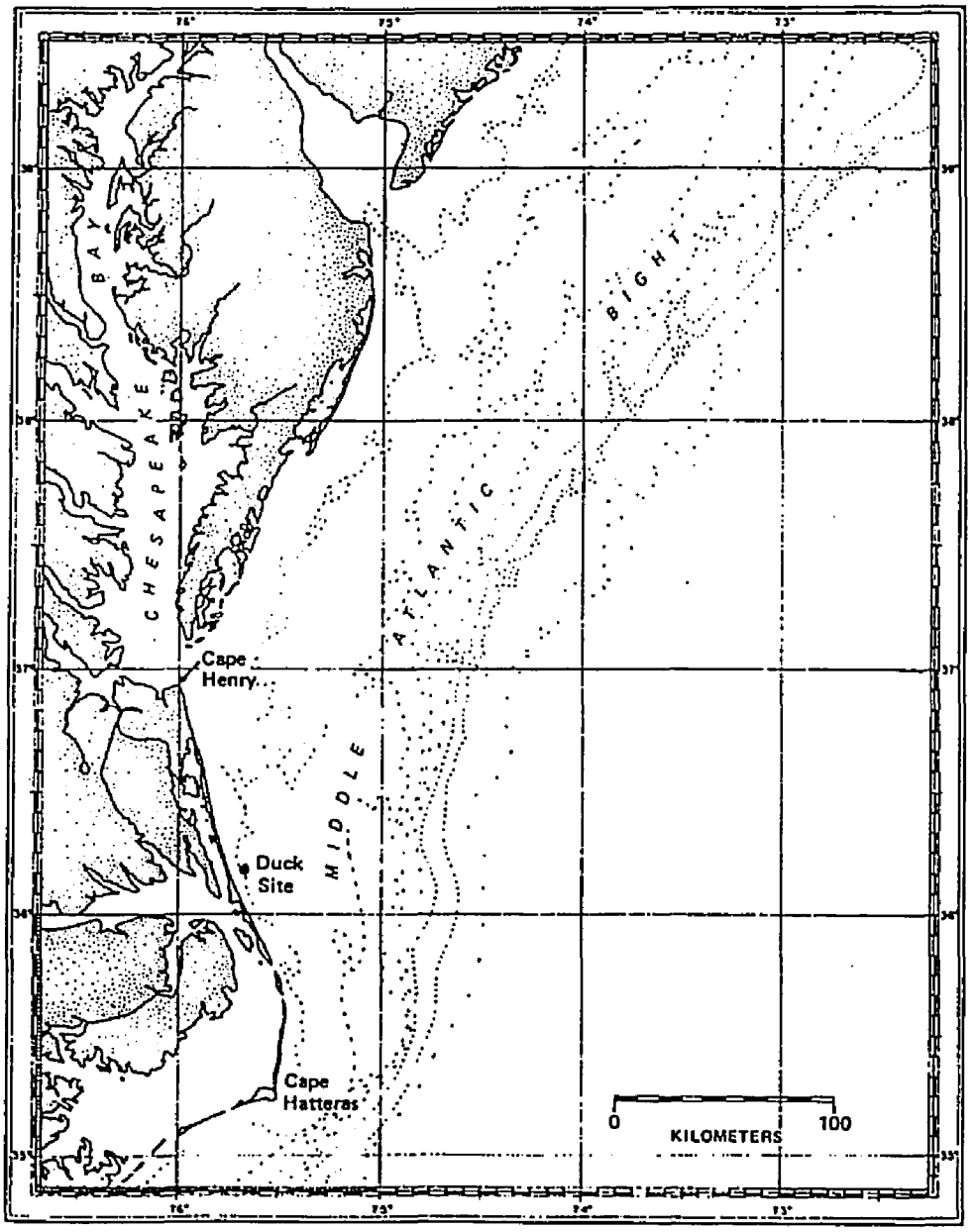
CHESAPEAKE BAY
MIDDLE ATLANTIC BIGHT
Cape Henry
Duck Site
Cape Hatteras
0
100
KILOMETERS

Figure 2.2 Sketch showing shore-normal bathymetric profile (Green, 1987)

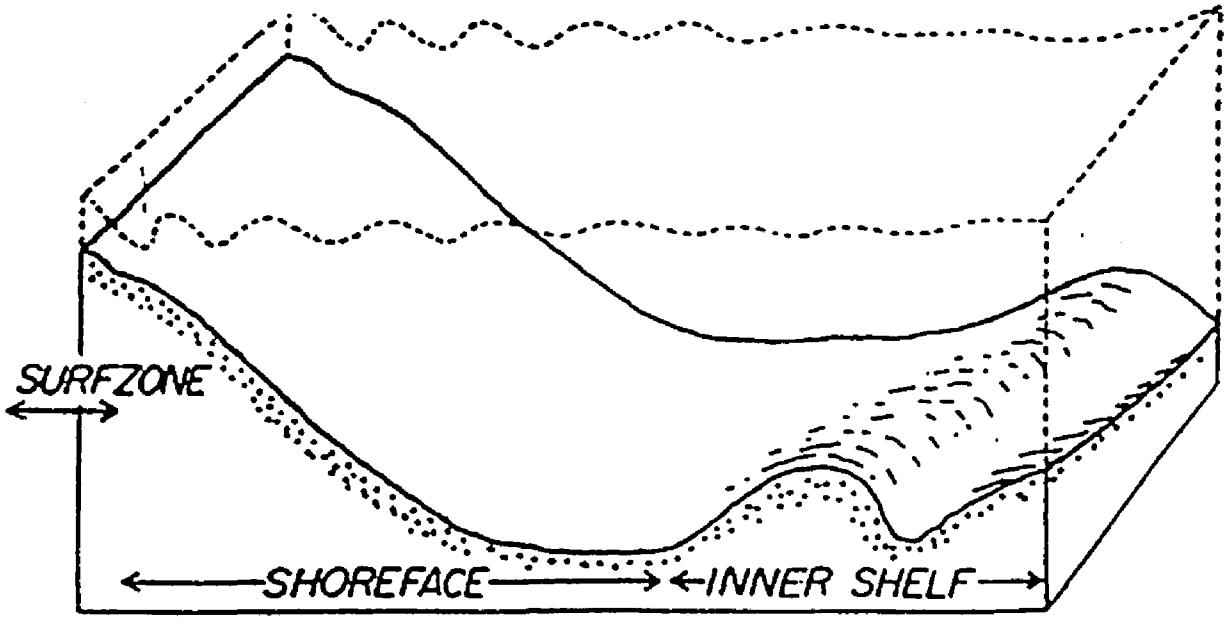
SURFZONE
SHOREFACE
INNER SHELF

Figure 2.3 Profile camera (A) and plan-view (B) images showing the ripples on bottom

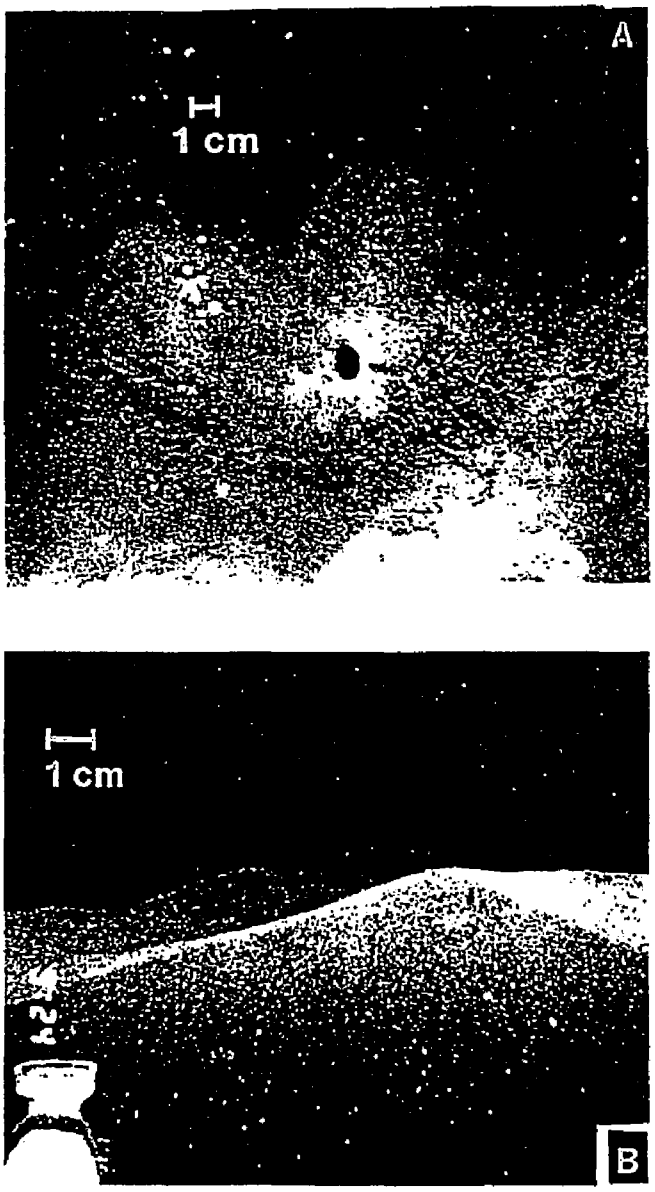
A
1 cm
1 cm
B

highest from October to December. Extratropical storms (Northeaster) or tropical cyclones may generate waves with significant heights in excess of 4 meters during the period October to February (Birkemeier, et al, 1981). Waves approach mainly from the South in spring and summer and North in Winter storm season. Extremely high waves are usually caused by the Northeast wind. Semi-diurnal tidal range averages 1 meter and 1.2 meters for spring tides (Birkemeier, et al, 1981) and shore-parallel near bottom tidal currents typically have speeds of 10 to 20 cm/sec (Wright, et al, 1991).

2.3 Instrument settings

The instrumented tripod was used to measure the time series of near-bottom oscillatory and mean flows and velocity profiles, suspended sediment concentration profiles and (sometimes) time-varying bed levels (bed erosion and accretions). The tripod used in this study (Figure 2.4) was similar to that described in Wright, et al, (1991, 1992). A tripod frame supports all the instruments. All of the electromagnetic current meters were 3.8 cm in diameter. Three of the current meters on the tripod were situated at elevations of 29, 87, and 124 cm; these sensors were logged by means of a Seadata Model 626 electronics package and were sampled at 1 Hz with a burst interval of 4 hours and a burst duration of 17 minutes. The fourth current meter (which was badly corrupted and not usable) in the array was part of the Model 635 package; it was situated at an elevation of 38 cm and sampled at 5 Hz. Five OBS-2 (Downing, 1985) sensors used to measure the suspended sediment concentration were located at elevations of 27, 54, 87, 120, and 147 cm respectively. Data from the OBS sensors were recorded at 5 Hz with a burst interval of 8 hours and a burst duration of 6.8 minutes by means of an ONSET Tattletale solid state logging system.

Figure 2.4 Benthic boundary layer instrumented tripod used in the study

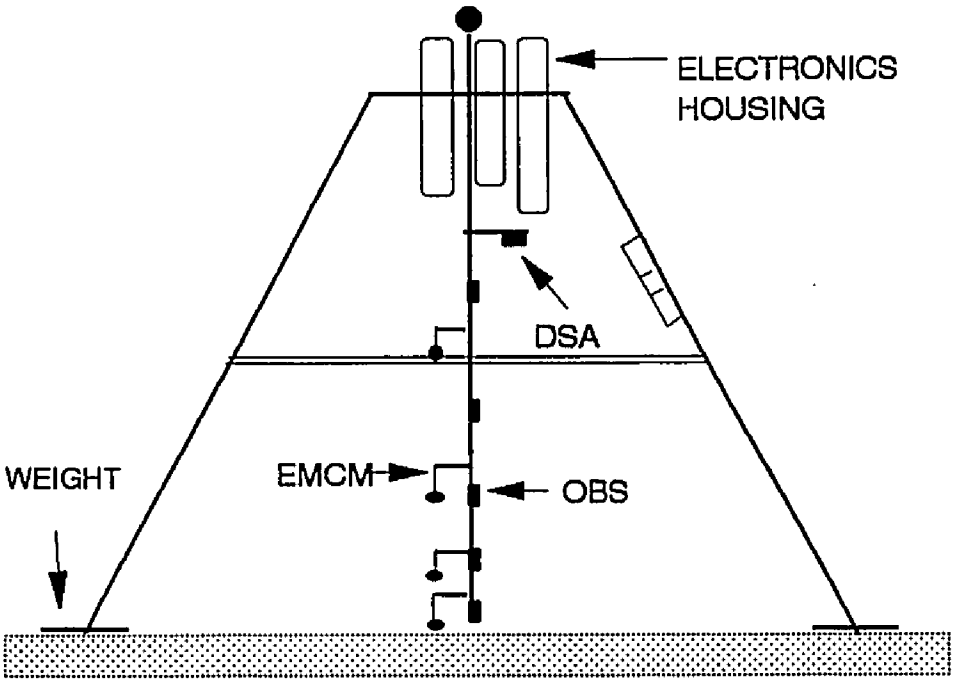
ELECTRONICS
HOUSING
DSA
WEIGHT
EMCM
OBS

Both current meters and OBS sensors were calibrated prior to deployment. The current meters were individually calibrated in steady flows before each deployment using a recirculating flume (Wright, et al, 1991). Native sediments from the field sites were used to calibrate the OBS sensors in a calibrating cylinder (Kim, 1991). Since previous experiences showed that only fine fractions of sediments ($>3.5\ \phi$) are found in the suspension most of the time, the OBS sensors were only calibrated using the fine fractions ($>3.5\ \phi$). Because larger grain size sediments, such as fine sand, could be lifted up into the water column during the storm, there is reasonable doubt about the validity of the OBS calibrations during the storm. This will be discussed later in section 2.5.

2.4 Analysis of hydrodynamics data

Five input parameters are needed to run the hydrodynamic boundary layer model which will be described in Chapter 3. These five parameters are (1) near bottom wave orbital velocity u_b; (2) wave period T; (3) reference current velocity u_{cr}; (4) reference height z_{cr}; and (5) the angle between wave propagation and mean current direction, θ. All the parameters, except z_{cr} which is equal to 124 cm in this study, are derived through procedures described below.

2.4.1 Derivation of u_c

Current time series were analyzed to determine the burst mean current velocity and direction. Readings from the two axes of current meters were rotated to the East-West (u) and North-South (v) components based on the reading of compass which was mounted to the tripod. Burst-averages of two rotated components provided the mean current velocity, u_c, and mean current direction, θ_c.

$$u_c = \sqrt{\bar{u}^2 + \bar{v}^2}$$

$$\theta_c = \arctan\left(\frac{\bar{v}}{\bar{u}}\right) \tag{2.1}$$

where

$$\bar{u} = \frac{1}{N}\sum_{i=1}^{N} u_i$$

$$\bar{v} = \frac{1}{N}\sum_{i=1}^{N} v_i \tag{2.2}$$

2.4.2 Derivation of θ

After knowing the mean current direction θ_c, the wave propagation direction θ_w must be determined in order to obtain the angle between the mean current direction and the direction of wave propagation. To determine θ_w, variances and covariance of u and v must be first calculated.

$$S_u^2 = \frac{1}{N-1}\sum_{i=1}^{N} (u_i - \bar{u})^2$$

$$S_v^2 = \frac{1}{N-1}\sum_{i=1}^{N} (v_i - \bar{v})^2 \tag{2.3}$$

$$S_{uv}^2 = \frac{1}{N-1}\sum_{i=1}^{N} (u_i - \bar{u})(v_i - \bar{v})$$

where S^2_u is the variance of u, S^2_v is the variance of v and S^2_{uv} is the covariance.

It is expected that variance in the direction of wave propagation is maximum. Therefore we can determine the wave propagation direction by rotating the coordinates counterclockwise

from u until the variance of the rotated East-West component, u′, reaches its maximum value. It can be proved that

$$S_{u'}^2 = S_u^2 \cos^2\theta' + S_{uv} \sin 2\theta' + S_v^2 \sin^2\theta' \tag{2.4}$$

where $S^2_{u'}$ is the variance of u′ and θ' is the rotated angle counterclockwise from the East (Figure 2.5). Differentiating equation (2.4) with respect to θ' gives

$$\frac{dS_{u'}^2}{d\theta'} = (S_v^2 - S_u^2)\sin 2\theta' + 2S_{uv}\cos 2\theta' \tag{2.5}$$

$S^2_{u'}$ can only reach its maximum value when the differential is equal to zero, i.e.,

$$(S_v^2 - S_u^2)\sin 2\theta_w + 2S_{uv}\cos 2\theta_w = 0 \tag{2.6}$$

under the condition that the differentiation of equation (2.5) with respect to θ_w is negative:

$$\frac{d^2 S_{u'}^2}{d\theta_w^2} = 2(S_v^2 - S_u^2)\cos 2\theta_w - 4S_{uv}\sin 2\theta_w < 0 \tag{2.7}$$

Then the wave propagation direction can be found when θ_w satisfies both equations (2.6) and (2.7) and, finally, θ can be obtained.

$$\theta = |\theta_c - \theta_w| \qquad |\theta| < \frac{\pi}{2} \tag{2.8}$$

Figure 2.5 Concept sketch of relation between direction of mean current and wave propagation

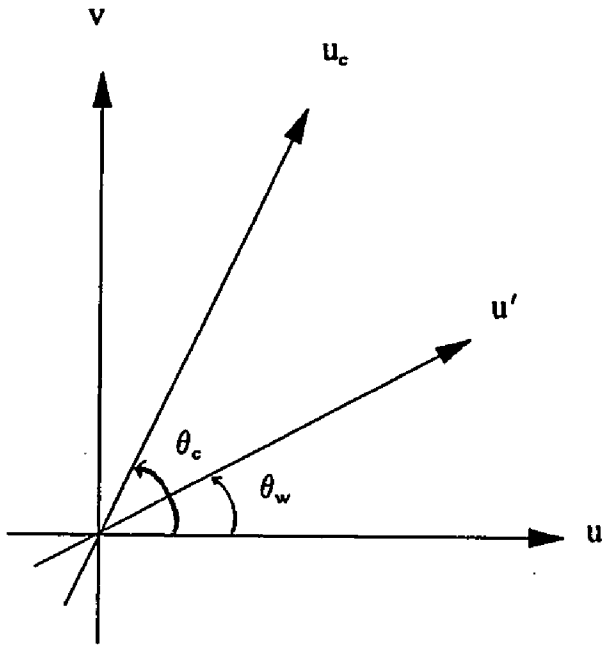
v
u_c
u'
θ_c
θ_w
u

2.4.3 Derivation of u_b and T

If the near-bottom velocity measurements are available, the near bottom root mean square wave orbital velocity can be estimated using

$$u_b = \sqrt{2}\ \sigma_w \tag{2.9}$$

where σ_w is the total variance of wave orbital velocity. The wave period T is evaluated using the zero-crossing of the time series of wave orbital velocity, which is the projection of u and v on the axis of the wave propagation direction (see Figure 2.5).

Ten bursts of hydrodynamics variables, which are going to be used in this study, are listed in Table 2.1. They are arbitraly categorized into three groups based on the value of the near-bottom root mean square orbital velocities. They are labeled as: (1) low energy condition, including Hr80 and Hr104; (2) moderate energy condition, including Hr248, Hr256, Hr264, and Hr272; and (3) high energy condition, including Hr296, Hr304, Hr312, and Hr320. Here, Hr0 is 0:00, 17 October 1991 and the first burst, Hr80 is 08:00, 18 October 1991.

2.5 Preliminary analysis of the OBS data

The time series of burst-averaged suspended sediment concentration measured using the OBS array on the tripod are shown in Figure 2.6a. As a companion, the time series of calculated root mean square near-bottom orbital velocity is plotted in Figure 2.6b. The time series plots start from 0:00 hours on 17 October 1991. From the first day of deployment, we see the OBS record is normally behaved till the end of the moderate northeaster storm. By 'normally behaved' we mean that the OBS records are responding to the shear stress (here measured by the near-bottom orbital velocity) properly and concentrations at lower elevations

Table 2.1 Input parameters used for the model .

	u_b	T	u_{cr}	z_{cr}	θ
Low energy	cm/s	sec	cm/s	cm	deg.
Hr 80	28.0	7.50	16.50	124	74.2
Hr 104	27.9	9.60	5.98	124	83.6
Moderate					
Hr 248	41.2	8.96	14.92	124	71.2
Hr 256	52.8	10.17	8.02	124	68.0
Hr 264	60.7	10.53	13.07	124	61.1
Hr 272	66.0	10.62	21.11	124	54.3
High					
Hr 296	102.4	9.90	6.16	124	20.4
Hr 304	95.1	9.60	29.90	124	82.5
Hr 312	103.8	10.20	44.20	124	82.4
Hr 320	108.6	11.50	31.70	124	83.5

are greater than those above. Prior to the northeaster storm, all OBS measurements showed zero concentrations in the water column for hydrodynamic conditions of $u_b < 15$ cm/s. Following this moderate northeaster storm, which showed the near-bottom orbital velocity as high as 35 cm/s, the hydrodynamic conditions returned to the low pre-storm level for 3 days. However, during the 3 low hydrodynamic condition days when the OBS records were expected to be zero, the OBS data showed a steady increase in burst-averaged suspended sediment concentrations. This behavior is probably the result of an electronic drift problem (Madsen, et al, 1993, in press). A common ground for the OBS was found to be defective upon recovery of the data logging canisters and therefore lends some credibility to this explanation of the drift exhibited by the OBS data. A linear drift with time is assumed in order to correct the OBS data by 'de-drifting' the raw data. First, a straight line is fitted from the OBS data during these three days, then the linear drift is removed from the subsequent OBS concentrations. The corrected OBS data is plotted in Figure 2.7. With the exception of the OBS sensor at 27 cm, the drift-corrected burst-average concentrations now make more physical sense.

As mentioned at the end of section 2.1, it is not certain if the OBS calibration, conducted using fine fraction ($> 3.5\phi$) sediment, can be used to convert from OBS sensor output, voltage, to suspended sediment concentration. In an independent study using the same storm data, Madsen, et al, (1993, in press) discussed this problem, i.e., the size-dependent response of OBS as follows. Assuming OBS response to be linear, the relation between OBS output voltage, V, and total concentration of sediment mixture, C, reads (Madsen, et al, 1993 in press)

$$V=\sum V_n=\sum b_n C_n=\sum (b_n f_n)C \tag{2.10}$$

where V_n is the partial voltage contributed by the *n*th size class whose fraction in the mixture is $f_n = C_n/C$ and has a size-dependent calibration constant b_n. Treating the sediment from the storm as composed of two size classes (n=1 for fines with grain size smaller than 0.09 mm (3.5 ϕ), a median diameter of d_1=0.04 mm, and a fraction f_1=0.36 in the bottom sediments; n=2 for the coarse fraction of median diameter d_2=0.12 mm) separate calibrations showed $b_1/b_2 = 5$, i.e., a pronounced size-dependency as suggested by previous investigators (Ludwig and Hanes, 1990; Green and Boon, in press). Introducing these results in equation (2.10) gives

$$V=b_1\left(f_1+\frac{b_2}{b_1}f_2\right)C \tag{2.11}$$

which shows that a reasonable estimate (accurate to within 10%) of total concentration of suspended sediment, C, may be obtained from our OBS voltage output by using the calibration, b_1, obtained from the fine fraction if the fraction of coarse sediment, f_2, is less than 0.1. Madsen, et al (1993, in press) showed that f_2 was indeed smaller than 0.1 for all 5 OBS sensors used in this study and concluded that reasonable estimates of burst-averaged suspended sediment concentrations could be obtained as recorded at the five OBS elevations by simply using the sensor calibration obtained for the fine fraction sediments. This conclusion is borrowed and no further action is taken in dealing with the conversion of voltage to concentration. Table 2.2 lists the 10 bursts of measured suspended sediment concentrations.

Figure 2.6 Time series of (a) burst-averaged OBS data and (b) root mean square near-bottom orbital velocity. Plots start from 0:00 hours 17 October 1991.

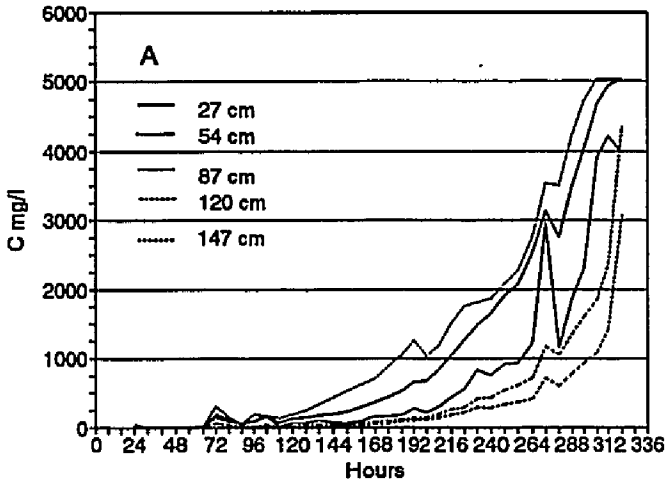
A
27 cm
54 cm
87 cm
120 cm
147 cm
C mg/l
6000
5000
4000
3000
2000
1000
0
0 24 48 72 96 120 144 168 192 216 240 264 288 312 336
Hours

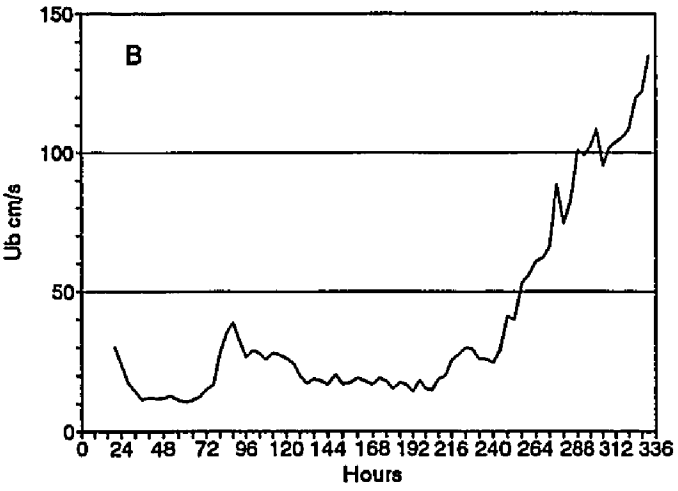
B
Ub cm/s
150
100
50
0
0 24 48 72 96 120 144 168 192 216 240 264 288 312 336
Hours

Figure 2.7 Time series of corrected burst-averaged OBS data.

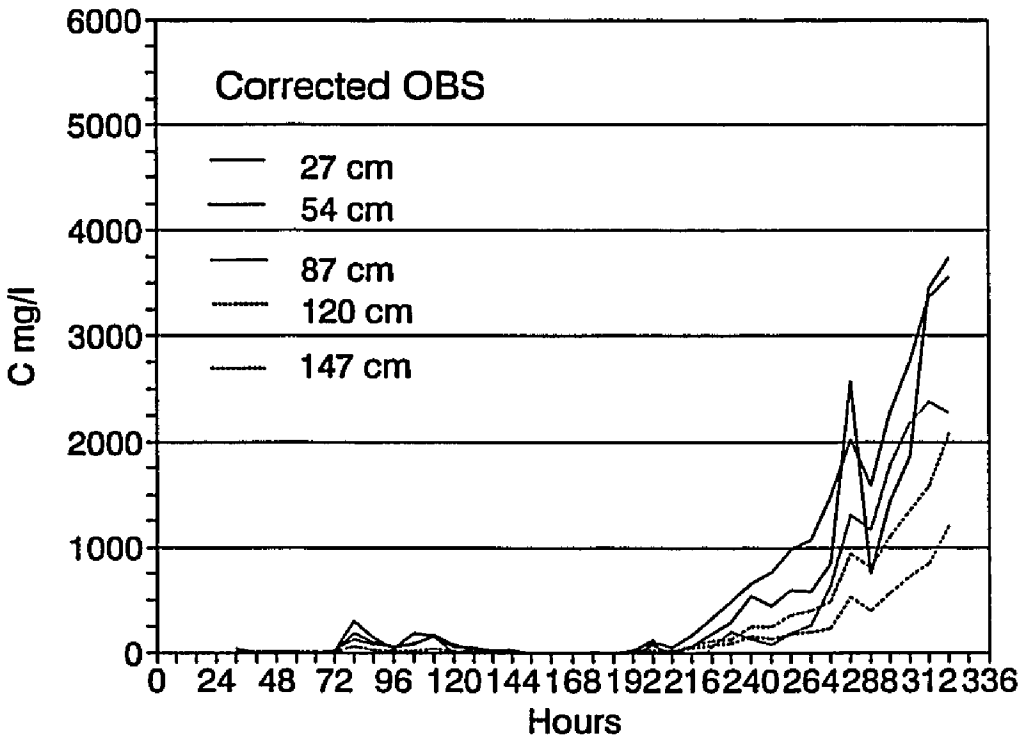
Corrected OBS
27 cm
54 cm
87 cm
120 cm
147 cm
C mg/l
6000
5000
4000
3000
2000
1000
0
0 24 48 72 96 120 144 168 192 216 240 264 288 312 336
Hours

Table 2.2 OBS measurements from the tripod

	C_1	C_2	C_3	C_4	C_5
Low energy	g/l	g/l	g/l	g/l	g/l
Hr80	0.306	0.184	0.133	0.063	0.056
Hr104	0.183	0.088	0.082	0.017	0.003
Moderate					
Hr248	0.439	0.767	0.077	0.247	0.131
Hr256	0.587	0.976	0.190	0.352	0.175
Hr264	0.581	1.072	0.261	0.403	0.197
Hr272	0.852	1.481	0.639	0.488	0.233
High					
Hr296	1.442	2.282	1.783	1.102	0.572
Hr304	1.856	2.754	2.177	1.349	0.719
Hr312	3.450	3.359	2.379	1.578	0.851
Hr320	3.737	3.556	2.270	2.083	1.197

C_1, C_2, C_3, C_4, and C_5 are measured at 27, 54, 87, 120, and 147 cm above the bottom, respectively.

3. A WAVE-CURRENT-SEDIMENT INTERACTION BOUNDARY LAYER MODEL

3.1 Introduction

A boundary layer model which addresses the non-linear interactions among wave, current and bottom non-cohesive sediments is discussed in this chapter. Theoretically, it is a combination of existing boundary layer model (Madsen and Wikramanayake, 1991) and a sediment suspension model. It is used to predict the flow and suspended sediment field by providing some simple known characteristics of wave, current and sediment.

On continental shelves, when waves propagate from deep water to shallow water, they eventually will experience the presence of the bottom at some depth that depends on the period and amplitude of the waves. Unlike the conditions in laboratories, both waves and currents are present in field. Tide and wind, among others, are the main causes of currents. The model presented here basically accounts for the non-linear interactions among wave, current and bottom sediments. Figure 3.1 conceptually sketches the interactions.

The wave-current-sediment interactions can be partitioned into two parts: wave-current interaction (combined boundary layer) and flow-sediment interaction (sediment suspension and stratification). The wave-current interaction, which typically determine the structure of the near-bottom flow (Glenn and Grant, 1987) is associated with the non-linear coupling of short time scale of wave and relatively long time scale of current boundary layers. This interaction

Figure 3.1 Concept sketch of wave-current-sediment interaction in a combined boundary layer

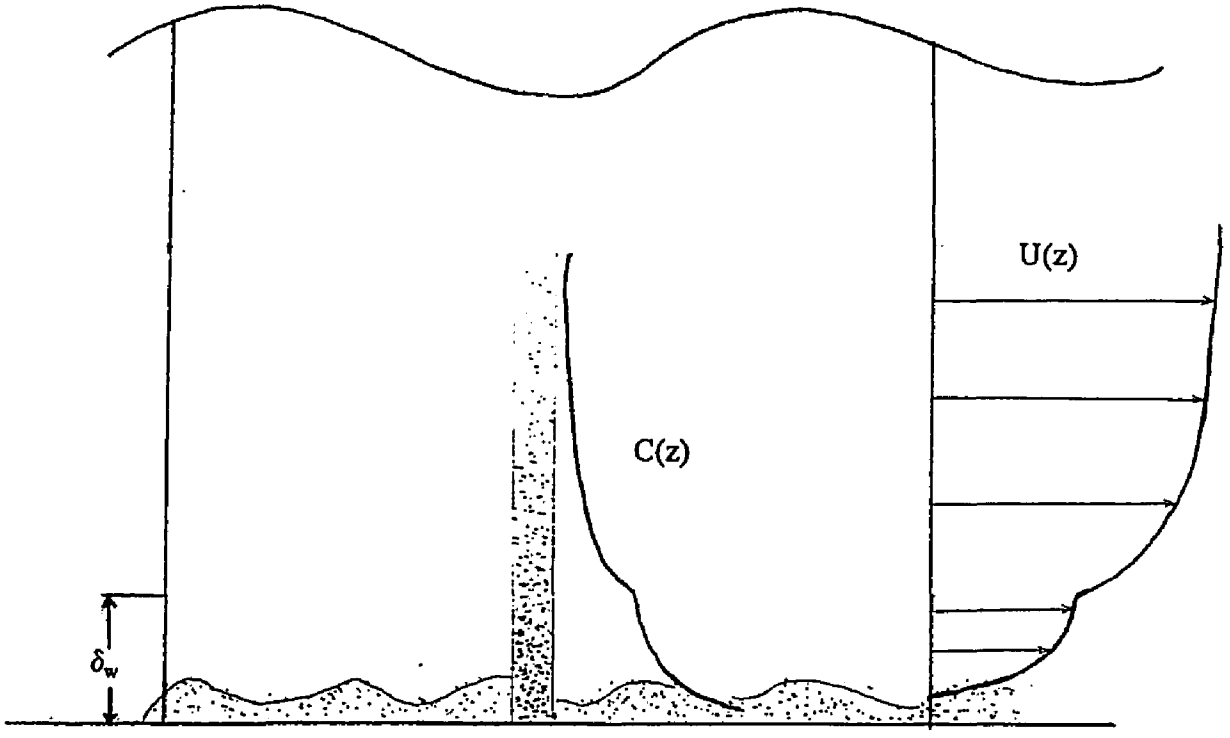
U(z)
C(z)
δ_w

results in an wave boundary layer nested within a relatively steady current boundary layer. Owing to the high frequency of flow reversal, the wave boundary layers have very little time to develop and they are very thin in comparison to the steady current boundary layer. When the maximum near-bottom wave velocities are the same order as the near bottom current velocities, which is typically the case on continental shelves, the small scale of the wave boundary layer causes the boundary shear stress that would be associated with the wave to be much greater than that associated with the current (Glenn and Grant, 1987).

The boundary shear stress in a fully rough turbulent flow also depends on the physical bottom roughness; a larger bottom roughness results in a larger shear stress (Glenn and Grant, 1987). In a wave-current boundary layer, if the boundary shear stress is smaller than the critical shear stress which is required to lift the sediments from bottom, the bottom roughness will be only associated to the bottom sediments and, if any, preexisting bed forms. If the boundary shear stress is greater than the critical shear stress, bottom sediment will be in motion and more stable bottom configuration, ripples, are generated. Ripples and sediment movements will increase the bottom roughness which causes the boundary shear stress to increase. Above the wave boundary layer, the current-generated turbulence is responsible to distribute the suspended sediments over the water column. Therefore, it is the wave-generated high boundary shear stress that initiate the motion of the bottom sediments within the wave boundary layer. It is the non-oscillating current which can possibly transport the suspended sediment.

A considerable amount of work have been done towards these two interactions. Smith (1977), Grant and Madsen (1979, 1986), Tanaka and Shuto (1981), Christofferson and

Jonsson (1985) all proposed combined wave-current boundary layer models. One feature shared by all these models was that the shear velocity was used to scale the turbulent eddy viscosity. The difference between one and another was that different linear relation was used. For example, Smith (1977) used a two layer linear model and scaled the eddy viscosity by the sum of wave and current shear velocities inside the wave boundary layer and by current shear velocity alone outside of the wave boundary layer. Grant and Madsen (1979, 1986) scaled the eddy viscosity inside the wave boundary layer by the total shear velocity and outside the wave boundary layer, identical to Smith's (1977) model, by the current shear velocity. The eddy viscosity was discontinuous at the top of the wave boundary layer in Grant and Madsen (1986) but continuous in Smith (1977). Tanaka and Shuto (1981) used a one layer linear eddy viscosity model.

A sophisticated numerical approach to model the eddy viscosity was proposed by Davis, Soulsby and King (1988). A significant difference between this numerical approach and the eddy viscosity models was that the numerical model allowed the eddy viscosity to be time-varying in contrast to the time-invariant eddy viscosity models. It applied a two-equation model to compute the two components of the eddy viscosity, the velocity scale which was taken as the square root of the average turbulent kinetic energy, and the length scale. Because of its greater sophistication than the simple eddy viscosity model, the velocity field and other parameters obtained from this numerical approach are expected to be more accurate (Madsen and Wikramanayake, 1991). Madsen and Wikramanayake (1991) modified the Grant and Madsen (1979, 1986) model and proposed a three-layer viscosity combined boundary layer model in which the discontinuity of the eddy viscosity at the edge of the wave boundary layer was removed. Madsen and Wikramanayake (1991) also proposed a time-varying eddy

viscosity model with an assumption of weak current. Although the time-varying model improved the solution in terms of sensitivity to the angle between the wave propagation and current, it is only slightly different from the solution of the time-invariant eddy viscosity model. Thus the three-layer time-invariant eddy viscosity model will be adopted, for simplicity, as the wave-current interaction model in this study.

The flow-sediment interaction is closely related to the wave-current interaction. In coastal water, the waves dissipate and, combined with currents, exert shear stresses on the bottom sediments (only non-cohesive sediments are considered in this study). Exceeding a critical condition when the shear stress is large enough, the sediment will be lifted from the bottom and diffused upward into the water column. Meanwhile, bottom features such as ripples and other bed-forms are generated and the bed roughness is changed by the addition of form drag elements. The flow, affected by the change of bottom roughness and sediment in the water (which changes the density and generate stratification), has to adjust itself. These adjustments among the flow and sediments will eventually bring about an equilibrium. The interaction of flow and bottom sediments has been heavily studied both in the laboratory and the field. Since waves play a much more important role in the flow-sediment interaction, most studies were done only under wave conditions. Carstens, et al (1969), Lofquist (1978), Nielsen (1979), Miller and Komar (1980a, 1980b), Rosengaus (1987), Sato (1988) and Mathisen (1989) made laboratory experiments with regular waves and made the bed form geometry measurements. Rosengaus (1987), Sato (1988) and Mathisen (1989) also conducted laboratory experiments with irregular waves. Inman (1957), Dingler (1974), Nielsen (1984), among others, studied the flow-sediment interactions in the field measurements. Wikramanayake and Madsen (1991) analyzed all the data above and developed relations

between bottom bed-form geometry and flow conditions. Wiberg and Smith (1983) developed a model for the combined boundary layer by taking account of the stratification. Glenn and Grant (1987) modified the Grant and Madsen (1979) combined boundary layer model by involving the sediment concentration and sediment-induced stratification into the model.

In this chapter, the three-layer combined boundary layer model by Madsen and Wikramanayake (1991) will firstly be adopted and then, similar to the approach by Glenn and Grant (1987), modified by introducing the sediment concentration and sediment induced stratification into the model, and finally, expressions of velocity and concentration profiles will be developed.

3.2 Governing equations

The mixture of fluid and suspended sediment is treated as a continuum here. In order to do this, two approximations are introduced. First, the concentration of suspended sediment is assumed low enough to permit inter-particle interactions to be neglected. Lumley (1978) suggests that so long as the volumetric sediment concentration is not larger than 3×10^{-3} (i.e. mass concentration of 8 g/l for quartz sediments), inter-particle interactions can be neglected. Suspended sediment volumetric concentrations are expected to be of the order of 10^{-3} or less outside of the surf zone on the continental shelf (Glenn and Grant, 1987). The second approximation is that sediment velocity is assumed equal to the fluid velocity minus the particle settling velocity. This approximation is assumed to be adequate for the large-scale, energetic eddies that scale with distance from the bottom (Glenn and Grant, 1987).

Using scaling arguments applied by Madsen and Wikramanayake (1991), and

neglecting Coriolis force, the linearized Reynolds-averaged governing equations for a combined wave-current flow with small concentrations of suspended sediment are given by

$$\frac{\partial <\vec{u}>}{\partial t} = -\frac{1}{\rho}\frac{\partial <p>}{\partial x} - \frac{\partial}{\partial z}<\vec{u}'w'> \tag{3.1}$$

$$\frac{\partial <C>}{\partial t} - w_f\frac{\partial <C>}{\partial z} + \frac{\partial}{\partial z}<C'w'> = 0 \tag{3.2}$$

where $\vec{u}$ is the horizontal fluid velocity, w is the vertical fluid velocity, p is the pressure, ρ is the fluid density, C is the sediment concentration, w_f is the sediment settling velocity, t is time , and z is the vertical coordinate measured positive upward from the bottom. The prime and angle bracket denote the turbulent fluctuation and Reynolds-average, respectively.

To solve (3.1) and (3.2), an eddy viscosity and eddy diffusivity closure scheme similar to that applied by Glenn and Grant (1987) is adopted

$$-<\vec{u}'w'> = \nu_{tm}\frac{\partial <\vec{u}>}{\partial z} \tag{3.3}$$

$$-<C'w'> = \nu_{ts}\frac{\partial <C>}{\partial z} \tag{3.4}$$

where ν_{tm} is the turbulent eddy viscosity and ν_{ts} is the turbulent eddy diffusivity of sediment mass. ν_{tm} and ν_{ts} are then assumed analogous with formulae used in atmospheric boundary layers affected by stable thermal stratification:

$$\nu_{cm} = \frac{\nu_t}{1 + \beta\left(\frac{z}{L}\right)} \tag{3.5}$$

$$\nu_m = \frac{\nu_t}{\gamma + \beta\left(\frac{z}{L}\right)} \tag{3.6}$$

where υ_t is the eddy viscosity under neutral flow condition, γ and β are empirical constants. The effect of stable stratification is represented by z/L and

$$L = \frac{\rho u_*^3}{\kappa g \langle \rho' w' \rangle} \tag{3.7}$$

is the Monin-Obukhov length. In equation (3.7), u_* is the shear velocity, g is the acceleration due to gravity and κ (=0.41) is von Karman's constant.

At this point, the eddy viscosity under neutral flow, υ_t, is left to be modeled in order to solve the governing equations. Eddy viscosity models have been developed for oscillatory flow by Kajiura (1968), Myrhaug (1982) and Brevik (1981) and for combined steady and oscillatory flow by Smith (1977), Grant and Madsen (1979, 1986), Christofferson and Jonsson (1985), Tanaka and Shuto (1981) and Madsen and Wikramanayake (1991). The viscosity model by Madsen and Wikramanayake (1991) will be used here.

3.3 Eddy viscosity model

The Madsen and Wikramanayake (1991) time-invariant eddy viscosity model is a refinement of Grant and Madsen (1986) model. In this model, eddy viscosity υ_t is scaled by shear velocity (velocity scale) and height above the bottom (length scale) (Figure 3.2):

Figure 3.2 Sketch showing the 3 layer eddy viscosity model by Madsen and Wikramanayake (1991)

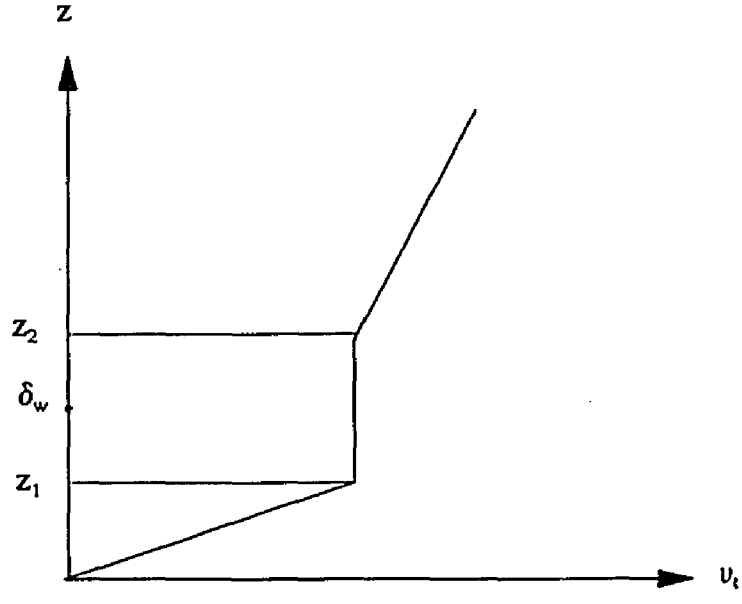
z
z_2
δ_w
z_1
v_t

$$\nu_t = \begin{cases} \kappa u_{*cw} z & z_0 < z < z_1 \\ \kappa u_{*cw} \alpha \delta_w & z_1 < z < z_2 \\ \kappa u_{*c} z & z > z_2 \end{cases} \tag{3.8}$$

where $z_1 = \alpha\delta_w$, $z_2 = z_1/\varepsilon$. α is a free parameter used to define a fraction of the wave boundary layer thickness. α is assumed equal to 0.5 following Madsen and Wikramanayake (1991). In equation (3.8), u_{*cw} is the shear velocity based on the maximum combined bottom shear stress, u_{*c} is the shear velocity based on time-averaged (current) bottom shear stress.

$$u_{*c} = \sqrt{\frac{\tau_c}{\rho}}$$
$$u_{*cw} = \sqrt{\frac{\tau_m}{\rho}} \tag{3.9}$$

where τ_c is current shear stress and τ_m is the maximum combined shear stress. The wave boundary layer thickness, δ_w, is defined as

$$\delta_w = \frac{\kappa u_{*cw}}{\omega} \tag{3.10}$$

in which ω is radian wave frequency. ϵ is a parameter denoting the relative magnitude of the current and wave shear velocities

$$\varepsilon = \frac{u_{*c}}{u_{*cw}} \tag{3.11}$$

Since u_{*c} is always smaller than u_{*cw} in the problem, ε is always smaller than unity.

As indicated in equation (3.8), the shear velocities differ depending on whether we are within or above the wave boundary layer. Above the wave boundary layer, the shear velocity, u_{*c}, is only related to the mean flow, and within the wave boundary layer, the shear velocity, u_{*cw}, results from the wave-current interaction and hence u_{*cw} is larger than u_{*c}. In this three-layer model, the viscosity is a linear function of z at both top and bottom layers and constant at the middle layer.

Following the approach of Glenn and Grant (1987), fluid velocity, pressure and suspended sediment concentration in a turbulent wave-current combined flow can be partitioned into the following three components:

$$\vec{u} = \vec{u}_c + \vec{u}_w + \vec{u}'$$

$$p = p_c + p_w + p' \qquad (3.12)$$

$$C = C_m + C_p + C'$$

where the subscript c represents the current component, w represents the wave component. Subscripts m and p in the concentration partitioning denote mean and periodic respectively. Prime is for turbulent fluctuation. The mean concentrations are assumed to be quasi-steady and periodic concentrations are assumed to have a period of half of the wave period.

Follow Glenn and Grant (1987), it is further assumed that waves and turbulence are not correlated within the wave boundary layer and equation (3.12) simplifies by Reynolds-averaging to:

$$<\vec{u}> = \vec{u}_c + \vec{u}_w$$

$$<p> = p_c + p_w \qquad z<\delta_w \qquad (3.13)$$

$$<C> = C_m + C_p$$

Substituting equation (3.13) into equations (3.3) and (3.4) gives

$$-<\vec{u}'w'> = \nu_{tm}\frac{\partial}{\partial z}(\vec{u}_c + \vec{u}_w) \qquad (3.14)$$

$$-<C'w'> = \nu_{ts}\frac{\partial}{\partial z}(C_m + C_p) \qquad (3.15)$$

Equations (3.14) and (3.15) indicate that both waves and currents are related to the turbulent diffusions within wave boundary layer. Substituting Equations (3.13), (3.14) and (3.15) into (3.1) and (3.2), and applying the assumption that $\vec{u}_c$ and C_m are quasi-steady, the governing equations within the wave boundary layer are derived.

$$\frac{\partial \vec{u}_w}{\partial t} = -\frac{1}{\rho}\frac{\partial}{\partial x}(p_c + p_w) + \frac{\partial}{\partial z}\left(\nu_{tm}\frac{\partial}{\partial z}(\vec{u}_c + \vec{u}_w)\right) \qquad z<\delta_w \qquad (3.16)$$

$$\frac{\partial C_p}{\partial t} - w_f\frac{\partial}{\partial z}(C_m + C_p) - \frac{\partial}{\partial z}\left(\nu_{ts}\frac{\partial}{\partial z}(C_m + C_p)\right) = 0 \qquad z<\delta_w \qquad (3.17)$$

Above the wave boundary layer, the time scale of the energetic turbulent fluctuations are the same order of magnitude as or greater than the wave period but are much less than the time scale of the quasi-steady current (Glenn and Grant, 1987), so the averaging time above the wave boundary layer is equal to or greater than the wave period. The Reynolds-averaged terms in equation (3.12) become

$$\langle \vec{u} \rangle = \vec{u}_c$$

$$\langle p \rangle = p_c \qquad z > \delta_w \tag{3.18}$$

$$\langle C \rangle = C_m$$

and the turbulent diffusion terms in this layer are

$$-\langle \vec{u}' w' \rangle = \nu_{tm} \frac{\partial \vec{u}_c}{\partial z} \qquad z > \delta_w \tag{3.19}$$

$$-\langle C' w' \rangle = \nu_{ts} \frac{\partial C_m}{\partial z} \qquad z > \delta_w \tag{3.20}$$

The flow and concentration field above the wave boundary layer ($z > \delta_w$) are governed by

$$0 = -\frac{1}{\rho}\frac{\partial p_c}{\partial x} + \frac{\partial}{\partial z}\left(\nu_{tm}\frac{\partial \vec{u}_c}{\partial z}\right) \qquad z > \delta_w \tag{3.21}$$

$$-w_f \frac{\partial C_m}{\partial z} - \frac{\partial}{\partial z}\left(\nu_{ts}\frac{\partial C_m}{\partial z}\right) = 0 \qquad z > \delta_w \tag{3.22}$$

3.4 Solutions

The Monin-Obukhov length L can be rewritten by expressing $\langle \rho' w' \rangle$ in terms of fluctuations of suspended sediment concentration. In a sediment laden flow, the bulk density of the fluid-sediment mixture can be described as

$$\rho = \rho_s C + (1-C)\rho_w$$
$$= C(\rho_s - \rho_w) + \rho_w \qquad (3.23)$$
$$= \rho_w(C(s-1)+1)$$

where ρ_w is the density of the fluid (here water), C is the volumetric concentration of suspended sediment, ρ_s is the density of sediment, and s is the relative sediment density. The turbulent fluctuation of density ρ' is

$$\rho' = \rho_w C'(s-1) \qquad (3.24)$$

Then, Reynolds-averaged turbulent mass diffusivity $<\rho' w'>$ can be rewritten as

$$<w'\rho'> = <w'\rho_w C'(s-1)>$$
$$= <w'C'(s-1)\rho_w> \qquad (3.25)$$
$$= \rho_w(s-1)<w'C'>$$

Substituting Equation (3.25) into (3.7) gives

$$L = \frac{u_*^3}{\kappa g}\frac{\rho}{\rho_w}\frac{1}{(s-1)<w'C'>}$$
$$= \frac{u_*^3}{\kappa g}\frac{C(s-1)+1}{(s-1)<w'C'>} \qquad (3.26)$$
$$= \frac{u_*^3}{\kappa g<w'C'>}\left(\frac{1}{s-1}+C\right)$$

Because C is in the order of 10^{-3} and much less than that of 1/(s-1), it can be neglected. Then

equation (3.26) becomes

$$L = \frac{u_*^3}{\kappa g(s-1)\langle w'C'\rangle} \tag{3.27}$$

and the stability parameter can be written as

$$\frac{z}{L} = \frac{\kappa z}{u_*^3} g(s-1)\langle w'C'\rangle \tag{3.28}$$

Substituting equation (3.9) and (3.20) into (3.28), we derive the stability parameter above the wave boundary layer:

$$\frac{z}{L_c} = \frac{\kappa z}{u_{*c}^3} g(s-1)\left(-\nu_{ts}\frac{\partial C_m}{\partial z}\right) \qquad z>\delta_w \tag{3.29}$$

Substituting equation (3.9) and (3.15) into (3.28), we derive the stability parameter within the wave boundary layer:

$$\frac{z}{L_{cw}} = \frac{\kappa z}{u_{*cw}^3} g(s-1)\left(-\nu_{ts}\frac{\partial}{\partial z}(C_m + C_p)\right) \qquad z<\delta_w \tag{3.30}$$

Based on Grant and Madsen's (1979) argument that the turbulent momentum flux associated with the vertical gradient of the wave velocity must go to zero as the top of the wave boundary layer is approached, Glenn and Grant (1987) assumed that the turbulent concentration flux associated with the periodic concentration gradient also must go to zero. From equation (3.30) we know that the stability parameter is proportional to elevation z.

When z is close to z_0, no matter what the periodic concentration gradient is, the stability parameter is expected to be negligible anyway. Near the top of the wave boundary layer, the periodic concentration gradient is also unimportant because the gradient is close to zero. Therefore, it would be appropriate to simplify the stability parameter within the wave boundary layer by neglecting the periodic concentration gradient, i.e., equation (3.30) can be simplified as

$$\frac{z}{L_{cw}} = \frac{\kappa z}{u_{*cw}^3} g(s-1)\left(-\nu_{ts}\frac{\partial}{\partial z}C_m\right) \qquad z<\delta_w \tag{3.31}$$

3.4.1 About the continuity of the stability parameter

It is noticed from equations (3.29) and (3.31) that the stability parameter profile has a discontinuity at elevation $z=\delta_w$ because of the discontinuity of shear velocity at this elevation (equation 3.9). As we will show in the solutions in the next section, the stability parameter is a factor in both velocity and concentration profiles. This discontinuity may cause some difficulties in the calculations of the velocity and concentration profiles. As stated before, one assumption of this boundary layer model is the wave dominance and weak current. Under this assumption, it is common that the combined shear velocity, with high wave conditions, is often 4 to 5 times larger than the current shear velocity. A factor of 4 or 5 between u_{*c} and u_{*cw} will generate a large jump of the stability parameter at the top of the wave boundary layer, $z = \delta_w$, and also cause a rather dramatic change of velocity and concentration at this elevation. This kind of abrupt change should be avoided in dealing with the wave-current combined boundary layer. Attempt is made here to circumvent the stability parameter discontinuity problem. However, it is necessary to bear in mind that the continuous shear

velocity here is only for the sake of stability parameter calculation. It does not affect the shear velocity configuration in the eddy viscosity model.

Similar to the way in which Madsen and Wikramanayake (1991) modified the Grant and Madsen (1986) viscosity model, the shear velocity is modified to become continuous. Assume the shear velocity decreases linearly from u_{*cw} (at $z=z_1$) to u_{*c} (at $z=z_2$), the shear velocity between z_1 and z_2 is a linear function of z (Figure 3.3)

$$u_* = u_{*cw}\left(e + 1 - \frac{z}{z_2}\right) \qquad z_1<z<z_2 \tag{3.32}$$

The stability parameter in this region is

$$\frac{z}{L_m} = \frac{\kappa z}{u_*^3} g(s-1)\left(-\nu_{ts}\frac{\partial}{\partial z} C_m\right) \qquad z_1<z<z_2 \tag{3.33}$$

Now, equation (3.29) is used in the region $z>z_2$ and equation (3.31) in $z<z_1$. Equations (3.29), (3.31) and (3.33) give a continuous stability parameter profile.

3.4.2 Solutions of current and mean concentration

Averaging the governing Equations (3.16), (3.17), (3.21) and (3.22) over a wave period and neglecting the pressure gradient term near the bottom, the equations governing the current and mean concentration become

Figure 3.3 Sketch of the continuous shear velocity

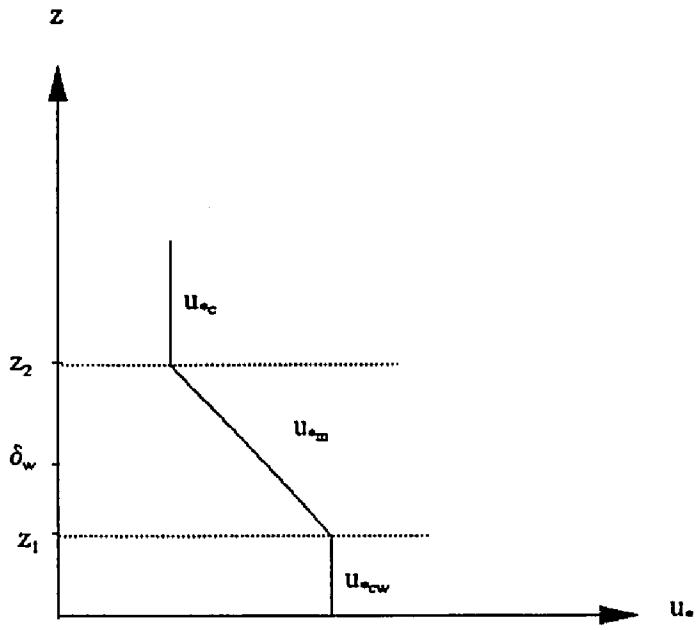
z
u_{e_c}
z_2
u_{e_m}
δ_w
z_1
$u_{e_{cw}}$
u_e

$$\frac{\partial}{\partial z}\left(\nu_{tm}\frac{\partial \vec{u}_c}{\partial z}\right)=0 \tag{3.34}$$

$$\frac{\partial}{\partial z}\left(w_f C_m+\nu_{ts}\frac{\partial C_m}{\partial z}\right)=0 \tag{3.35}$$

Equation (3.34) can be rewritten as

$$\nu_{tm}\frac{\partial \vec{u}_c}{\partial z}=u_{*c}^{\,2} \tag{3.36}$$

and since the mean concentration C_m is not a function of time, equation (3.35) can be rewritten as

$$w_f C_m+\nu_{ts}\frac{\partial C_m}{\partial z}=0 \tag{3.37}$$

i.e., the vertical net flux is zero. Equations (3.36) and (3.37) are the governing equations for current and mean concentration near the bottom.

Substituting ν_{tm} and ν_{ts} in equations (3.36) and (3.37) by the corresponding eddy viscosity and eddy diffusivity described in equations (3.5), (3.6) and (3.8), we can obtain:

$$\frac{\kappa u_{*cw} z}{1+\beta\left(\frac{z}{L_{cw}}\right)}\frac{\partial \bar{u}_c}{\partial z} = u_{*c}^{\,2} \qquad z<z_1 \tag{3.38}$$

$$w_f C_m + \frac{\kappa u_{*cw} z}{\gamma+\beta\left(\frac{z}{L_{cw}}\right)}\frac{\partial C_m}{\partial z} = 0 \qquad z<z_1 \tag{3.39}$$

We then apply the non-slip condition at $z=z_0=k_b/30$ and get the solution of the mean current:

$$\begin{aligned} u_c &= \frac{u_{*c}u_{*c}}{u_{*cw}\kappa}\left(\ln\left(\frac{z}{z_0}\right)+\beta\int_{z_0}^{z}\frac{dz}{L_{cw}}\right) \\ &= e\frac{u_{*c}}{\kappa}\left(\ln\left(\frac{z}{z_0}\right)+\beta\int_{z_0}^{z}\frac{dz}{L_{cw}}\right) \qquad z<z_1 \end{aligned} \tag{3.40}$$

where z_0 is the hydraulic roughness length.

Introducing the reference concentration, $C_m(z_0)$ which is assumed, for the moment, be a known, equation (3.39) can be integrated to give the solution of the mean concentration within the bottom layer.

$$C_m(z) = C_m(z_0)\left(\frac{z}{z_0}\right)^{-B\gamma}\exp\left(-B\beta\int_{z_0}^{z}\frac{dz}{L_{cw}}\right) \qquad z<z_1 \tag{3.41}$$

where B is the Rouse number and

$$B = \frac{w_f}{\kappa u_{*cw}} \tag{3.42}$$

For the middle layer, $z_1 < z < z_2$, the governing equations become

$$\frac{\kappa u_{*cw} z_1}{1+\beta\left(\frac{z}{L_m}\right)} \frac{d\bar{u}_c}{dz} = u_{*c}^2 \qquad z_1<z<z_2 \tag{3.43}$$

$$w_f C_m + \frac{\kappa u_{*cw} z_1}{\gamma+\beta\left(\frac{z}{L_m}\right)} \frac{dC_m}{dz} = 0 \qquad z_1<z<z_2 \tag{3.44}$$

Equations (3.43) and (3.44) can be rearranged to

$$\frac{du_c}{dz} = \frac{u_{*c} u_{*c}}{u_{*cw}\kappa}\left(\frac{1}{z_1} + \frac{\beta}{z_1}\frac{z}{L_m}\right) \qquad z_1<z<z_2 \tag{3.45}$$

$$\frac{dC_m}{dz} + \frac{w_f}{\kappa u_{*cw}}\left(\frac{\gamma}{z_1} + \frac{\beta}{z_1}\frac{z}{L_m}\right) C_m = 0 \qquad z_1<z<z_2 \tag{3.46}$$

Using the condition of matching current velocity at $z = z_1$ to determine the integration constant, the solution of the current at the middle layer is attained:

$$u_c = e\frac{u_{*c}}{\kappa}\left(\frac{z}{z_1} - 1 + \ln\left(\frac{z_1}{z_0}\right) + \beta\int_{z_0}^{z_1}\frac{dz}{L_{cw}} + \frac{\beta}{z_1}\int_{z_1}^{z}\frac{z}{L_m}dz\right) \qquad z_1<z<z_2 \tag{3.47}$$

Obtaining the mean concentration at z_1 from equation (3.41) and using this concentration as a boundary condition, the mean concentration profile in the middle layer is derived.

$$C_m(z) = C_m(z_1)\exp\left(-B\gamma\left(\frac{z}{z_1}-1\right)-\frac{B\beta}{z_1}\int_{z_1}^{z}\frac{z}{L_m}dz\right) \qquad z_1<z<z_2 \tag{3.48}$$

where

$$C_m(z_1) = C_m(z_0)\left(\frac{z_1}{z_0}\right)^{-B\gamma}\exp\left(-B\beta\int_{z_0}^{z_1}\frac{dz}{L_{cw}}\right) \tag{3.49}$$

For the top layer, $z > z_2$, the governing equations are

$$\frac{\kappa u_{*c} z}{1+\beta\left(\frac{z}{L_c}\right)}\frac{du_c}{dz} = u_{*c}^{\,2} \qquad z>z_2 \tag{3.50}$$

$$\frac{\kappa u_{*c} z}{\gamma+\beta\left(\frac{z}{L_c}\right)}\frac{dC_m}{dz} + w_f C_m = 0 \qquad z>z_2 \tag{3.51}$$

Equations (3.50) and (3.51) can be rewritten as

$$\frac{du_c}{dz} = \frac{u_{*c}}{\kappa}\left(\frac{1}{z}+\frac{\beta}{L_c}\right) \qquad z>z_2 \tag{3.52}$$

$$\frac{dC_m}{dz} + \frac{w_f}{\kappa u_{*c}}\left(\frac{\gamma}{z}+\frac{\beta}{L_c}\right)C_m = 0 \qquad z>z_2 \tag{3.53}$$

Integrating Equations (3.52) and (3.53) and determining the constants of integration by matching the current velocities and mean concentrations at z_2 gives the solution of u_c and C_m

in the top layer.

$$u_c = \frac{u_{*c}}{\kappa}\left\{1 - \varepsilon + \ln(\frac{z}{z_2}) + \varepsilon\left(\ln\left(\frac{z_1}{z_0}\right) + \beta\int_{z_0}^{z_1}\frac{dz}{L_{cw}} + \frac{\beta}{z_1}\int_{z_1}^{z_2}\frac{z}{L_m}dz\right) + \beta\int_{z_2}^{z}\frac{dz}{L_c}\right\} \qquad z>z_2 \tag{3.54}$$

$$C_m(z) = C_m(z_2)\left(\frac{z}{z_2}\right)^{-\frac{B\gamma}{\varepsilon}}\exp\left(-\frac{B\beta}{\varepsilon}\int_{z_2}^{z}\frac{dz}{L_c}\right) \qquad z>z_2 \tag{3.55}$$

where

$$C_m(z_2) = C_m(z_0)\left(\frac{z_1}{z_0}\right)^{-B\gamma}\exp\left\{-B\gamma\left(\frac{1}{\varepsilon}-1\right) - B\beta\left(\int_{z_0}^{z_1}\frac{dz}{L_{cw}} + \frac{1}{z_1}\int_{z_1}^{z_2}\frac{z}{L_m}dz\right)\right\} \tag{3.56}$$

Substituting equation (3.37) into (3.29) (3.33) and (3.31) give the expressions of the simplified continuous stability parameters

$$\frac{z}{L_c} = \frac{\kappa z}{u_{*c}^3}g(s-1)w_f C_m(z) \qquad z>z_2 \tag{3.57}$$

$$\frac{z}{L_m} = \frac{\kappa z}{u_*^3}g(s-1)w_f C_m(z) \qquad z_1<z<z_2 \tag{3.58}$$

$$\frac{z}{L_{cw}} = \frac{\kappa z}{u_{*cw}^3}g(s-1)w_f C_m(z) \qquad z<z_1 \tag{3.59}$$

The u_* in equation (3.58) is described in equation (3.32).

3.5 The reference concentration model

The reference concentration $C_m(z_0)$ must be determined in order to calculate the vertical concentration profiles. Modeling the reference concentration has been the subject that has been of concern to many investigators (e.g., Yalin, 1963; Owen, 1964; Smith, 1977; Smith and McLean, 1977a, 1977b; McLean, 1991). Various reference concentration models have been proposed (Kim, 1991). In most models, reference concentration $C_m(z_0)$ is a function of excess shear stress and/or bed concentration C_b,

$$C_m(z_0)=f(S_n, C_b) \tag{3.60}$$

where S_n is the normalized excess shear stress.

$$S_n=\left\langle \frac{|\tau'|}{\tau_c}-1 \right\rangle \tag{3.61}$$

In equation (3.61), τ_c is the critical shear stress for initiation of motion of the sediment obtained from the modified Shields diagram of Madsen and Grant (1976). τ' is the skin friction shear stress. $< >$ denotes time averaging. For combined wave-current flows dominated by the wave motion we have $|\tau'| \simeq \tau_{wm}'|\cos \omega t| = \rho u_{*wm}'^2|\cos \omega t|$, where u_{*wm}' is the maximum skin friction velocity, which is obtained by applying the hydrodynamic boundary layer model discussed in this chapter. τ_{wm}' is the maximum skin friction shear stress. The time average of the skin friction shear stress can be simplified as $< |\tau'| > = (2/\pi)\ \tau_{wm}'$.

Among other reference concentration models, the Smith and McLean (1977a, 1977b) model has been widely recognized. This model introduced an empirical suspension coefficient γ_0, and gave the following formula to calculate the reference concentration $C_m(z_0)$:

$$C_m(z_0) = \frac{\gamma_0 C_b S_n}{1 + \gamma_0 S_n} \tag{3.62}$$

where γ_0 is called resuspension coefficient. Normally, C_b is treated as a constant (=0.65) for sediments containing one single grain size. When multiple grain size exist, $C_m(z_0)$ and C_b are replaced by $C_{mi}(z_0)$ and C_{bi} which are the reference concentration and bed concentration of the *i*th grain size class respectively. S_a can be calculated using a boundary layer model, e.g., Smith and McLean, 1977; Grant and Madsen, 1986; Madsen and Wikramanayake, 1991, etc. In the case of multiple grain size, the critical shear stress for each individual grain size, τ_i is used. The resuspension coefficient, γ_0, is the essential parameter to be obtained and this will be the topic of Chapter 6. This reference concentration model will be used throughout this thesis. The resuspension coefficient is assumed equal 2 x 10^{-3} until more details are discussed in Chapter 6.

4. BOTTOM ROUGHNESS UNDER THE WAVE-CURRENT-SEDIMENT INTERACTION

4.1 Introduction

In a wave-dominated continental shelf environment, the wave motion interacts with the bottom sediment to generate bedforms and cause sediment transport when the wave-induced shear force exceeds the critical Shields parameter. Both the bedforms and sediment transport will increase the total bottom roughness which will then affect the rate of wave energy dissipation. The elements in this circle will mutually adjust until an equilibrium is established. Old equilibria will be broken and new ones established whenever bed shear stress changes.

Bottom roughness and reference concentration are critical in determining the current and mean concentration solutions discussed in section 3.4. This problem has been addressed by several investigations (Nielsen, 1977, 1981; Miller and Komar, 1980a, 1980b; Grant and Madsen 1982; Smith and McLean 1977a, 1977b). The convention is to partition the roughness into three parts, i.e

$$k_b = k_{bd} + k_{br} + k_{bm} \tag{4.1}$$

where k_b is the total bottom roughness, k_{bd} is the grain roughness and usually equal to the grain size multiplied by a constant (e.g. 2.5), k_{br} is ripple roughness (or other kind, such as biological roughness) and k_{bm} is the roughness caused by sediment motion. The last two terms are movable bed roughness. The significance of each term is relative and related to the

sediment properties and flow hydrodynamics. They depend on the maximum skin friction Shields parameter, ψ_m', and critical Shields parameter, ψ_c, for the sediment. Under low flow conditions when $\psi_m' < \psi_c$, no ripples are generated on the bottom and there is no sediment transport. Therefore only grain roughness is important when $\psi_m' < \psi_c$ except in situations where ripples are residual. If previous ripples and/or biogenic roughness exists, both will affect the bed roughness. Under moderate flow conditions, i.e., when the skin friction Shields parameter exceeds the critical Shields parameter for the sediment, pre-existing bedforms and biogenic roughness, if any, will be remolded. Since there is little sediment transport at this stage, ripple roughness makes the most important contribution. During storm condition (high waves), the bottom shear stress is high and ripples are washed out. During this high wave condition, sediment motion roughness dominates. In this chapter, field data are used to test the performance of several bottom toughness models. A new movable roughness model is also presented.

4.2 Existing roughness models

In order to model the bottom roughness, relations between sediment properties, flow dynamics and ripple geometry must first be obtained. Three important parameters representing the hydrodynamics and sediment properties are involved in these relations. These parameters are: maximum skin friction Shields parameter ψ_m', critical Shields parameter ψ_c, and fluid-sediment parameter S_* (Grant and Madsen, 1982). They are expressed as:

$$\psi'_m = \frac{\tau'_{wm}}{(s-1)\rho g d} \tag{4.2}$$

$$S_* = \frac{d}{4\nu}\sqrt{(s-1)gd} \tag{4.3}$$

If S_* is known, ψ_c can be found directly from the Shields graph (Madsen and Grant 1976). In equation (4.2), $\tau_{wm}' = 0.5\rho f_w' u_{bm}^2$ is the maximum skin friction shear stress, f_w' is the skin friction factor (the method of obtaining f_w' is discussed in section 4.3) and u_{bm} is the maximum orbital velocity. Other parameters involved such as s, ρ, g, and d have been previously defined. ν is the kinematic viscosity of water.

Using these parameters, investigators have derived different bottom roughness models. Based on the data from laboratory-generated bedforms in pure oscillatory flow with several grain sizes of sediments, Grant and Madsen (1982) defined two ranges of ripple development. Ripples attain their maximum steepness when $\psi_c < \psi_m' < \psi_b$ where ψ_b is the break-off Shields parameter,

$$\psi_b = 1.8 S_*^{0.6} \psi_c \tag{4.4}$$

In this range, the following empirical ripple geometry relations were derived:

$$\frac{\eta}{A_b} = 0.22\left(\frac{\psi'_m}{\psi_c}\right)^{-0.16} \tag{4.5}$$

$$\frac{\eta}{\lambda} = 0.16\left(\frac{\psi'_m}{\psi_c}\right)^{-0.04} \tag{4.6}$$

where η is the ripple height, λ is the ripple length and $A_b = u_{bm}/\omega$ is the orbital excursion amplitude. When $\psi_m' > \psi_b$, (break off range), Grant and Madsen (1982) found a different set of ripple geometry relations

$$\frac{\eta}{A_b} = 0.48 S_*^{0.8}\left(\frac{\psi'_m}{\psi_c}\right)^{-1.5} \tag{4.7}$$

$$\frac{\eta}{\lambda} = 0.28 S_*^{0.6}\left(\frac{\psi'_m}{\psi_c}\right)^{-1.0} \tag{4.8}$$

Using the ripple geometry from the equations above, Grant and Madsen (1982) obtained an empirical ripple roughness relation from laboratory measurements of energy dissipation over rippled beds in the equilibrium range

$$k_{br} = 28\eta\left(\frac{\eta}{\lambda}\right) \tag{4.9}$$

Nielsen (1981) also derived a set of empirical relations of ripple geometry and ripple roughness from analyzing the field data by Inman (1957), Dingler (1974) and Miller and Komar (1980):

$$\frac{\eta}{A_b} = 21\theta^{-1.85} \tag{4.10}$$

$$\frac{\eta}{\lambda} = 0.342 - 0.34\,\psi_m'^{\,0.25} \tag{4.11}$$

In equation (4.10), θ was defined as

$$\theta = \frac{u_{bm}^{\,2}}{(s-1)gd} \tag{4.12}$$

Using Carstens, et al's (1969) and Lofquiest's (1986) laboratory measurements of wave energy dissipation, Nielsen (1983, 1992) obtained a relation similar to equation (4.9) but with a different constant

$$k_{br} = 8\eta\left(\frac{\eta}{\lambda}\right) \tag{4.13}$$

Reanalyzing the field data used by Nielsen (1981), Wikramanayake and Madsen (1991) introduced another set of empirical evaluations of ripple geometry and ripple roughness:

$$\frac{\eta}{\lambda} = 0.34 - 0.40Z^{0.16} \tag{4.14}$$

$$\begin{aligned} \frac{\eta}{A_b} &= 0.011Z^{-0.60} && Z<0.015 \\ \frac{\eta}{A_b} &= 0.0002Z^{-1.54} && Z>0.015 \end{aligned} \tag{4.15}$$

where

$$Z = \frac{\psi'_m}{S_*} \tag{4.16}$$

is a dimensionless parameter. By best-fitting their evaluated data for energy dissipation measured in laboratory experiments, Wikramanayake and Madsen (1991) concluded a very simple relation between the ripple roughness and ripple geometry:

$$k_{br} = 4\eta \tag{4.17}$$

According to Wikramanayake and Madsen (1991), the equivalent ripple geometry equations (4.14) and (4.15) are not always valid. Their validity range of Z is between 1.5 x 10^{-3} and 1.5 x 10^{-1}. In terms of grain size, d, the equations are valid in the range from d = 0.08 mm to d = 0.64 mm, which covers most bottom sediment on continental shelves.

In addition to the ripple roughness, sediment motion roughness had also been modeled by many investigators. Grant and Madsen (1982), Nielsen (1981) and Wikramanayake and Madsen (1991) developed different sediment motion roughness models. Grant and Madsen (1982) defined a sediment transport layer and related the sediment motion roughness k_{bm} to the thickness of the sediment transport layer, h_{tm}, by

$$k_{bm} = 3.8 h_{tm} \tag{4.18}$$

where

$$h_{tm} = 42(s+0.5)d(\sqrt{\psi'_m} - 0.7\sqrt{\psi_c})^2 \tag{4.19}$$

If s = 2.65, equation (4.19) becomes

$$k_{bm} = 430d(\sqrt{\psi'_m} - 0.7\sqrt{\psi_c})^2 \tag{4.20}$$

Both Nielsen (1981) and Wikramanayake and Madsen (1991) have derived very similar relations:

Nielsen (1981)

$$k_{bm} = 190d(\psi'_m - \psi_c)^{0.5} \tag{4.21}$$

Wikramanayake and Madsen (1991)

$$k_{bm} = 340d(\sqrt{\psi'_m} - 0.7\sqrt{\psi_c})^2 \tag{4.22}$$

Combining the expressions of grain roughness, ripple roughness and sediment motion roughness, the three existing roughness models described above can be expressed as:

Grant and Madsen (1982)

$$k_b = d + 28\eta\left(\frac{\eta}{\lambda}\right) + 430d(\sqrt{\psi'_m} - 0.7\sqrt{\psi_c})^2 \tag{4.23}$$

Nielsen (1981)

$$k_b = 2.5d + 8\eta\left(\frac{\eta}{\lambda}\right) + 190d(\psi'_m - \psi_c)^{0.5} \tag{4.24}$$

Wikramanayake and Madsen (1991)

$$k_b = d + 4\eta + 340d(\sqrt{\psi'_m} - 0.7\sqrt{\psi_c})^2 \tag{4.25}$$

In a recent study by Madsen et al (1993, in press), the physical bed roughness in sheet-flow conditions (flat bed) was found to be approximately equal to 15 times the modal grain diameter, i.e.

$$k_{bm} = 15d \tag{4.26}$$

Along with other three roughness models, equation (4.23, 4.24 and 4.25), the Madsen et al's (1993, in press) model, which applied only under sheet-flow conditions, will be tested in the next section.

4.3 Test of roughness models using field data

The wave-current combined boundary layer model (Madsen and Wikramanayake, 1991) discussed in Chapter 3 was used to calculate the profiles of current and sediment concentration using the 4 roughness models from section 4.2. This boundary layer model (Madsen and Wikramanayake, 1991) is similar to Grant and Madsen (1986) model, the major difference being that it uses a three-layer continuous eddy viscosity model instead of a two-layer non-continuous eddy viscosity. The calculated velocity and concentration profiles are smooth as opposed to those from Grant and Madsen (1986) that exhibit kinks. The procedure starts by using the following approximate friction factor relationship (equation (24) of the Grant and Madsen, 1986),

$$\frac{1}{4\sqrt{f_w}} + \log_{10}\frac{1}{4\sqrt{f_w}} = \log_{10}\frac{A_b}{k_b} - 0.17 + 0.24(4\sqrt{f_w}) \tag{4.27}$$

to determine the skin friction factor f_w'. k_b is equal to the mean grain size for the Grant and

Madsen (1982) and Wikramanayake and Madsen (1991) models, and 2.5 times mean grain size for the Nielsen (1981) model in calculation of the skin friction factor. The skin friction factor is then used to calculate the maximum skin friction shear stress, $\tau_{wm}' = 0.5\rho f_w' u_{bm}^2$ and physical bottom roughness k_b using the 4 roughness models. The reference concentration $C_m(z_0)$ can be derived by assuming the bed sediment volume concentration $C_b = 0.65$ and the suspension coefficient $\gamma_0 = 2 \times 10^{-3}$ and using the Smith and McLean (1977) reference concentration model (γ_0 is roughness-dependent. Studies (Drake and Cacchione, 1989; Vincent et al, 1991) showed γ_0 also depended on excess shear stress. However, it will be discussed in detail in Chapter 6 why γ_0 should be a constant). Iterating k_b into equation (4.27) can bring out the solution of the total friction factor f_w which is then used to calculate the maximum wave shear velocity, the combined shear velocity and the current shear velocity. Using the solutions in Chapter3, the current and concentration profiles can be calculated. The stratification and multiple grain size effect are not considered here. The settling velocity of the mean grain size (d=0.0117 cm, w_f=1.01 cm/s) is used.

The boundary layer model was run against the field data of low (fair weather), moderate and high (storms) energy conditions listed in Table 2.1. The output of two example bursts from each of four roughness models are shown in Table 4.1. It is seen that substantial differences exist among the results from the four roughness models. For low energy conditions, the Grant and Madsen (1982) roughness model gives the highest ripple roughness and total roughness. The large difference of bottom roughness results in different modeled shear velocities. For moderate and high energy conditions, the ripple roughness diminishes with increasing bed shear stress, but the roughness caused by sediment motion increases.

Table 4.1 Output parameters from the model

		η	λ	ψ_m'	k_w	k_{bm}	f_w	u_{*cw}	u_*	δ_w	z_0
Hr. 80		cm	cm	-	cm	cm	-	cm/s	cm/s	cm	cm
	GM	4.69	38.08	0.15	16.19	0.25	0.14	7.42	1.92	7.08	0.55
	WM	0.12	2.74	0.15	0.48	0.17	0.03	3.31	1.20	3.16	0.02
	N	0.72	6.11	0.19	0.67	0.79	0.04	3.94	1.32	3.76	0.05
Hr. 312											
	GM	0.80	62.08	1.43	0.29	6.05	0.04	14.04	4.98	18.19	0.21
	WM	0	0	1.43	0	4.09	0.03	12.78	4.63	16.54	0.14
	N	0	0	1.76	0	2.89	0.03	11.91	4.39	15.42	0.10
	M	0	0	1.43	0	0.18	0.01	7.42	3.09	9.61	0.01

GM = Grant and Madsen (1982)
WM = Wikramanayake and Madsen (1991)
N = Nielsen (1981)
M = Madsen et al, (1993, in press)

Figures 4.1 to 4.3 show the estimated concentration profiles with different roughness models for low, moderate and high energy conditions respectively. Under low energy conditions (Figure 4.1), when the ripple roughness dominates, the modeled concentrations from Wikramanayake and Madsen (1991) model are lower than those from the Grant and Madsen (1982) and the Nielsen (1981) models. The Grant and Madsen (1982) model gives the highest concentration. When energy increases (Figure 4.2), concentration profiles from the three models approach to each other, however, the Grant and Madsen (1982) model still produces the highest concentrations and the Wikramanayake and Madsen (1991) produces the lowest. Under high energy conditions (Figure 4.3), the ripples are wiped out and ripple roughness is predicted to vanish by models other than the Grant and Madsen (1982) model. Bottom roughness is mainly caused by sediment motion. In this case, the concentration value of Wikramanayake and Madsen (1991) becomes higher than that of Nielsen (1981) but still lower than that of Grant and Madsen (1982). The concentration profiles from these three models are very close to each other. The fourth roughness model by Madsen et al, (1993 in press), which is only used under high energy conditions, produces much lower concentrations.

By comparing the calculated concentration profiles from all energy conditions with the measured concentration profiles (denoted by m in each panel), we find that under low and moderate energy conditions, calculated concentrations using the Grant and Madsen (1982) roughness model are the closest to the measurements. Under high energy conditions, the Madsen et al (1993, in press) roughness model offers the closest approximation to measurements. However, comparing the calculated and measured concentration will not draw the conclusion that on roughness model is better than another under a certain energy condition because concentration is also a function of the resuspension coefficient. By varying the

Figure 4.1 Comparison of measured and calculated concentration profiles for 2 bursts of low energy condition. Numerical values (1, 2, and 3) in each panel represents calculated profiles using Grant and Madsen (1982), Wikramanayake and Madsen (1991), and Nielsen (1981) roughness model respectively. m denotes measured profile.

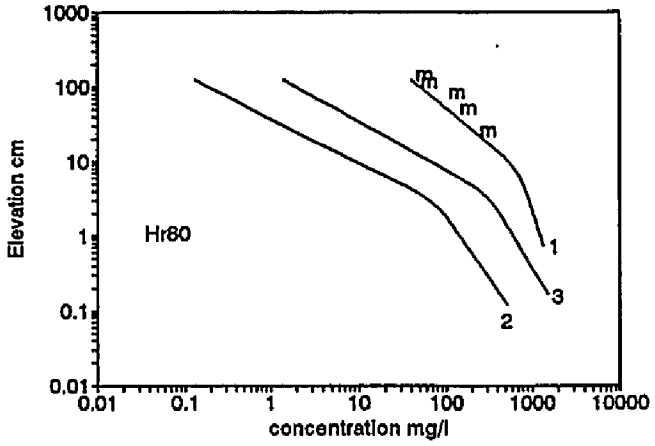
1000
100
10
1
0.1
0.01
Elevation cm
Hr80
m
m
m
m
1
2
3
0.01
0.1
1
10
100
1000
10000
concentration mg/l

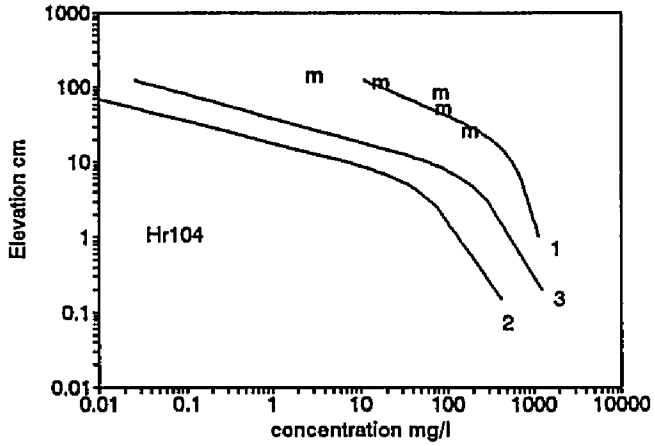
1000
100
10
1
0.1
0.01
Elevation cm
Hr104
m
m
m
m
m
1
2
3
0.01
0.1
1
10
100
1000
10000
concentration mg/l

Figure 4.2 Comparison of measured and calculated concentration profiles for 4 bursts of moderated energy condition. The notations are the same as in Figure 4.1

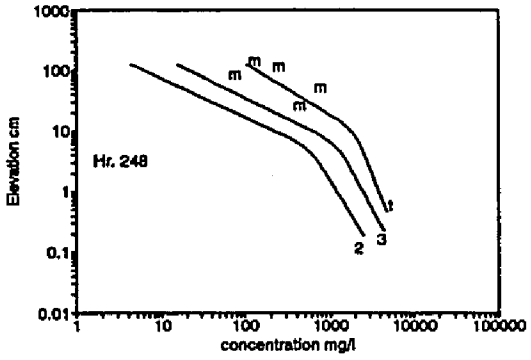
Hr. 248
Elevation cm
concentration mg/l
1000
100
10
1
0.1
0.01
1
10
100
1000
10000
100000
m
1
2
3

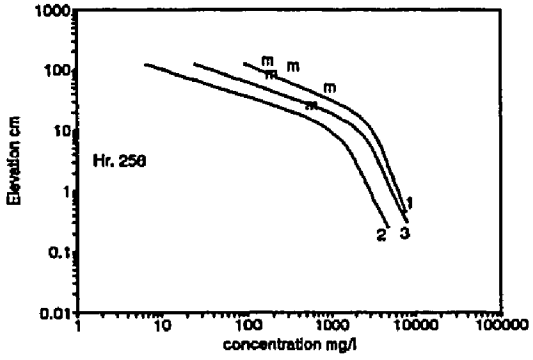
Hr. 256
Elevation cm
concentration mg/l
1000
100
10
1
0.1
0.01
1
10
100
1000
10000
100000
m
1
2
3

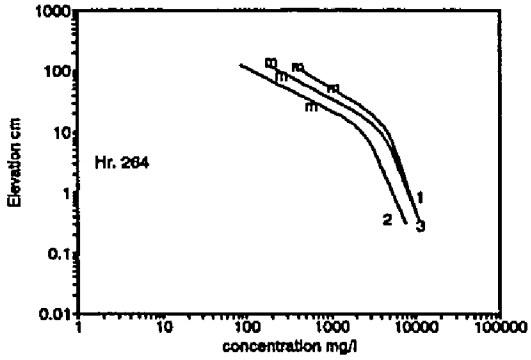
Hr. 264
Elevation cm
concentration mg/l
1000
100
10
1
0.1
0.01
1
10
100
1000
10000
100000
m
1
2
3

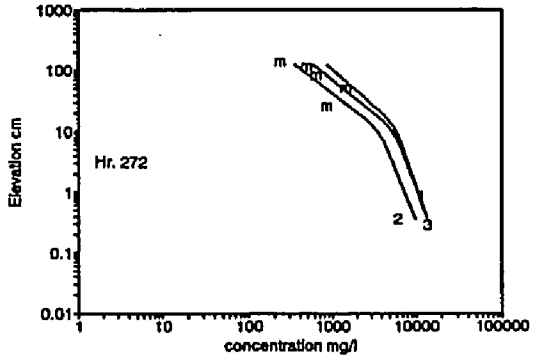
Hr. 272
Elevation cm
concentration mg/l
1000
100
10
1
0.1
0.01
1
10
100
1000
10000
100000
m
1
2
3

Figure 4.3 Comparison of measured and calculated concentration profiles for 4 bursts of high energy condition. '4' denotes the calculations using the Madsen et al (1993, in press) roughness model for high energy conditions. Other notations are the same as in Figure 4.1

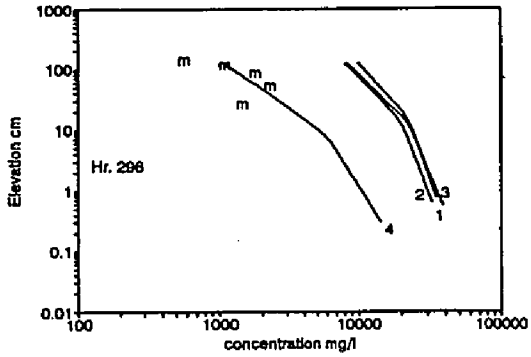
Hr. 296
Elevation cm
concentration mg/l
1000
100
10
1
0.1
0.01
100
1000
10000
100000
m
1
2
3
4

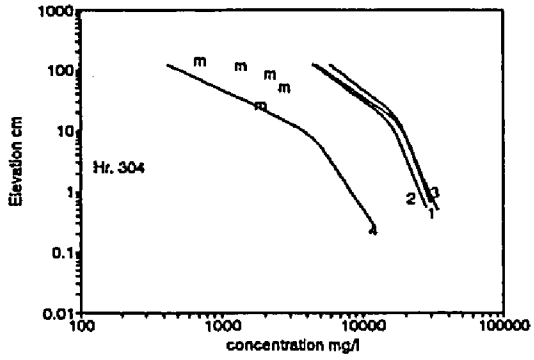
Hr. 304
Elevation cm
concentration mg/l
1000
100
10
1
0.1
0.01
100
1000
10000
100000
m
1
2
3
4

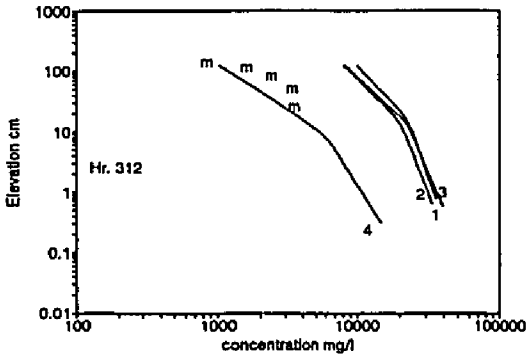
Hr. 312
Elevation cm
concentration mg/l
1000
100
10
1
0.1
0.01
100
1000
10000
100000
m
1
2
3
4

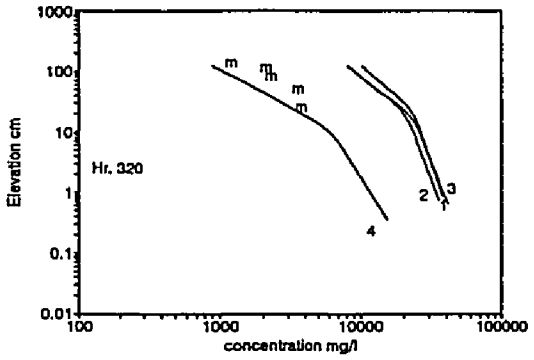
Hr. 320
Elevation cm
concentration mg/l
1000
100
10
1
0.1
0.01
100
1000
10000
100000
m
1
2
3
4

value of the resuspension coefficient, the calculated concentrations from any roughness model can match the measurements. Therefore, only the comparison of the hydrodynamics (here velocity) can tell us which roughness model is the best. Figure 4.4 shows velocity profiles calculated using the 4 roughness models discussed above. For all energy conditions, the calculated velocity profiles are roughness-model-dependent and the Grant and Madsen (1982) roughness models always gives the highest roughness and causes the highest shear in the current velocity profiles. Unfortunately, comparison of velocities under low and moderate energy conditions can not be made because the measurements are not available (reasons are discussed in the next section). However, the bottom panel of Figure 4.4 shows that the calculated velocities from the Madsen et al (1993, in press) roughness model gives the best match to the measurements. This indicates that this roughness model is the best to be used under high energy conditions. Because the Madsen et al (1993, in press) roughness model gives the best match of the concentrations as well as velocities under high energy conditions, it is appropriate to assume that the Grant and Madsen (1982) model can also give the best match of calculated and measured velocities under low energy conditions. Therefore, the Grant and Madsen (1982) roughness model is treated as the best model under low and moderate energy conditions.

4.4 A new roughness model

From the preceding discussion we know that roughness models determine whether the calculated concentration and velocity profiles are close to the measurements. It is also found that at low and moderate energy regime when the ripple roughness is most important, the Grant and Madsen (1982) roughness model yields profiles closest to the measurements. Under high energy regimes when ripples have been wiped out and sediment motion roughness

Figure 4.4 Calculated current velocity profiles for 3 example bursts (one from each energy condition). The notations are the same as in Figure 4.3

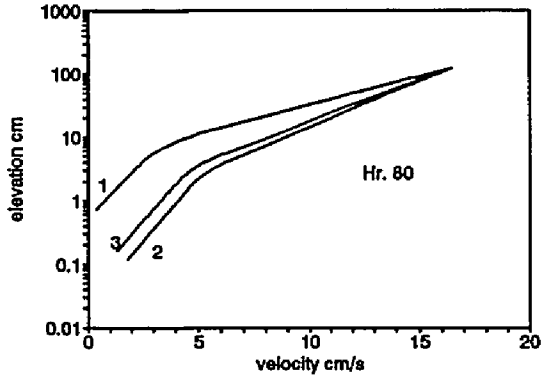
1000
100
10
1
0.1
0.01
elevation cm
0
5
10
15
20
velocity cm/s
Hr. 80
1
3
2

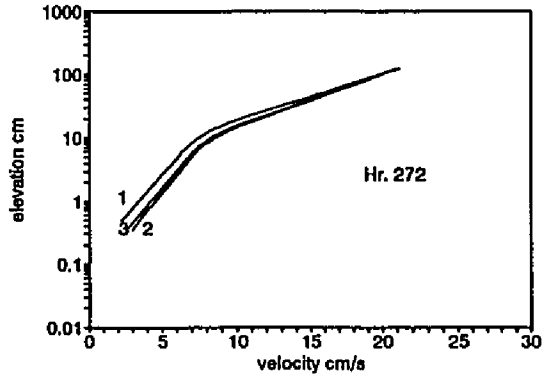
1000
100
10
1
0.1
0.01
elevation cm
0
5
10
15
20
25
30
velocity cm/s
Hr. 272
1
3
2

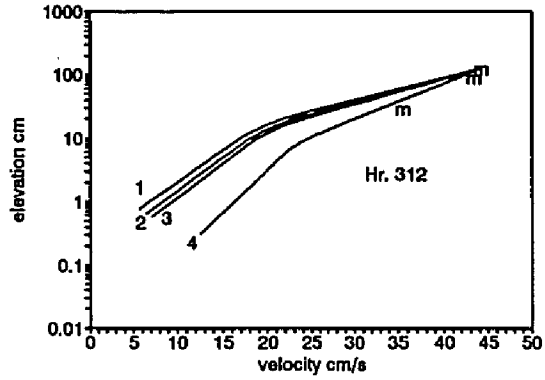
1000
100
10
1
0.1
0.01
elevation cm
0
5
10
15
20
25
30
35
40
45
50
velocity cm/s
Hr. 312
m
m
1
2
3
4

becomes the major factor, the Madsen et al (1993, in press) roughness model gives the best calculated concentration profiles. These observations suggest that a combination of the Grant and Madsen (1982) ripple roughness model and the Madsen et al' sediment motion roughness model can produce the best agreement between the calculated and measured concentration profiles at all energy levels. A new roughness model is established as follows.

When the maximum skin friction Shields parameter exceeds the critical Shields parameter, sediment motion is initiated. As ψ_m' becomes larger and larger, more and more sediment grains start moving, then ripples are generated and finally, as ψ_m' is large enough, ripples are wiped out and sheet flow occurs. Investigators have studied the criteria of sheet flow occurrence and have given different results. Katori, et al (1981) found, in their oscillatory flow tank experiments, that sheet flow occurred when ψ_m' is greater than 0.5. Wilson (1988, 1989) studied the sheet flow in a pressurized tube for steady flow and found that the ψ_m' criteria is 0.8. For values of ψ_m' greater than 0.8, the bed is found to be essentially flat, with bed-load particles moving briskly in a sheet flow layer which has thickness, δ_s, much larger than the grain size (Wilson, 1989).

Under sheet flow conditions, Wilson (1988) suggested a relation of estimating the sediment motion roughness:

$$k_{bm} = \Omega \delta_s \tag{4.28}$$

where Ω is an empirical constant which is approximately 0.5 (Wilson, 1989) and δ_s is the sheet flow thickness. δ_s is a function of sediment grain size and the maximum skin friction Shields parameter ψ_m',

$$\delta_s = f(d, \psi'_m) \tag{4.29}$$

Wilson (1988) best-fitted his data obtained from two measurements conducted in a pressurized conduit (Wilson, 1966) and showed that

$$\delta_s = 10 d \psi'_m \tag{4.30}$$

Substituting δ_s into k_{bm}, Wilson (1989) derived the sediment motion roughness in sheet flow conditions:

$$k_{bm} = 5 d \psi'_m \tag{4.31}$$

Applying Wilson's (1989) idea, Wikramanayake and Madsen (1991) analyzed the data set of Carstens, et al (1969) and ended up with a similar relation

$$k_{bm} = 60 d \psi'_m \tag{4.32}$$

It is seen that the sediment motion roughness calculated from Wikramanayake and Madsen (1991) relation is 12 times as large as that from Wilson (1989).

It is known from equations (4.31) and (4.32) that, for certain sediment, the sediment motion roughness is proportional to the magnitude of maximum skin friction Shields parameter ψ_m'. As long as ψ_m' is greater than ψ_c, sediment grains will be in motion. Since it is not certain to date how different motion (bedload, sheet flow etc.) affects the sediment motion roughness, it would be appropriate to assume a similar relation for the sediment motion roughness under all (including sheet-flow) conditions so long as ψ_m' is greater than ψ_c:

$$k_{bm} = 15 d \psi_m' \qquad \psi_m' > \psi_c \tag{4.33}$$

The right hand side of equation (4.33) is equal to the Madsen et al' roughness value multiplied by ψ_m'. It is more reasonable to have a roughness varying with the maximum skin friction Shields parameter. The constant in equation (4.33) is only a tentative value, and it can be fine-tuned by the measurements and calculations which will be discussed later in the chapter. The purpose here is to borrow the idea from the roughness formulation under sheet-flow condition (Wilson, 1988) and expand it to broader conditions (so long as the sediment motion is initiated) to form a new roughness formulation. The new roughness model can be written as

$$k_b = d + 28 \eta \left(\frac{\eta}{\lambda} \right) + 15 d \psi_m' \tag{4.34}$$

In equation (4.34), η and λ are estimated using Grant and Madsen (1982) roughness model. When $\psi_m' \leq \psi_c$, and there is no pre-existing ripples, equation (4.34) gives k_b in 1 to 2.5 times of grain diameter. This range of bed roughness values compare well with Nielsen's (1981) roughness evaluation of the flat bed (no sediment motion). When ψ_m' is greater than ψ_c but still less than the criteria for sheet flow (0.5 or 0.8), the ripple roughness dominates. Once ψ_m' is greater than the sheet flow criteria, ripples are wiped out and the bed roughness is solely dependent on ψ_m'. The roughness from equation (4.34) will be close to that of Madsen, et al (1993, in press) estimation (15 d) right at the sheet flow criteria, but will increase along with increasing ψ_m'.

With this new roughness model, the boundary layer model is run again using the same

data sets. The results are plotted in Figure 4.5 to 4.7. In 10 runs of all energy conditions, the match of the calculated profiles with the measurements are indeed improved. Most of the calculated concentration profiles are fairly close to the measurements. This improvement is also shown in the calculated current velocity profiles. Figure 4.8 shows three calculated velocity profiles along with the measurements. The measurements of current velocity for the other 7 bursts are not shown because they barely make any physical sense either due to lack of direction consistency or due to magnitude inconsistency (i.e. measured speed at lower elevation is greater than that at higher elevation). Measurements of the three bursts shown in Figure 4.8 are the only measurements that satisfy the direction and magnitude consistency (by direction consistency we mean the direction differences among the burst-averaged mean currents at 3 elevations are less than 6.0°; the magnitude consistency means that the velocity value from higher elevation is greater than that from below and the vertical velocity profile (3 points) is close to logarithmic). Two of these three bursts show comparable calculated and measured current velocity profiles. It can be concluded that the new roughness model produces calculated profiles of sediment concentration and, even though supported by only limited data, current velocity more comparable to the measurements. Therefore, the new roughness model will be used from now on.

Figure 4.5 Comparison of measured and calculated (using the new roughness model) concentration profiles for 2 bursts of low energy condition.

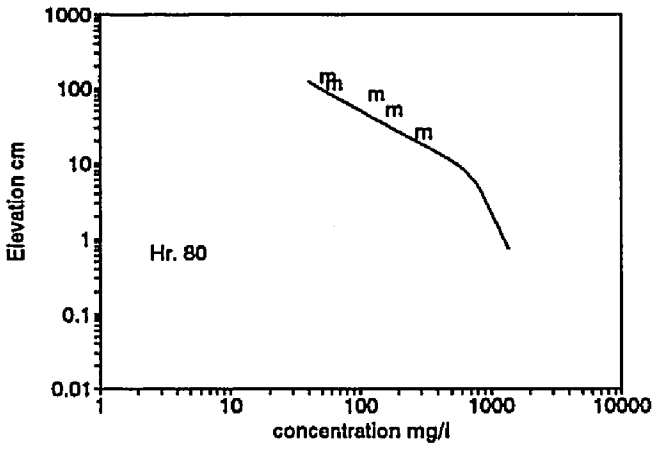
1000
100
10
1
0.1
0.01
Elevation cm
Hr. 80
1
10
100
1000
10000
concentration mg/l

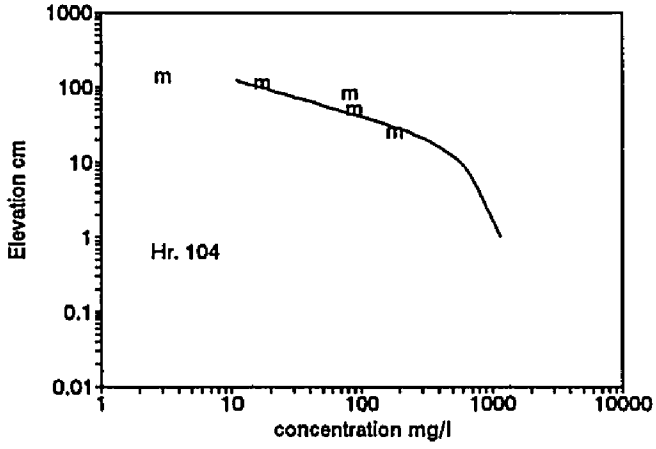
1000
100
10
1
0.1
0.01
Elevation cm
Hr. 104
1
10
100
1000
10000
concentration mg/l

Figure 4.6 Comparison of measured and calculated (using the new roughness model) concentration profiles for 4 bursts of moderate energy condition.

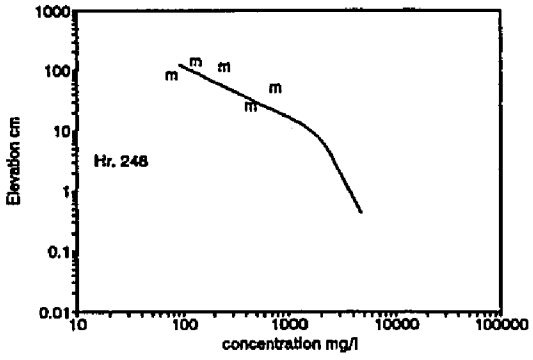
Elevation cm
1000
100
10
1
0.1
0.01
Hr. 248
10
100
1000
10000
100000
concentration mg/l

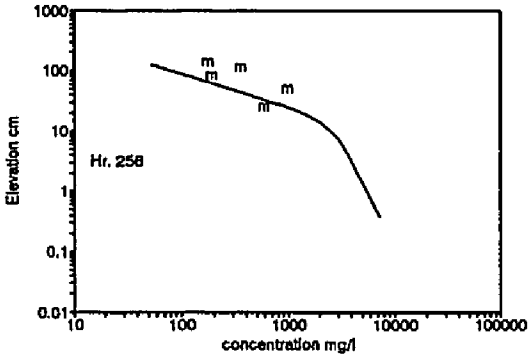
Elevation cm
1000
100
10
1
0.1
0.01
Hr. 256
10
100
1000
10000
100000
concentration mg/l

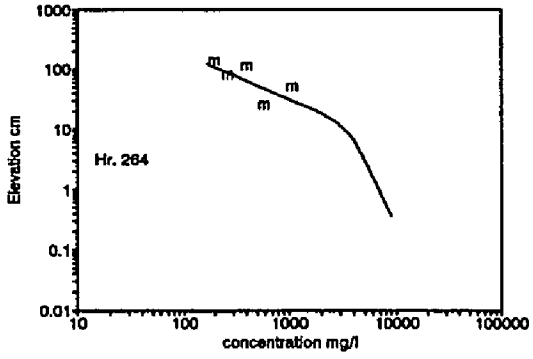
Elevation cm
1000
100
10
1
0.1
0.01
Hr. 264
10
100
1000
10000
100000
concentration mg/l

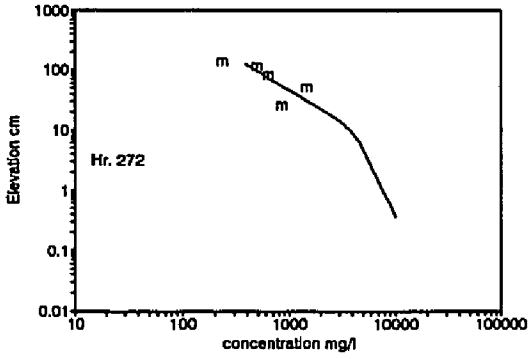
Elevation cm
1000
100
10
1
0.1
0.01
Hr. 272
10
100
1000
10000
100000
concentration mg/l

Figure 4.7 Comparison of measured and calculated (using the new roughness model) concentration profiles for 4 bursts of high energy condition.

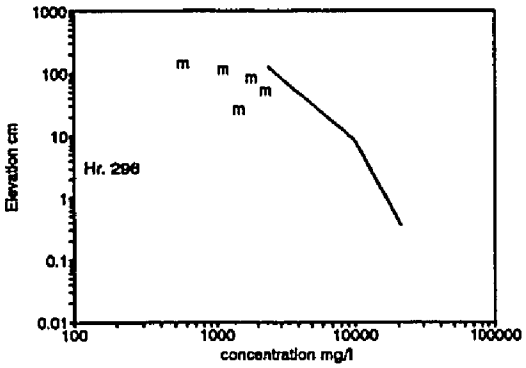
1000
100
10
1
0.1
0.01
Elevation cm
Hr. 296
m
m
m
m
m
100
1000
10000
100000
concentration mg/l

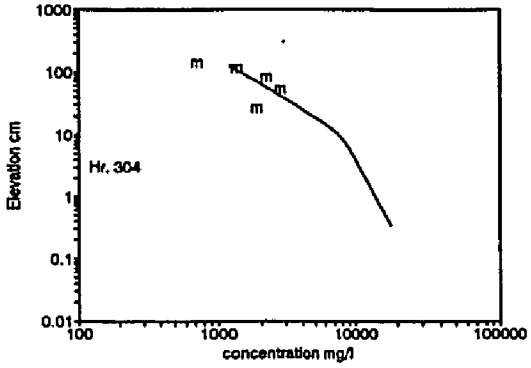
1000
100
10
1
0.1
0.01
Elevation cm
Hr. 304
m
m
m
m
m
100
1000
10000
100000
concentration mg/l

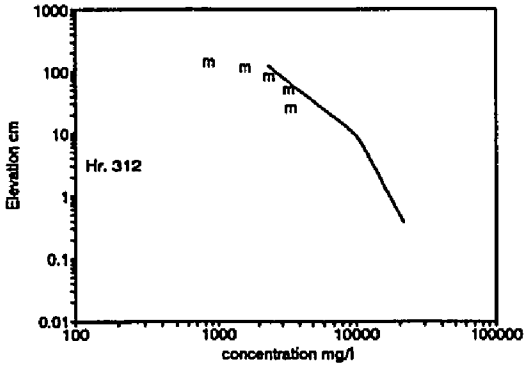
1000
100
10
1
0.1
0.01
Elevation cm
Hr. 312
m
m
m
m
m
100
1000
10000
100000
concentration mg/l

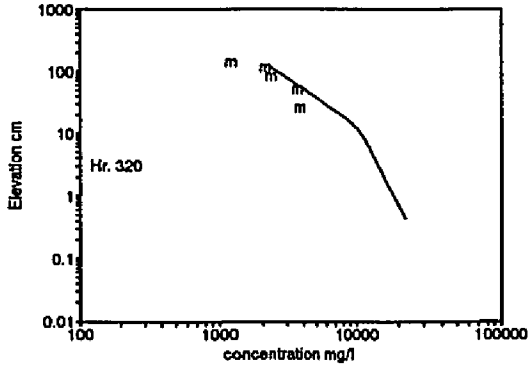
1000
100
10
1
0.1
0.01
Elevation cm
Hr. 320
m
m
m
m
m
100
1000
10000
100000
concentration mg/l

Figure 4.8 Comparison of measured and calculated (using the new roughness model) velocity profiles for 3 bursts of high energy condition.

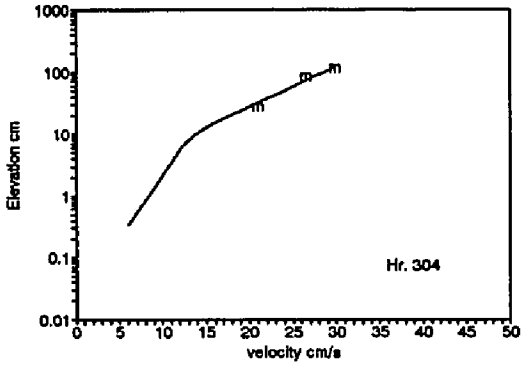
1000
100
10
1
0.1
0.01
Elevation cm
0 5 10 15 20 25 30 35 40 45 50
velocity cm/s
Hr. 304

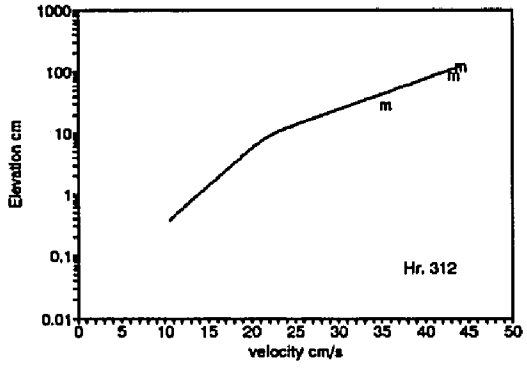
1000
100
10
1
0.1
0.01
Elevation cm
0 5 10 15 20 25 30 35 40 45 50
velocity cm/s
Hr. 312

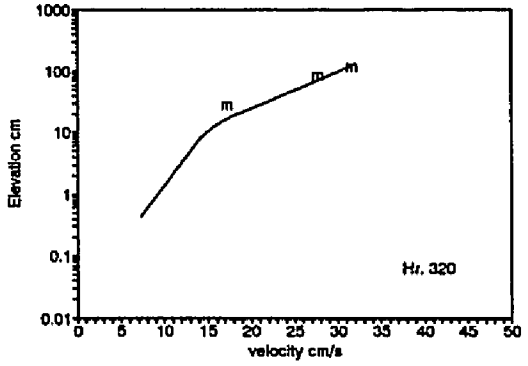
1000
100
10
1
0.1
0.01
Elevation cm
0 5 10 15 20 25 30 35 40 45 50
velocity cm/s
Hr. 320

5. EFFECTS OF STRATIFICATION AND SEDIMENT COMPOSITION ON SUSPENDED SEDIMENT CONCENTRATION PROFILES

5.1 Introduction

Suspended sediment transport is normally modeled in two ways: energetics models (following Inman and Bagnold, 1963) and tractive models (following Bjiker, 1971). In tractive models, the key is to compute the vertical profiles of the current velocity and suspended sediment concentration. With these two profiles, the sediment transport rate, q_s, can be expressed as:

$$\vec{q}_s = \int_{z_r}^{h} \vec{u}(z)\, C(z)\, dz \tag{5.1}$$

where u(z) and C(z) are the current velocity and the sediment concentration at elevation z respectively, z_r (z_0 in this study) is the reference height at which the lower bound of suspended sediment transport is located, and h is any height above z_r. In equation (5.1), the horizontal component of the sediment velocity is assumed equal to the water velocity.

The vertical profiles of velocity and concentration are influenced by many factors, among which suspended sediment induced stratification and bottom sediment composition are the most important. Since Smith and McLean (1977a, 1977b) first introduced a method of accounting for the effect of stratification, this issue has been extensively studied (Taylor and Dyer, 1977; Adams and Weatherly, 1981; Coleman, 1984; Glenn, 1983; Glenn and Grant,

1987; Vincent and Green, 1990; McLean, 1992). The effect of sediment composition is reflected by the presence of the settling velocity in the calculations of the concentration profiles. In an environment where sediments have multiple grain size, using a single grain size, e.g. D_{50}, in calculations can cause over-estimate or under-estimate of the suspended sediment concentration (Kineke and Sternberg, 1989; McLean, 1992). Although the effects of both stratification and sediment composition have been investigated separately, the relationship between these two has not been appreciated. Efforts are made in this chapter to explore this relationship and its dependence on the energy forcing (waves, currents) conditions. The boundary layer model discussed in Chapter 3 is run against 2 bursts of data in Table 2.1 (Hr80 and Hr312 which represent low and high energy conditions respectively) to demonstrate the effects of stratification and sediment composition on the suspended sediment concentration profiles. First, the two effects are studied separately in the model to see their individual influence on the sediment concentration. Then, both of them are put together to test the combined effect. The newly developed roughness model, equation (4.34) is used.

5.2 Effect of stratification

It was noted in Chapter 3, equations (3.5) and (3.6) that stable stratification reduces the turbulent eddy viscosity and eddy diffusivity. This reduction damps the upward dissipation of the turbulent energy as well as diffusion of the suspended sediments. When stable stratification exists, the calculated concentration at a given elevation will be smaller than the concentration in neutral flow.

Stratification is a complex process that depends not only the shear velocity but the sediment properties as well. For certain sediment grain sizes, very high or very low shear

velocities do not generate significant stratification. This is because when the shear velocity is very high, the concentration in the water column may also be extremely high. From the stability parameter equations (3.29), (3.31) and (3.33), we know that the stability parameter, z/L, is a function of the ratio of concentration to the shear velocity cubed. It is this ratio, which is dependent on the flow dynamics and sediment properties, that determine whether a stable stratification occurs.

The effects of stratification on suspended sediment concentration profiles are shown in Figure 5.1 and 5.2. Since stratification effect is the emphasis of this section, single grain size sediment is used in running the model discussed in Chapter 3. The single grain size diameter is the mean diameter of the bottom sediment sampled from the field. The mean grain size is 0.0117 cm and the corresponding settling velocity is 1.01 cm/s. Figure 5.1 shows the plot of concentration profiles in stratified and neutral flows under the low energy condition. $\gamma_0 = 2 \times 10^{-3}$ is used. The difference between the neutral and stratified concentration profiles is apparent. In the wave boundary layer, the stratification does not affect the suspended sediment concentration profile since, as Glenn and Grant (1987) pointed out, the stability parameter is negligibly small. Above the wave boundary layer, the stratification becomes important in affecting the concentration profile because the stability parameter becomes larger and the decay rate of the concentration is increased due to the stratification. This example indicates that, even under low energy conditions, stratification effect on concentration profile can be important.

Figure 5.2 shows profiles under high energy condition. $\gamma_0 = 1 \times 10^{-3}$ is used in this calculation. The reason for using 1×10^{-3}, instead of 2×10^{-3}, is that when the latter

resuspension value is used, the iteration of the calculating procedure (Chapter 3) never converge. This is because the stability parameter is high enough to cause the concentration above the wave boundary layer abruptly drop to as small as zero. In order to have the iteration procedure converged, we have to make compromise by using a smaller γ_0 value in the calculation under high energy conditions. Fortunately, using different γ_0 values has no conflict with our explanation of the stratification effect on the concentration profiles. Comparisons with Figure 5.1 suggest that the difference between neutral and stratified concentration profiles increases with the energy condition. Under a high energy condition (storms), the reduction of suspended sediment concentration due to the stratification is much greater than that under low energy condition even though a smaller γ_0 value is used.

Figure 5.3 shows the stability parameter profiles calculated for the 2 energy conditions. Within the wave boundary layer (δ_w = 7 and 10 cm for low and high energy conditions respectively), the stability parameters are smaller than 0.03 and therefore the stratification does not affect the sediment concentration profiles. Above the wave boundary layer, stratification effects should be considered.

5.3 Effect of sediment composition

Sediment composition affects the concentration profile through the variation of the equivalent settling velocity (average settling velocity) in the boundary layer. In a turbulent flow, after sediments of multiple grain size composition are suspended into the water column, the balance between gravity and turbulent diffusions keeps larger grain size sediments from being diffused upward as far as the smaller grain size sediments. This results in a decrease of average (or equivalent) grain size, as well as a decrease of the average (or Figure

5.1 Calculated profiles of concentration and velocity under low energy condition.

1 = neutral, 2 = stratified, m = measured. $\gamma_0=2 \times 10^{-3}$.

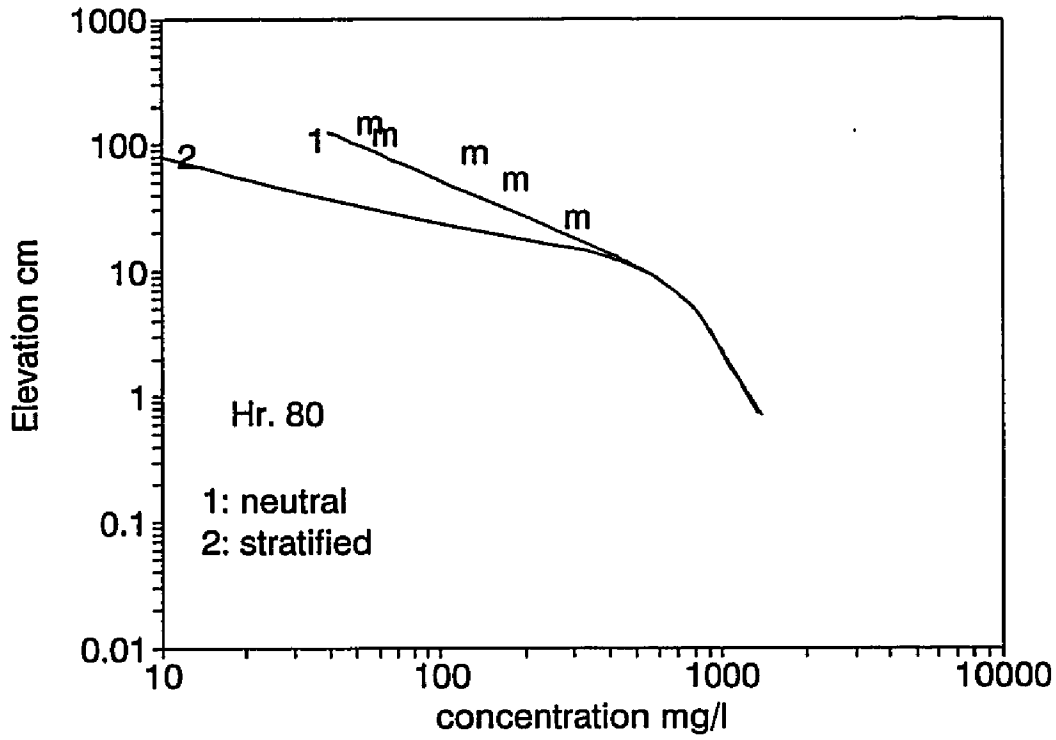
1000
100
10
1
0.1
0.01
Elevation cm
10
100
1000
10000
concentration mg/l
1
2
m
m
m
m
m
Hr. 80
1: neutral
2: stratified

Figure 5.2 Calculated profiles of concentration and velocity under high energy condition.

1 = neutral, 2 = stratified, m = measured. $\gamma_0 = 1 \times 10^{-3}$.

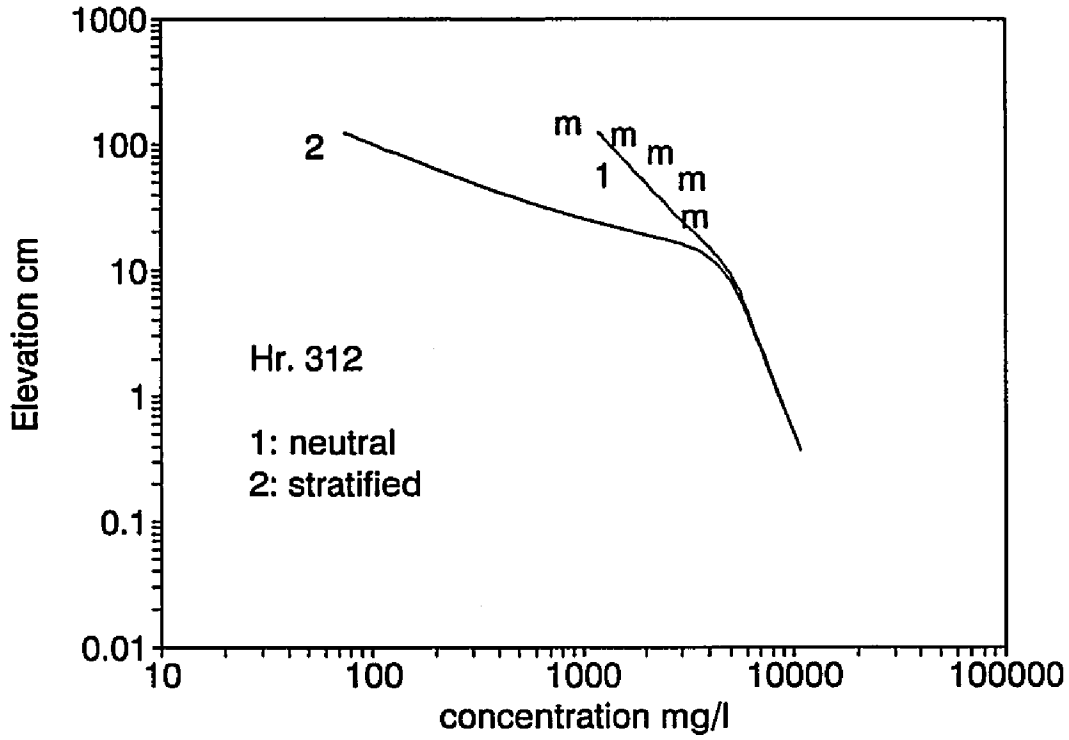
1000
100
10
1
0.1
0.01
Elevation cm
2
m
m
m
1
m
m
Hr. 312
1: neutral
2: stratified
10
100
1000
10000
100000
concentration mg/l

Figure 5.3 Calculated profiles of the stability parameter

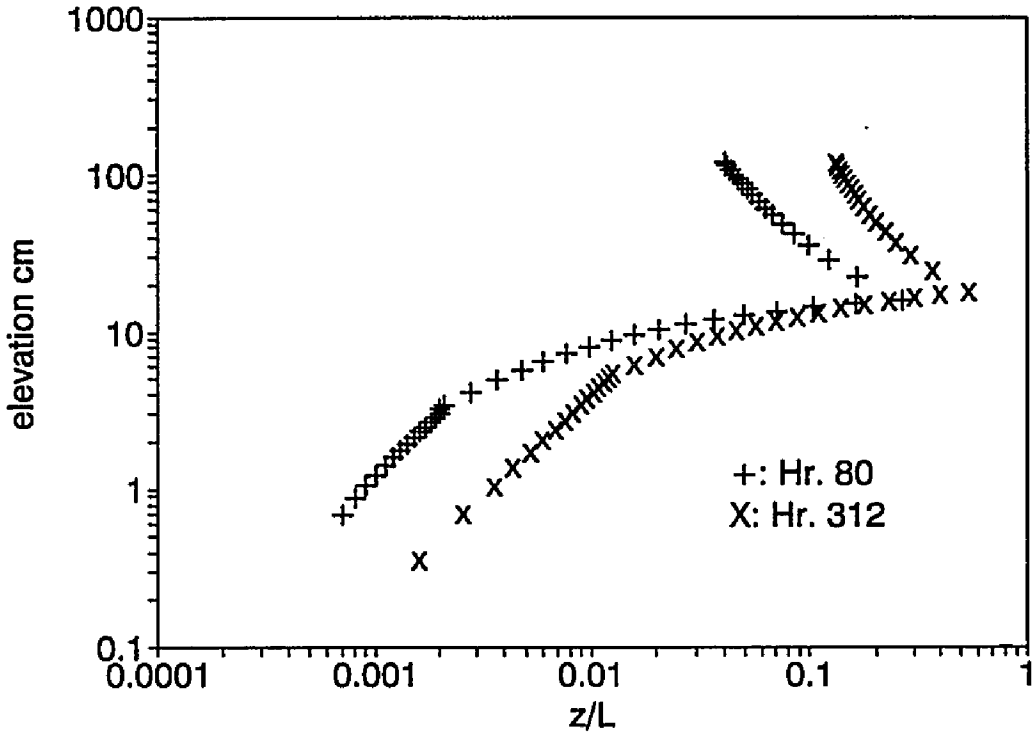
1000
100
10
1
0.1
elevation cm
0.0001
0.001
0.01
0.1
1
z/L
+: Hr. 80
X: Hr. 312

equivalent) settling velocity, from the bottom upward. This reduction of the equivalent settling velocity causes a higher or lower concentration than would prevail if settling velocity were single valued. If the single valued settling velocity is selected as the low end of the multiple grain sizes (settling velocities), the equivalent settling velocity will be larger than the single valued settling velocity and the multiple grain size sediment concentration will be lower than that of the single valued settling velocity. Conversely, if the single valued settling velocity is selected as the high end, the former concentration will be larger than the latter concentration. Normally, the single valued settling velocity is estimated by $w_f = \Sigma(f_i\, w_{fi})$, where w_{fi} is the settling velocity of the *i*th component of the sediment mixture and f_i is the fraction of that component. The equivalent settling velocity at any elevation above the bottom is always smaller than the single valued (mean grain size, e.g. d=0.0117 cm, w_f=1.01 cm/s) settling velocity. Therefore, sediment composition effects normally causes higher concentration.

Consistent with the boundary layer model discussed in Chapter 3, the prediction of settling velocity can be obtained in the three layers (which have the same definition as in the eddy viscosity model). In the bottom layer ($z < z_1$), the concentration profile for each grain size component can be written as:

$$C_{mi}(z) = C_{mi}(z_0)\left(\frac{z}{z_0}\right)^{-B_i\gamma} \exp\left(-B_i\beta\int_{z_0}^{z}\frac{dz}{L_{cw}}\right) \qquad z<z_1 \tag{5.2}$$

where i = 1 .. N is the *i*th components of the bottom sediment which is composed of N grain size components. $C_{mi}(z_0)$ is the reference concentration of the *i*th component,

$$C_{mi}(z_0) = \frac{C_{bi}\gamma_0 S_n}{1+\gamma_0 S_n} \tag{5.3}$$

where $C_{bi} = f_i C_b$ is the bed concentration of the *i*th component. B_i is the Rouse number for each individual grain size component:

$$B_i = \frac{w_{fi}}{\kappa u_{*cw}} \tag{5.4}$$

In equation (5.3), w_{fi} is the settling velocity of the *i*th component. For the middle layer, the equation used to calculate the $C_{mi}(z)$ is:

$$C_{mi}(z) = C_{mi}(z_0)\left(\frac{z_1}{z_0}\right)^{-B_i\gamma} \exp\left(-B_i\gamma\left(\frac{z}{z_1}-1\right) - \frac{B_i\beta}{z_1}\int_{z_1}^{z}\frac{z}{L_m}dz - B_i\beta\int_{z_0}^{z_1}\frac{dz}{L_{cw}}\right) \quad z_1<z<z_2 \tag{5.5}$$

For the top layer, the equation is:

$$C_{mi}(z) = C_{mi}(z_0)\left(\frac{z_1}{z_0}\right)^{-B_i\gamma}\left(\frac{z}{z_2}\right)^{-\frac{B_i\beta}{\varepsilon}} \exp\left(-B_i\gamma\left(\frac{1}{\varepsilon}-1\right) - \frac{B_i\beta}{z_1}\int_{z_1}^{z_2}\frac{z}{L_m}dz - B_i\beta\int_{z_0}^{z_1}\frac{dz}{L_{cw}} - \frac{B_i\beta}{\varepsilon}\int_{z_2}^{z}\frac{dz}{L_c}\right) \quad z>z_2 \tag{5.6}$$

At any elevation, the total concentration is simply the sum of concentrations of all grain size components

$$C_m(z) = \sum_{i=1}^{N} C_{mi}(z) \qquad i = 1 \ \ldots \ N \tag{5.7}$$

It is also necessary to bear in mind that, in equations (5.2), (5.5) and (5.6), z/L_{cw}, z/L_m, and z/L_c (the stability parameters in the bottom, middle and top layer respectively) are all functions of settling velocity. The procedure of running the model is just like the procedure in the previous section. Stratification is assumed equal to zero because the effect of

multiple grain sizes is emphasized in this section. The concentration of each grain size class is calculated using equations (5.2), (5.5) and (5.6) and then the total concentration profile is estimated using equation (5.7). The equivalent settling velocity profile can be estimated as follows:

$$w_f(z) = \sum \{f_i(z) w_{fi}\} \tag{5.8}$$

where $w_f(z)$ is the equivalent settling velocity at elevation z, $f_i(z)$ is the fraction of the *i*th grain size class at z, and $w_{fi}(z)$ is the settling velocity of that grain size class.

To calculate the concentration profile affected by the sediment composition, the composition data of the multiple grain size classes must be known in addition to the data used in section 5.2. The sediment composition used in the calculation is shown in Table 5.1. The information in Table 5.1 is obtained by analyzing the field bottom sediments in the laboratory. The field sediments are first wet-sieved to separate the fine ($> 4\ \phi$) and coarse fractions. As stated in Chapter 2, there are about 20% of fine sediments. The coarse fraction is then analyzed using an automated settling tube. Four histograms of coarse sediment are plotted in Figure 5.4. The percentage of the five grain size members of the coarse fraction are obtained by averaging 4 samples for each of the 5 grain size classes.

In order to emphasize the effect of sediment composition on the suspended sediment concentration profile, the stratification effect is not involved, i.e., neutral hydrodynamic model is used, in the calculations of this section. Figure 5.5 and 5.6 are plots of the calculated concentration profiles under low and high energy conditions showing the effect of differing sediment compositions. Presence of multiple grain size significantly changes the concentration profiles in both cases. Comparing the concentration profiles obtained using a

Table 5.1 Composition of bottom sediment at the Duck site

Class	1	2	3	4	5	6	Weighted Average
Size(cm)	0.005	0.009	0.0105	0.0125	0.015	0.018	0.0117
%	20	8	13	26	20	13	
w_f(cm/s)	0.26	0.63	0.84	1.09	1.42	1.81	1.01

Figure 5.4 Histogram of 4 bottom sediment samples taken from the Duck site.

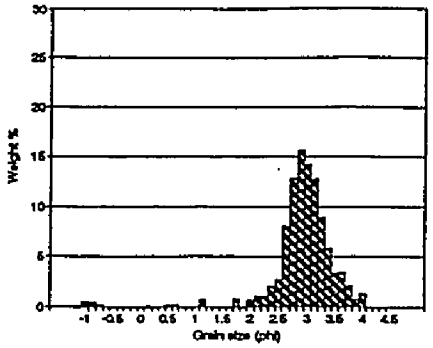
Weight %
Grain size (phi)

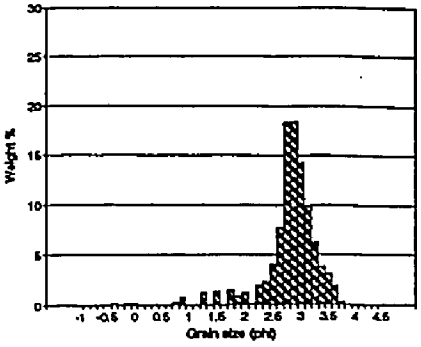
Weight %
Grain size (phi)

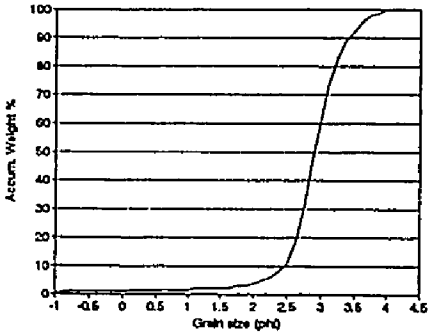
Accum. Weight %
Grain size (phi)

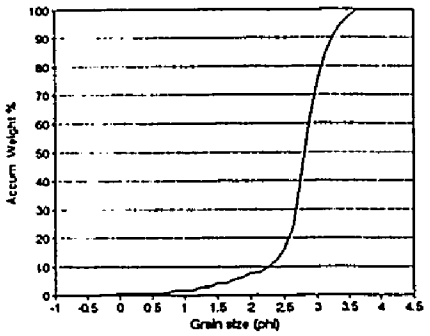
Accum. Weight %
Grain size (phi)

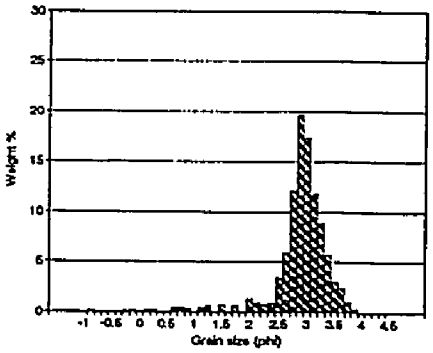
Weight %
Grain size (phi)

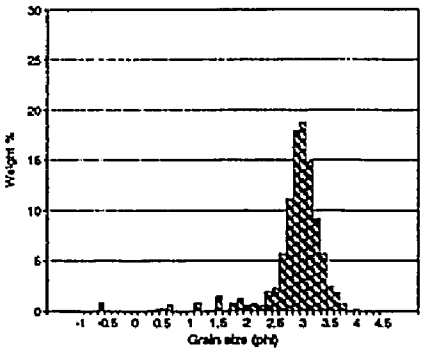
Weight %
Grain size (phi)

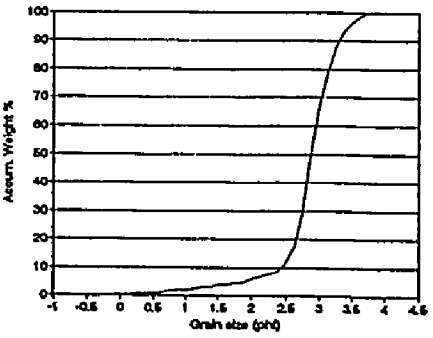
Accum. Weight %
Grain size (phi)

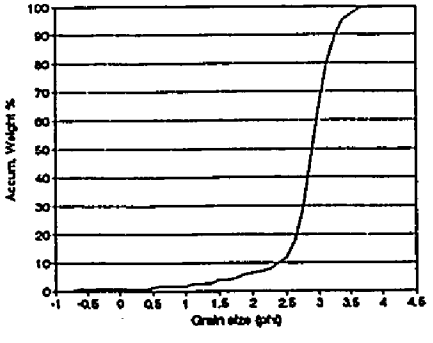
Accum. Weight %
Grain size (phi)

single valued settling velocity (settling velocity of the mean grain size), the suspended sediment concentrations increase under both low and high energy conditions due to the effects of the sediment composition, except at the very bottom of the Figure 5.5 (this is a special case when the equivalent settling velocity is larger than the single valued settling velocity (1.01 cm/s); the cause of this is explained in the next paragraph, accompanying Figure 5.7). However, the increasing magnitude (relative to the neutral concentration profiles) of the concentration decreases from low energy condition to high energy condition. The reason for this is obviously that when u_{*cw} approaches larger value, the differences in the individual Rouse number B_i, equation (5.3), become smaller. When u_{*cw} is very large (much greater than w_{fi}), the Rouse number is always very small. No matter what the sediment composition is and how different between w_{fi} and the single valued settling velocity, the effect of the sediment composition will diminish.

The increase of suspended concentration due to the use of multiple grain size are caused by the decreasing settling velocity from the bottom to the top. The equivalent settling velocity profiles for both energy conditions considered here are plotted in Figure 5.7. The settling velocity has a lower gradient in high energy conditions, when relative variations of B_i among grain size classes are smaller, than in low energy conditions, when grain size effects on B_i are more significant. The offset of the equivalent settling velocity at the lower bond is caused by the multiple grain size composition of bed sediment and magnitude of difference between the maximum skin friction Shields parameter ψ_m' and critical Shields parameter ψ_c. Under low energy conditions, the magnitude of $(\psi_m'-\psi_c)$ is small relative to the magnitude of ψ_c. Therefore, the suspension of the bed sediments is sensitive to the variation of $(\psi_m'-\psi_c)$. Because the largest grain size has the lowest ψ_c value (so the value of $(\psi_m'-\psi_c)$ is the largest),

the percentage of the largest grain size is relatively high under low wave energy conditions compared to that under high energy condition in which the suspension of the bed sediments is not so sensitive to the variation of $(\psi_m'-\psi_c)$ because the magnitude of $(\psi_m'-\psi_c)$ is large relative to ψ_c. The relative high percentage of larger grain size classes results in the equivalent settling velocity being greater than the weighted average settling velocity of the bottom sediments (1.01 cm/s). This explains why the multiple grain size concentration is smaller than the single grain size concentration in Figure 5.5.

The cause of the decreasing equivalent settling velocity can be seen from Figure 5.8 in which the percentages of all sediment classes at each elevation are plotted. It is clearly seen that the percentage of the finest class (0.005 cm) increases faster under the low energy condition than under the high energy condition. This is more clearly shown in Figure 5.9, where each grain size class is plotted separately. For the first class (0.005 cm), there are less within the wave boundary layer under low energy condition than under high energy condition; however, its percentage increases upward more rapidly under low energy condition than under high energy condition. For grain size class 2 and 3, their percentages at the bottom are almost the same under low and high energy conditions, but at the top, their percentage are greater under high energy condition than under low condition. For each of grain size class 4, 5, and 6, the distributions are the reverse of the distribution of grain size class 1, i.e., there is less of these classes within, or slightly above the wave boundary layer, under high energy condition than under low energy condition; and there is more of these classes above the wave boundary layer under high energy condition. These differences of contents of grain size classes at each elevation also explains the offset of the equivalent settling velocity at the bottom of Figure 5.7.

Figure 5.5 Calculated concentration profiles under low energy condition.

1 = single grain size (= mean size), 2 = multiple grain size. $\gamma_0=2 \times 10^{-3}$.

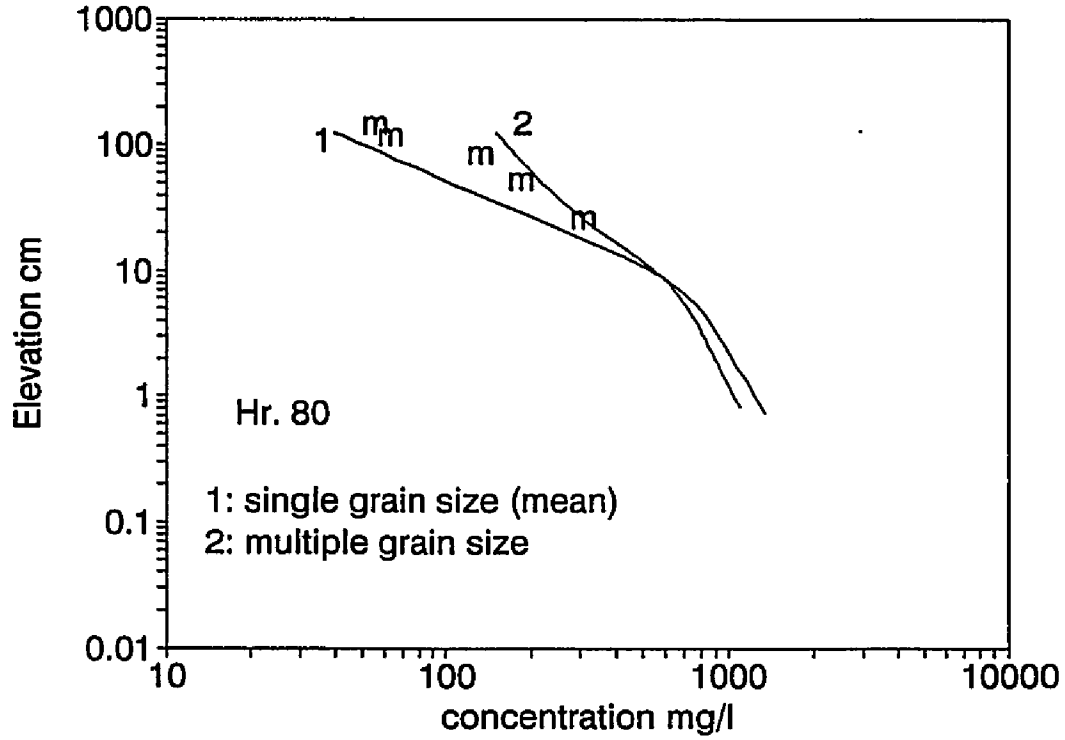
1000
100
10
1
0.1
0.01
Elevation cm
10
100
1000
10000
concentration mg/l
1
2
m
Hr. 80
1: single grain size (mean)
2: multiple grain size

Figure 5.6 Calculated concentration profiles under high energy condition.

1 = single grain size (=mean size), 2 = multiple grain size. $\gamma_0 = 1 \times 10^{-3}$.

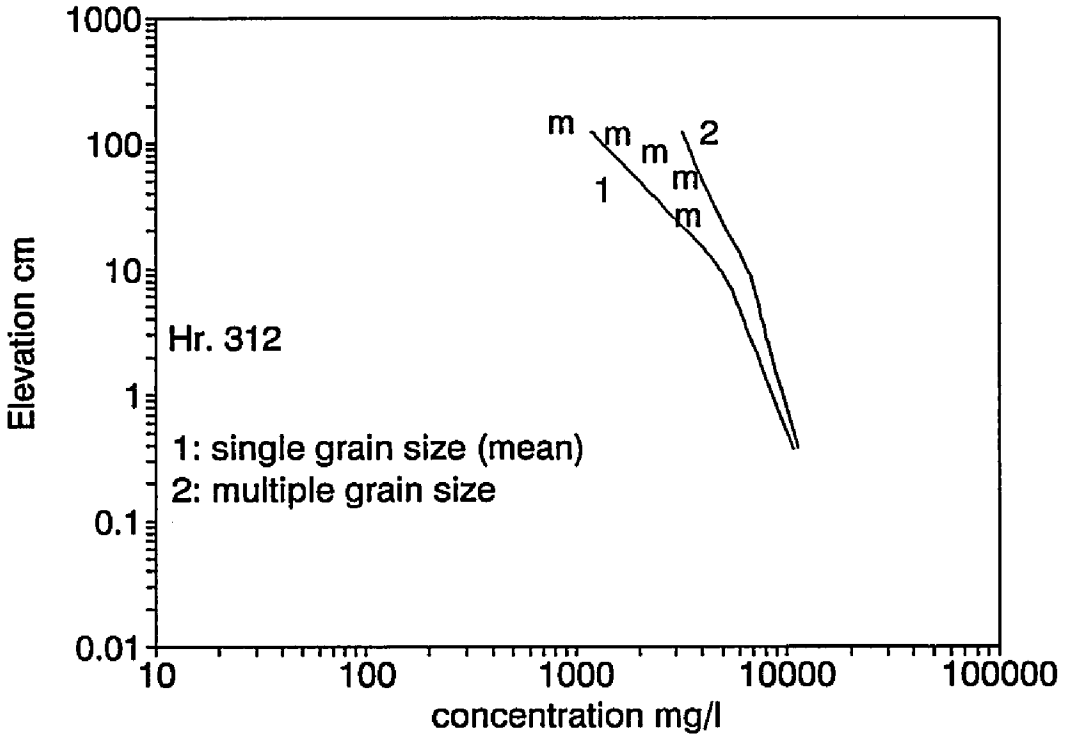
1000
100
10
1
0.1
0.01
Elevation cm
Hr. 312
1: single grain size (mean)
2: multiple grain size
m
m
m
2
1
m
m
10
100
1000
10000
100000
concentration mg/l

Figure 5.7 Calculated profiles of the equivalent settling velocity

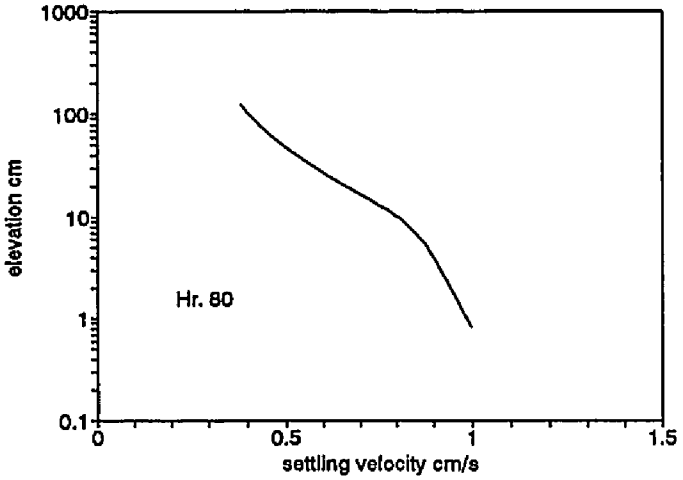
1000
100
10
1
0.1
elevation cm
Hr. 80
0
0.5
1
1.5
settling velocity cm/s

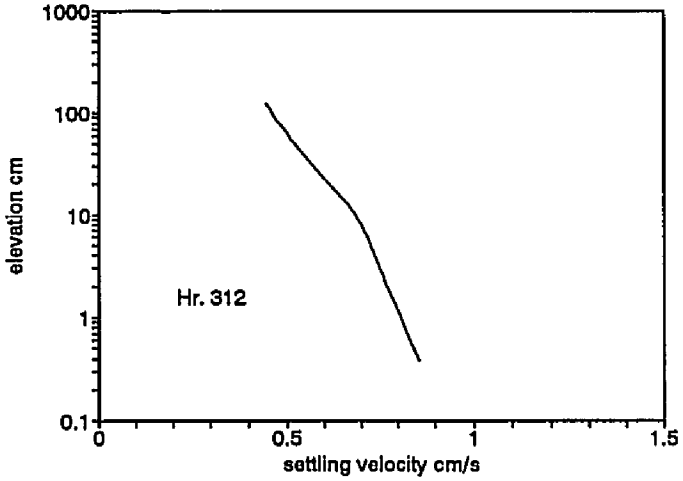
1000
100
10
1
0.1
elevation cm
Hr. 312
0
0.5
1
1.5
settling velocity cm/s

Figure 5.8 Percentage of each grain size classes plotted vs elevation

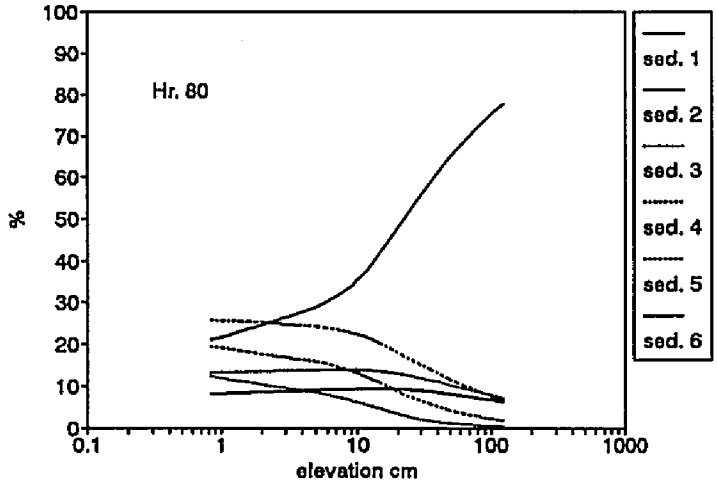
Hr. 80
%
elevation cm
sed. 1
sed. 2
sed. 3
sed. 4
sed. 5
sed. 6

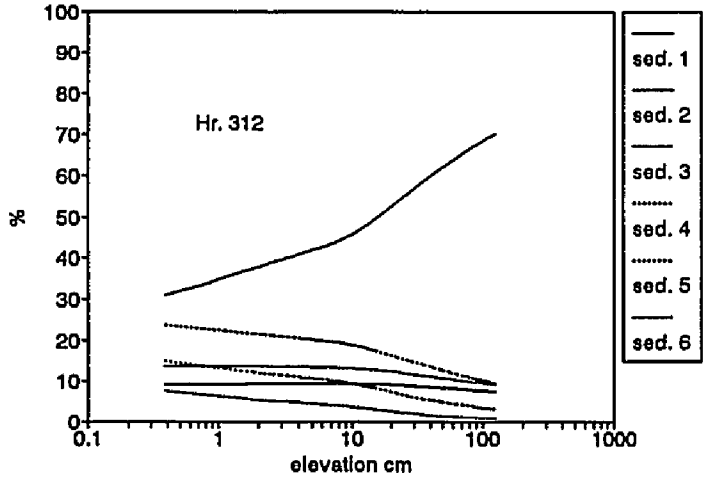
Hr. 312
%
elevation cm
sed. 1
sed. 2
sed. 3
sed. 4
sed. 5
sed. 6

Figure 5.9 Profiles of percentage of all grain size classes.

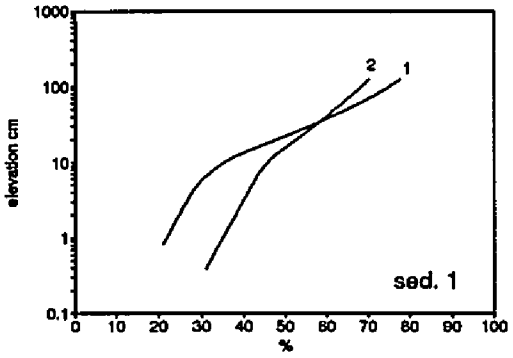
elevation cm
1000
100
10
1
0.1
0 10 20 30 40 50 60 70 80 90 100
%
1
2
sed. 1

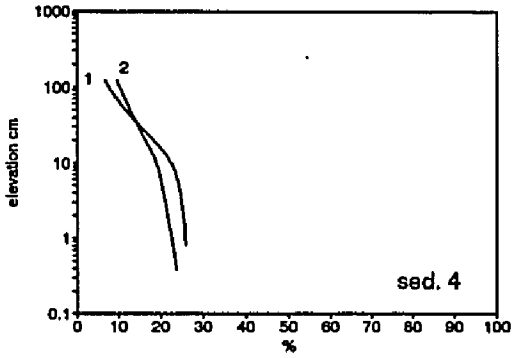
elevation cm
1000
100
10
1
0.1
0 10 20 30 40 50 60 70 80 90 100
%
1
2
sed. 4

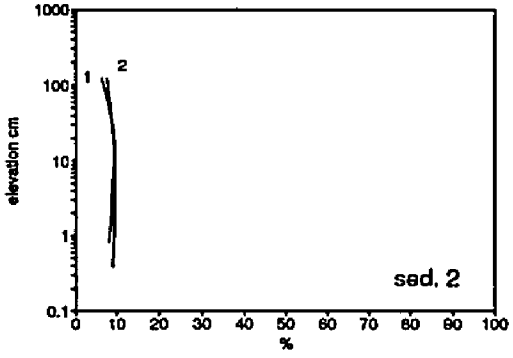
elevation cm
1000
100
10
1
0.1
0 10 20 30 40 50 60 70 80 90 100
%
1
2
sed. 2

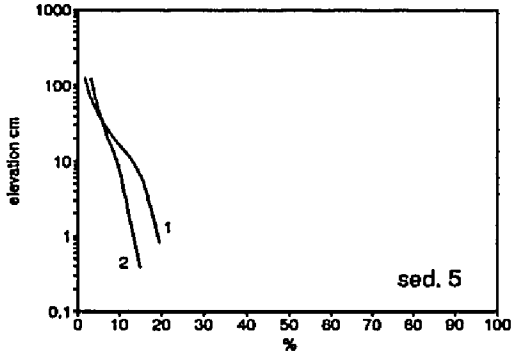
elevation cm
1000
100
10
1
0.1
0 10 20 30 40 50 60 70 80 90 100
%
1
2
sed. 5

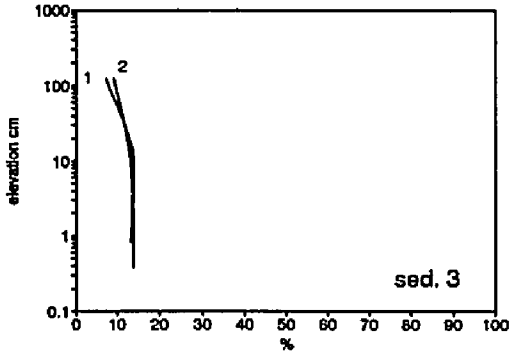
elevation cm
1000
100
10
1
0.1
0 10 20 30 40 50 60 70 80 90 100
%
1
2
sed. 3

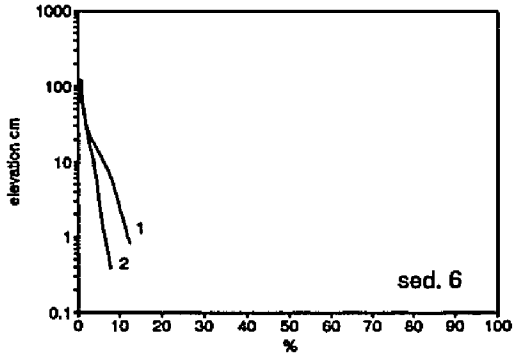
elevation cm
1000
100
10
1
0.1
0 10 20 30 40 50 60 70 80 90 100
%
1
2
sed. 6

5.4 Summary and discussions

From the preceding discussions based on our field data, we see that the effects of stratification and sediment composition have opposing effects. While the effect of stratification tends to reduce the concentration, the sediment composition effect enhances the concentration. We also see that this opposing effect varies with the energy conditions. To depict this more clearly, the profiles of suspended sediment concentration calculated using: (1) single grain size (d=0.0117 cm) in neutral flow, and (2) multiple grain size in stratified flow (more natural) are plotted in Figure 5.10. γ_0 is assumed equal to 2×10^{-3} for low energy condition and 1×10^{-3} for high energy condition in order to keep consistency with the discussions in section 5.2. This figure shows the combined effects of stratification and sediment composition on the concentration profiles of both low and high energy conditions. It is clear in Figure 5.10 that the combined effect also depends on the energy conditions. In the low energy situations (top panel), the effect of sediment composition outweighs the effect of stratification in almost the entire profile (except in the very bottom, which has been explained in the previous section) and causes a net increase of suspended sediment concentration. Under high energy condition (bottom panel), however, the profile is more complicated. Within and slightly above the wave boundary layer, the sediment composition effect dominates because the stratification is negligible in this region. A net increase of the concentration occurs. Above the wave boundary layer, where the stratification is expected important, there is a net decrease of the concentration because the effect of sediment composition is not as important as that of stratification.

Figure 5.11 shows profiles of equivalent settling velocity when both stratification and sediment composition effect are involved. Comparing to Figure 5.7, the profiles are almost

the same within the wave boundary layer because the stratification involvement does not change neither the concentration nor the composition of the suspended sediments by much. Above the wave boundary layer, the stratification further inhibits the upward diffusion of larger grain size classes and cause rapid decrease of the equivalent settling velocity. At the top of the profiles, the equivalent settling velocity is close to the settling velocity of the finest grain size class (0.26 cm/s), which means that 100% of the suspended sediment are this grain size class. This can also be seen from Figure 5.12, where the percentage profiles of each grain size classes are plotted.

These conclusions were drawn from the calculations using the data from our field experiments. They apply to general continental shelf environments with multiple grain size sediments whose grain size distribution is close to normal (Gaussian distribution). However, the grain sizes are not normally distributed in some special cases. The following is dedicated to examine the sediment composition effect when the grain size distribution is either extremely negatively skewed or positively skewed.

Input variables of Hr80 (low energy condition) and Hr312 (high energy condition) from Table 2.1 are used again. The composition and distribution of two "synthesized" sediment samples are listed in Table 5.2 and plotted in Figure 5.13. In order to have the same sediment composition of the field data, the weighted average grain size are not identical from case to case. This is because both "same grain size composition" and "different skewness with the same average grain size" can not be satisfied at the same time. The calculated concentration profiles are plotted in Figure 5.14 and 5.15. It is noticed that, for both positive and negative skewed grain size distributions, the effect of sediment composition

Figure 5.10 Calculated concentration profiles under low(top panel) and high (bottom panel) energy conditions. m = measured.

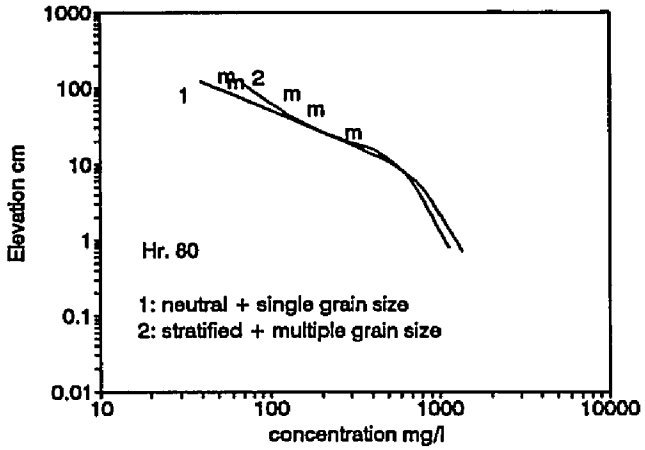
1000
100
10
1
0.1
0.01
Elevation cm
10
100
1000
10000
concentration mg/l
1
2
Hr. 80
1: neutral + single grain size
2: stratified + multiple grain size

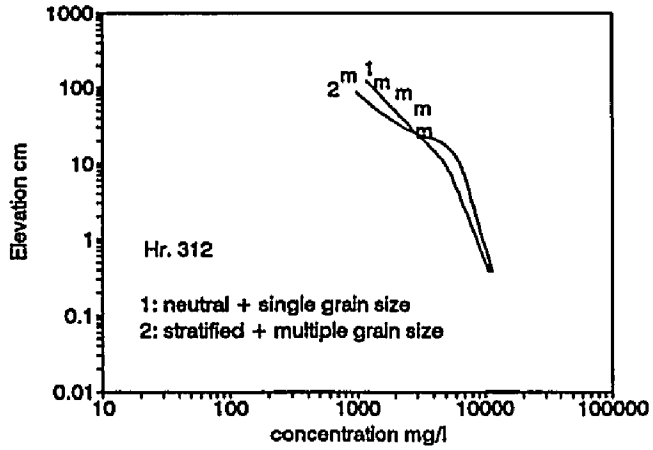
1000
100
10
1
0.1
0.01
Elevation cm
10
100
1000
10000
100000
concentration mg/l
2
1
Hr. 312
1: neutral + single grain size
2: stratified + multiple grain size

Figure 5.11 Calculated profiles of the equivalent settling velocity

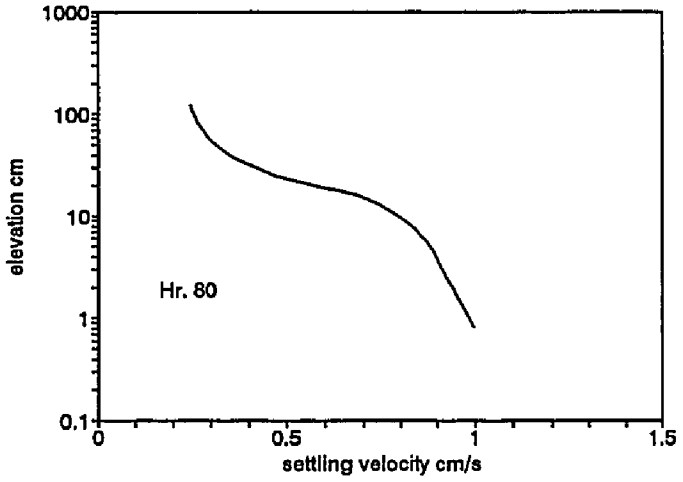
1000
100
10
1
0.1
elevation cm
Hr. 80
0
0.5
1
1.5
settling velocity cm/s

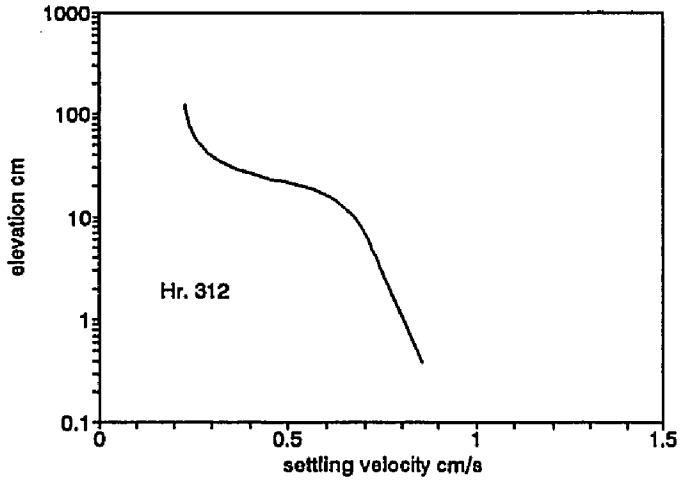
1000
100
10
1
0.1
elevation cm
Hr. 312
0
0.5
1
1.5
settling velocity cm/s

Figure 5.12 Percentage of each grain size classes plotted vs elevation

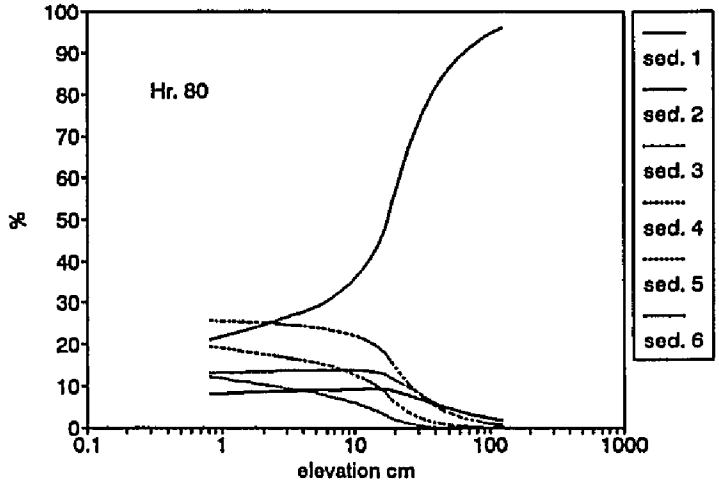
Hr. 80
%
elevation cm
sed. 1
sed. 2
sed. 3
sed. 4
sed. 5
sed. 6

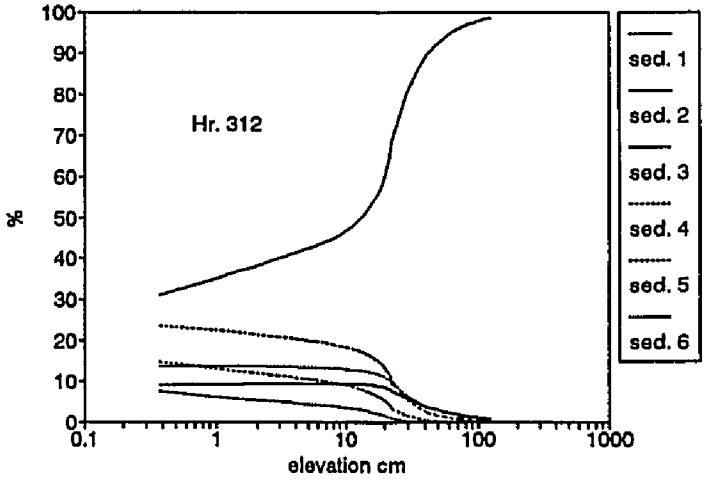
Hr. 312
%
elevation cm
sed. 1
sed. 2
sed. 3
sed. 4
sed. 5
sed. 6

on the concentration profiles increases the sediment concentration relative to the single grain size prediction at any elevations, which is like the results from the normally distributed sediments (The offset of the concentrations at the lower part of each profile pairs in Figure 5.14 has been explained in section 5.3). However, since the weighted average grain size are different in positively- and negatively- skewed samples, the concentration profiles of the two samples can not be compared. Instead, the differences between profile 1 and profile 2 in each panel of Figure 5.14 and 5.15 are examined. Under low energy condition (Figure 5.14), the positively skewed grain size distribution causes more increase of concentration than the negatively skewed grain size distribution. For example, at the top end of the profiles, the concentration increased from 80 mg/l to 290 mg/l in positively skewed sediment and from 30 mg/l to 70 mg/l in the negatively skewed sediment. This is because there are 40% of silt and clay, whose grain size (0.005 cm) is smaller than the weighted average grain size (0.0089 cm), in the positively skewed sediment. In the negatively skewed sediment, although there are 35% (6% + 8% + 12%) of grain sizes smaller than the weighted average grain size, there is only 6% of silt and clay. As we have shown in section 5.3, it is the clay and silt which are dominant at the upper part of the profile. Therefore, considering the sediment composition effect will create more difference in the calculated concentration profile for positively skewed sediment than for negatively skewed sediment. Under high energy condition (Figure 5.15), it is similarly shown that the positively skewed distribution creates more concentration increase than the negatively skewed distribution does. At the top end of the profiles, the concentration increase from 2000 mg/l to 6000 mg/l for the positively skewed sediment and from 700 mg/l to 1700 mg/l for the negatively skewed sediment.

Figure 5.16 and 5.17 show the equivalent settling velocities. Under the same energy

condition, the equivalent settling velocity profile has larger vertical gradient when the sediment's grain size distribution is negatively skewed. This is because, when the sediment distribution is negatively skewed, the majority large grain size sediment will not be diffused as high as the minority smaller grain size sediment. Conversely, when the skewness is positive, the majority finer grains can be diffused far above the bottom and the average grain size in the water column does not vary as much as in the negatively skewed situation. For the same sediment (positively or negatively skewed), the vertical gradient of the equivalent settling velocity profile becomes smaller under the high energy condition than under the low energy condition. As explained in section 5.3, under the high energy condition, the strong turbulence can diffuse larger grain size to elevations where the same grain size can not approach under the low energy condition. This increases the equivalent settling velocity at higher elevations and decreases the vertical gradient of the equivalent settling velocity profile.

Table 5.2 Compositions of two "synthesized" samples with skewed distributions

Positively skewed sample

Class	1	2	3	4	5	6	Weighted Average
Size(cm)	0.005	0.009	0.0105	0.0125	0.015	0.018	0.0089
%	40	25	12	9	8	6	
w_f(cm/s)	0.26	0.63	0.84	1.09	1.42	1.81	0.68

Negatively skewed sample

Class	1	2	3	4	5	6	Weighted Average
Size(cm)	0.005	0.009	0.0105	0.0125	0.015	0.018	0.0144
%	6	8	9	12	25	40	
w_f(cm/s)	0.26	0.63	0.84	1.09	1.42	1.81	1.35

Figure 5.13 Three different histograms of bottom sediment. The top panel shows the sediment distribution from the Duck site, the middle and bottom panels show two extremely skewed distributions.

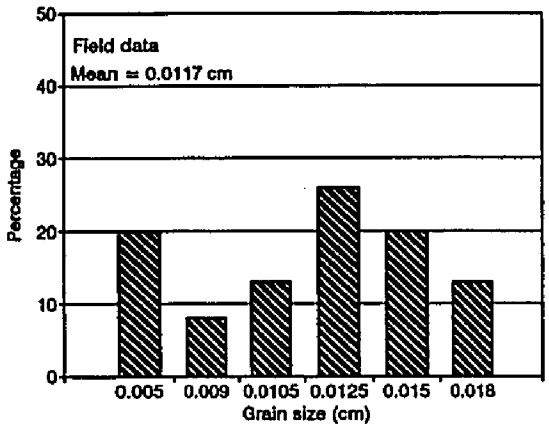
Field data
Mean = 0.0117 cm
Percentage
50
40
30
20
10
0
0.005
0.009
0.0105
0.0125
0.015
0.018
Grain size (cm)

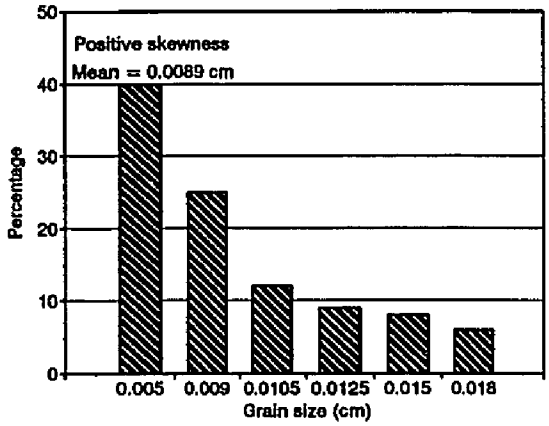
Positive skewness
Mean = 0.0089 cm
Percentage
50
40
30
20
10
0
0.005
0.009
0.0105
0.0125
0.015
0.018
Grain size (cm)

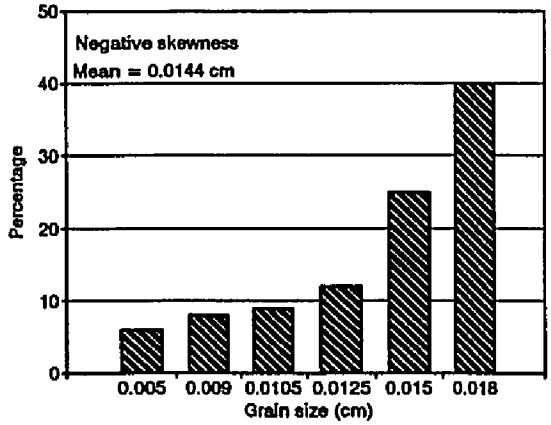
Negative skewness
Mean = 0.0144 cm
Percentage
50
40
30
20
10
0
0.005
0.009
0.0105
0.0125
0.015
0.018
Grain size (cm)

Figure 5.14 Calculated concentration profiles under low energy condition showing the difference of the sediment composition effect due to different skewness.

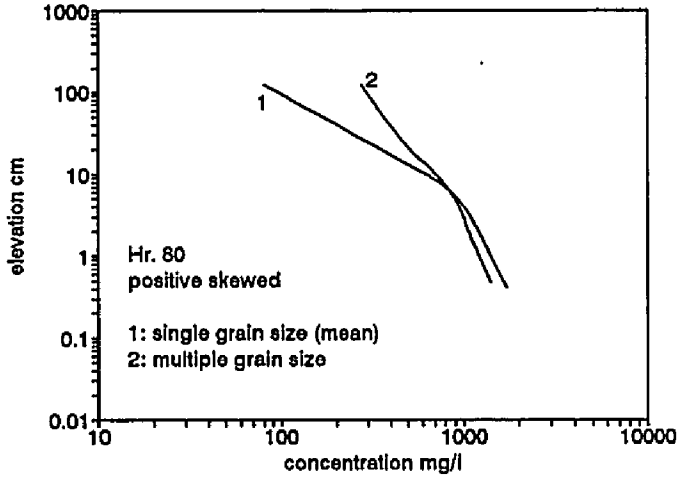
1000
100
10
1
0.1
0.01
elevation cm
1
2
Hr. 80
positive skewed
1: single grain size (mean)
2: multiple grain size
10
100
1000
10000
concentration mg/l

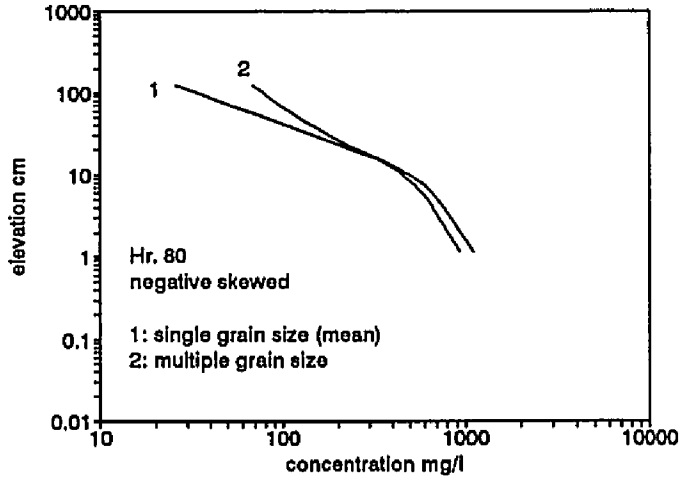
1000
100
10
1
0.1
0.01
elevation cm
1
2
Hr. 80
negative skewed
1: single grain size (mean)
2: multiple grain size
10
100
1000
10000
concentration mg/l

Figure 5.15 Calculated concentration profiles under high energy condition showing the difference of the sediment composition effect due to different skewness.

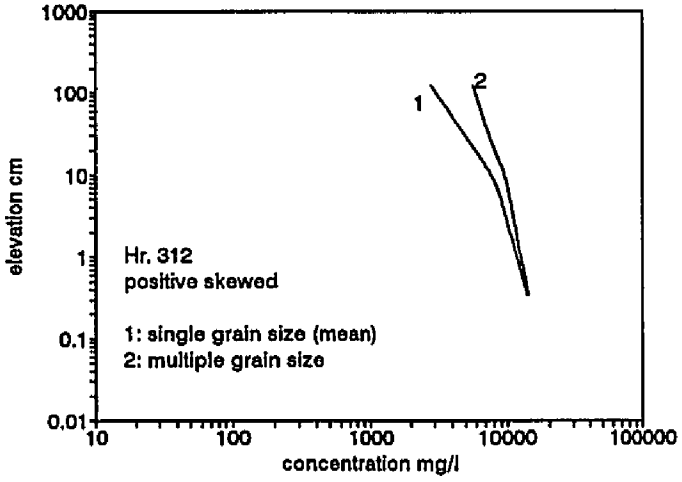
1000
100
10
1
0.1
0.01
elevation cm
Hr. 312
positive skewed
1: single grain size (mean)
2: multiple grain size
1
2
10
100
1000
10000
100000
concentration mg/l

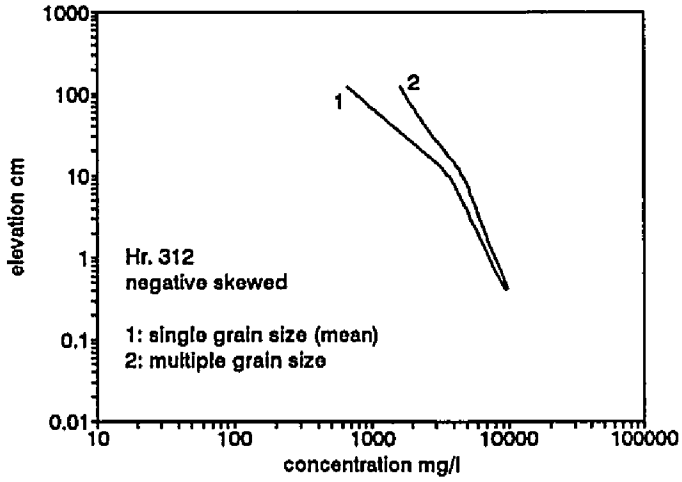
1000
100
10
1
0.1
0.01
elevation cm
Hr. 312
negative skewed
1: single grain size (mean)
2: multiple grain size
1
2
10
100
1000
10000
100000
concentration mg/l

Figure 5.16 Calculated profiles of equivalent settling velocity under low energy condition showing the difference of the sediment composition effect due to different skewness.

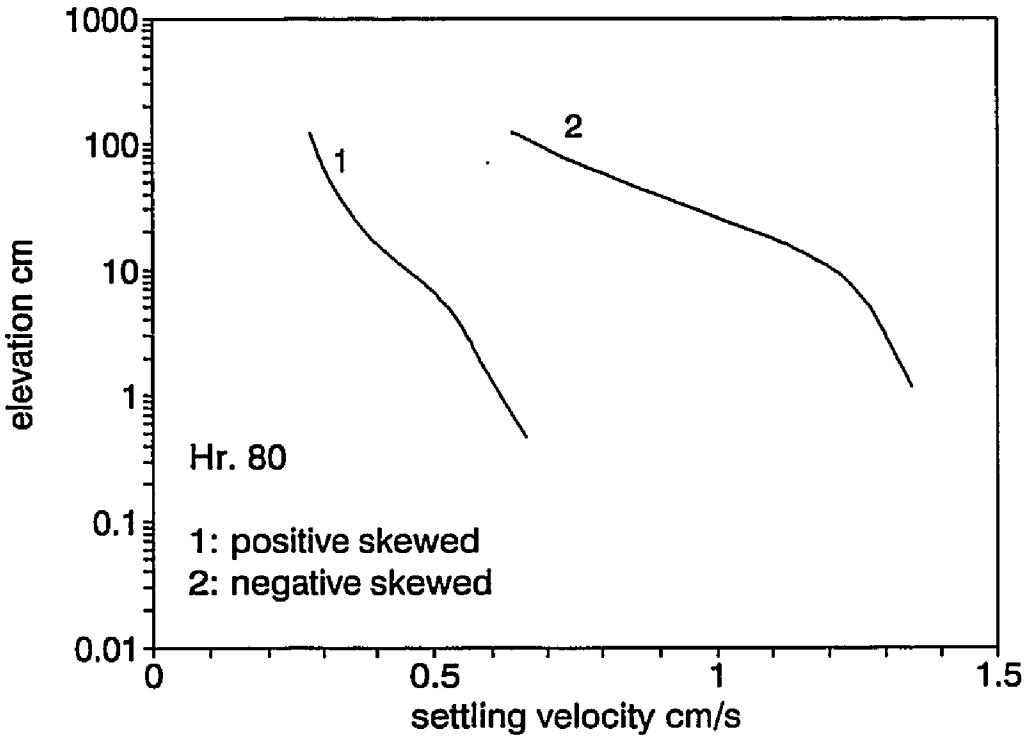
1000
100
10
1
0.1
0.01
elevation cm
0
0.5
1
1.5
settling velocity cm/s
1
2
Hr. 80
1: positive skewed
2: negative skewed

Figure 5.17 Calculated profiles of equivalent settling velocity under high energy condition showing the difference of the sediment composition effect due to different skewness.

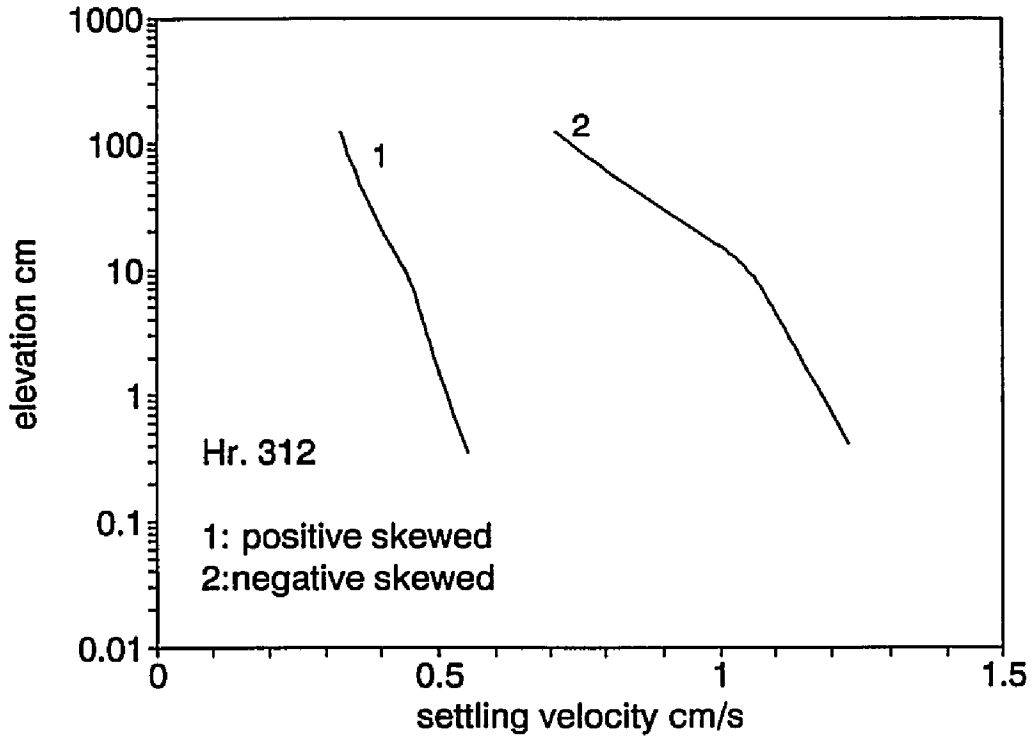
1000
100
10
1
0.1
0.01
elevation cm
0
0.5
1
1.5
settling velocity cm/s
1
2
Hr. 312
1: positive skewed
2:negative skewed

6. REFERENCE CONCENTRATION AND SUSPENSION COEFFICIENT

6.1 Introduction

As we stated at the end of Chapter 3, the suspension coefficient, γ_0, is the essential parameter to be determined in using the Smith and McLean's (1977a, 1977b) reference concentration model. This is because that C_b, the bed sediment concentration, normally is treated as a constant (=0.65) and S_n, the normalized excess shear stress can be calculated using a boundary layer model, e.g., Smith and McLean, 1977; Grant and Madsen, 1986; Madsen and Wikramanayake, 1991; etc. Many researchers have investigated and estimated γ_0 values through field and/or laboratory measurements. Smith and McLean (1977) gave $\gamma_0 = 2.4 \times 10^{-3}$ from their measurements in the Columbia river. Glenn (1983) analyzed the data of Kalkanis (1964) and Abou-Seida (1965) and derived a value of $\gamma_0 = 3 \times 10^{-3}$. Kim (1991) calculated the suspension coefficient using data observed from the Duck site during 1985 (storm) and 1987 (fair weather) and derived $\gamma_0 = 2 \times 10^{-3}$ for fair weather and $\gamma_0 = 3 \times 10^{-4}$ for storms. A survey by Drake and Cacchione (1989) showed a wide range in estimated values of γ_0 from as high as 1×10^{-2} (Kachel and Smith, 1986) to as low as about 1.5×10^{-5} (Wiberg and Smith, 1986; Sternberg et al, 1985; Hickey et al, 1986). A relation of suspension coefficient to excess shear stress which shows that γ_0 decreases as excess shear stress increases, was also reported (Drake and Cacchione, 1989; Vincent, et al 1991; Kim, 1991). In an independent analysis of the data from the peak of the 1991 Halloween storm, Madsen, et al (1993, in press) concluded that, under storm-induced sheet flow conditions,

$\gamma_0 = 10^{-4}$ with the reference elevation taken at 7 grain size diameters above the bed. In this chapter, an attempt is made to calculate the suspension coefficient using the wave-current boundary layer model (Madsen and Wikramanayake, 1991) and to apply this model to the concentration and hydrodynamics measurements listed in Table 2.1. Both the Grant and Madsen (1982) roughness model, equation (4.23), and the new roughness model, equation (4.34), are used in the calculations. This is because most investigators who observed the γ_0 - S_a relationship used the Grant and Madsen (1982) model and it has been shown of over-estimate the roughness under high energy conditions. It is expected that using the new roughness model could lead to a new γ_0 - S_a relationship.

6.2 Computation of resuspension coefficient

Two additional input variables are needed in the computation of the resuspension coefficient using the boundary layer model. These two measured variables are the sediment concentration C_s and the elevation z_s at which C_s was measured. The concentrations were measured using OBS sensors described in Chapter 2. The measured concentrations at two elevations (54 and 120 cm above the bottom, see Table 2.2) are used in the calculation for each data burst in Table 2.1.

The calculation procedure is similar to that discussed in Section 4.3. It starts by solving equation (4.27) to determine the skin friction factor f_w'. The skin friction factor is then used to calculate the skin friction and physical bottom roughness k_b using two roughness models, equations (4.23) and (4.34). Iterating k_b into equation (4.27) can bring out the solution of the total friction factor f_w which is then used to calculate the maximum wave shear velocity, the combined shear velocity, the current shear velocity and the maximum skin

friction shear stress. The reference concentration $C_m(z_0)$ can be derived from equation (3.62) by assuming the bed sediment concentration $C_b = 0.65$ and an initial suspension coefficient, e.g. 1×10^{-3}. Profiles of mean concentration is calculated using the solutions derived in chapter 3, equations (3.41), (3.45), and (3.55). Comparing the calculated concentration at z_a to the corresponding C_a in Table 2.2, and the resuspension coefficient is adjusted according to the difference between the calculated and measured concentrations at z_a. This procedure is repeated until the calculated concentration matches the measured C_a at elevation z_a. Having considered the fact that most resuspension coefficient values obtained by other investigators are estimated without involving the stratification and sediment composition effects, the calculations of γ_0 in this study also neglect the stratification and sediment composition effects in the hope of making our results comparable to others. Therefore, the main purpose here is to compare the performance of those two roughness models in the calculations of the resuspension coefficient. The weighted average grain size ($d=0.0117$ cm and $w_f=1.01$ cm/s) is used.

6.3 Results and discussions

The calculated γ_0 values using both the Grant and Madsen (1982) and the new roughness models are shown in Table 6.1 and Figure 6.1. At both elevations, γ_0 calculated using the two roughness models are very close to each other for the two low energy condition bursts (Hr80 and Hr104). This is because, as stated in Chapter 4, the sediment motion roughness is unimportant under low energy conditions and both roughness models produce similar roughness values. For the moderate and high energy conditions, the γ_0 values estimated from the two roughness models are different, and, γ_0 obtained using the new roughness model are higher than those obtained using the Grant and Madsen (1982) model.

Table 6.1 Calculated suspension coefficient (x 10^{-3}) using mean grain size.

		54 cm		120 cm		MEAN	
Hours	S_n	New	GM	New	GM	New	GM
80	0.43	3.97	3.92	3.08	3.03	3.53	3.48
104	0.36	3.03	3.00	2.96	2.91	3.00	2.96
248	1.72	6.47	5.71	5.29	4.55	5.88	5.13
256	3.11	8.41	5.25	13.00	7.38	10.70	6.32
264	4.21	4.47	2.24	4.78	2.24	4.63	2.24
272	4.97	3.59	1.69	2.46	1.10	3.01	1.40
296	12.38	1.21	0.33	0.89	0.21	1.05	0.27
304	10.84	2.49	0.58	2.22	0.44	2.36	0.51
312	12.61	1.76	0.47	1.31	0.30	1.54	0.39
320	13.43	1.86	0.46	1.88	0.39	1.87	0.43

New = the new roughness model

GM = the Grant and Madsen (1982) roughness model

Figure 6.1 Calculated suspension coefficients (γ_0) plotted vs normalized excess shear stress. Top: using measured concentration at 54 cm; Middle: using measured concentration at 120 cm; Bottom: mean values of γ_0. (□): using the new roughness model; (▲): using Grant and Madsen 1982 roughness model. Mean grain size is used.

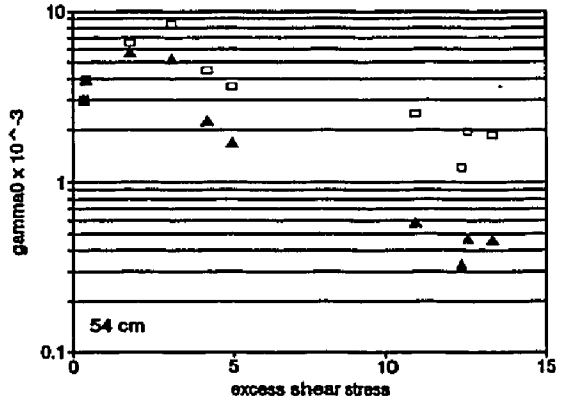
10
1
0.1
gamma0 x 10^-3
54 cm
0
5
10
15
excess shear stress

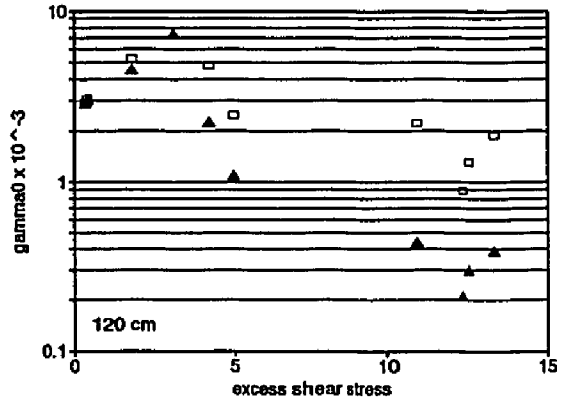
10
1
0.1
gamma0 x 10^-3
120 cm
0
5
10
15
excess shear stress

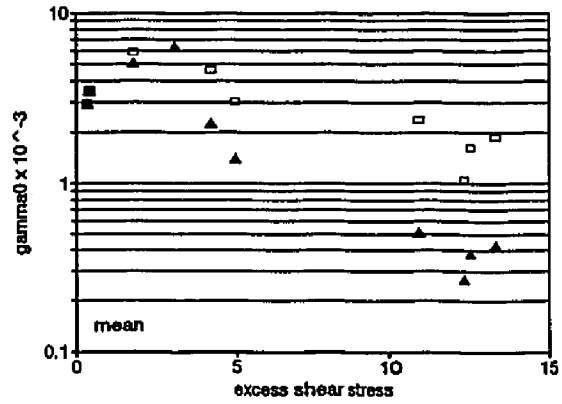
10
1
0.1
gamma0 x 10^-3
mean
0
5
10
15
excess shear stress

This difference is caused by the higher bottom roughness estimated by the Grant and Madsen (1982) roughness model. Suggestions by Cacchione and Drake (1990), and Madsen et al, (1993, in press) indicated that the Grant and Madsen (1982) model over-estimates the sediment motion roughness under high energy conditions. The over-estimate of the sediment roughness and, of course, the total roughness, results in an over-estimate of shear velocities. From the Rouse type equations in Chapter 5 and specifically, the Rouse number equation (5.3), we know that if the shear velocities are over-estimated, the Rouse number will be under-estimated. A smaller Rouse number will cause over-estimated concentration at each elevation. That is why the resuspension coefficient has to be reduced in order to match the calculated concentration to the measured concentration. Therefore, γ_0 is under-estimated when the grain and Madsen (1982) roughness model is used. Figure 6.1 plots the resuspension coefficients vs. the normalized shear stress S_n. The top panel shows the γ_0 calculated using the concentration measurements at 54 cm elevation, the middle panel shows γ_0 using the measurement at 120 cm elevation and the bottom panel shows the mean of those two. It is noticed that for γ_0 values obtained using both roughness models, there is a clear descending trend of γ_0 with increasing S_n. This descending trend reproduces the γ_0 - s_n relationship derived by other investigators (Drake and Cacchione, 1989; Vincent, et al, 1991; Kim, 1991) who also used the Grant and Madsen (1982) roughness model. The differences between the two γ_0 families is that the descending rate of γ_0 from the Grant and Madsen (1982) roughness model is higher than that of γ_0 from the new roughness model.

The γ_0 - S_n relation has been explained by Drake and Cacchione (1989). They suggested that: (1) the bed sediment concentration, C_b, may not be a constant; and (2) bed armoring or increasing substrate cohesiveness may make the bed sediment more difficult to

resuspend as shear stress increases and the bed is more intensively eroded. Besides these reasons, the effects of stratification and sediment composition (Chapter 5) may also contribute to the explanation of the γ_0 - S_n relation shown in Figure 6.1. As we have shown in Chapter 5, the combined effect of stratification and sediment composition changes the concentration profile in different manners under different energy conditions and at different elevations. Since the concentrations used in this chapter to estimate the resuspension coefficient are all from elevations above the wave boundary layer, we only discuss the variation of the concentration profiles due to the combined effect above the wave boundary layer. Under low energy condition, the effect of sediment composition outweighs the effect of stratification and causes a net increase of the calculated concentration (Figure 5.10). If both stratification and sediment composition were considered in the calculation of the γ_0, the estimated γ_0 values should be smaller than the values (Hr80 and Hr104) listed in Table 6.1. Under high energy condition, conversely, the stratification outweighs the effect of sediment composition and the combined effect causes a net decrease of the concentration. If both stratification and sediment composition effects were involved in the calculations of γ_0, the estimated γ_0 values should be greater than those (Hr296, Hr304, Hr312, and Hr320) in Table 6.1. The discussions above means that, besides the reasons indicated by Drake and Cacchione (1989) to explain the γ_0 - S_n relation, the neglect of both stratification and sediment composition effects may also be partially responsible for the descending resuspension coefficient with increasing normalized shear stress. Unfortunately, the boundary layer model in Chapter 3 is incapable of calculating the γ_0 values when both stratification and sediment composition effects are considered. This is because the iteration to compute the stability parameter does not converge when γ_0 is a variable. Without the converge of this iteration, the second iteration which computes the γ_0 does not work. Therefore, only qualitative explanations are shown here.

6.4. Computation of γ_0 using the concentration of silt and clay

Despite the fact that most γ_0 values are estimated using the mean grain size of the bottom sediments, a different approach is tried in this section. As we have noticed from Chapter 5, over 80% or more of the suspended sediments are silt and clay at the upper part of the water column. We also know from Chapter 2 that the OBS sensors were calibrated using only the finest grain size sediments. So, it is justified to calculate the resuspension coefficient by using the concentration profile of the silt and clay. The computing procedure is similar to that used in section 6.2, but the bed concentration is C_{bi} (= $f_i C_b$ = 0.2 C_b) instead of C_b(= 0.65). Because there are more clay and silt at higher elevations, only the measured concentration at 120 cm above the bottom is used in this calculation.

The estimated γ_0 values are listed in Table 6.2 and plotted in Figure 6.2. Comparing with the middle panel of Figure 6.1, it is noticed that the γ_0 values in Figure 6.2 are all smaller than those in Figure 6.1. For the 6 bursts of data under the low and moderate energy conditions, the γ_0 values estimated using the silt and clay (hereafter new γ_0 values) are on order smaller than those estimated using the mean grain size (hereafter old γ_0 values). This dramatic decrease of γ_0 is caused by using a different grain size (settling velocity). Under low energy conditions, when the current shear velocity is relatively small (1.92 cm/s for Hr.80), the settling velocity is an important factor to influence the Rouse number. When w_f = 0.26 cm/s (settling velocity of silt and clay) is used, the Rouse number is smaller and the concentration attenuation rate is smaller than when w_f = 1.01 cm/s (settling velocity of mean grain size) is used. For a fixed concentration measurement at 120 cm above the bottom, smaller reference concentration is needed to match the calculated concentration with the measured concentration. Given the shear stress and bed concentration, the smaller reference

concentration results in smaller resuspension coefficient. This is why the new values are much smaller than the old values under low and moderate energy conditions. Under high energy conditions, the new γ_0 values are also smaller than the old values, but the differences between them are not as large as under low and moderate energy conditions. For the 4 values calculated using the Grant and Madsen (1982) roughness model, there are very little differences between them. Under high energy conditions, the current shear velocities (4.98 cm/s from the Grant and Madsen (1982) roughness model and 3.51 cm/s from the new roughness model) are much higher. In this case, the Rouse number is always small no matter which grain size is used. Therefore, using different settling velocities under high energy conditions does not cause much differences in terms of the calculated concentration profiles. It is so especially when the Grant and Madsen (1982) roughness model is used. Because this model generates higher bottom roughness and higher shear velocity, the differences between the new and old γ_0 values are very small. The new roughness model generates relatively smaller shear velocity and, therefore, the differences between the new and old γ_0 values are more apparent. But, the magnitude of these differences are much smaller than those under low energy conditions.

In Figure 6.2, it is also interesting to see that the new γ_0 values do not decrease with increasing excess shear stress. 9 of 10 values scatter between 0.2×10^{-3} and 0.5×10^{-3}. This may imply that, for a certain grain size, the resuspension coefficient is not a function of the excess shear stress. Instead, the resuspension coefficient may only be related to the physical properties of the sediment.

Table 6.2 Calculated suspension coefficient (x 10^{-3}) using silt and clay.

		120 cm	
Hours	S_n	New	GM
80	1.24	0.29	0.29
104	0.12	0.11	0.11
248	3.25	0.48	0.48
256	5.43	0.52	0.47
264	7.16	0.39	0.34
272	8.34	0.35	0.31
296	19.92	0.28	0.21
304	17.52	0.44	0.32
312	20.29	0.40	0.30
320	21.57	0.51	0.38

New = the new roughness model

GM = the Grant and Madsen (1982) roughness model

Figure 6.2 Calculated suspension coefficients (γ_0) plotted vs normalized excess shear stress. The measured concentration at 120 cm is used. (□): using the new roughness model; (▲): using Grant and Madsen 1982 roughness model. Silt and clay is used.

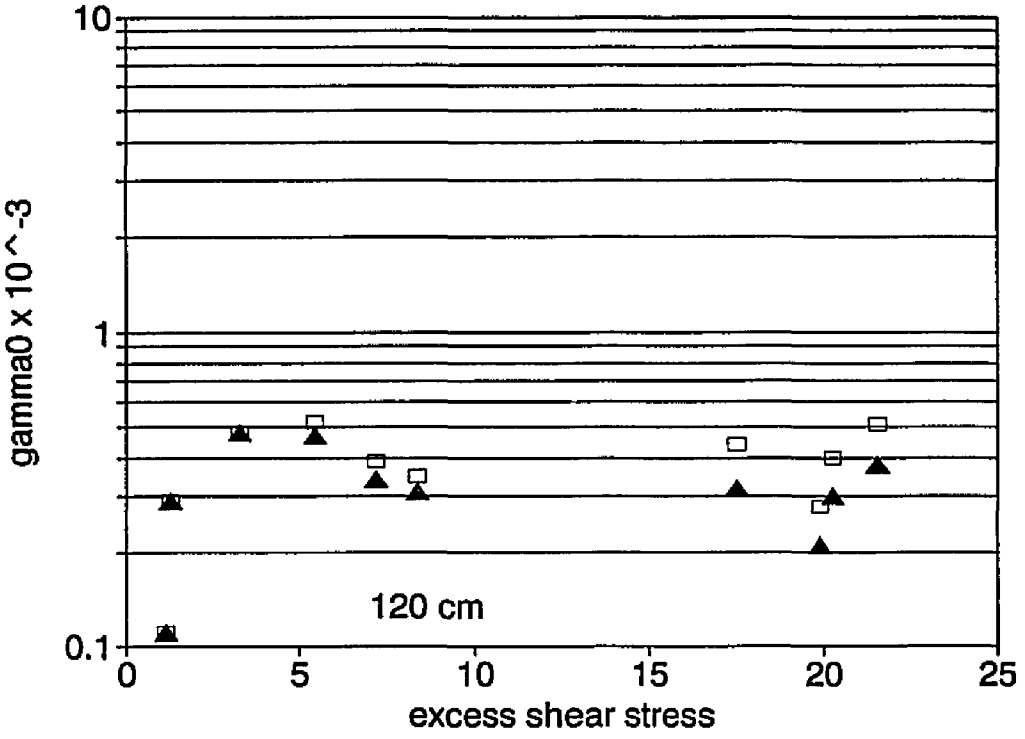
10
1
0.1
gamma0 x 10^-3
120 cm
0
5
10
15
20
25
excess shear stress

6.5. Summary

The resuspension coefficient γ_0 has been estimated by many investigators who present very different values. The differences could have been caused by several factors as follows: (1) different roughness models have been used; (2) the sediments composition which they used were different; (3) there were errors in the measurements; (4) the reference heights were different; (5) other factors. How important each factor is to the calculation of the resuspension coefficient is still not well known. However, we have seen from this chapter that roughness is an important factor in the γ_0 estimation. Since use of the Grant and Madsen (1982) roughness model over-estimates the bottom roughness under high energy conditions, the resuspension coefficient under high energy conditions is under-estimated. The γ_0 - S_n relation is reproduced when either the Grant and Madsen (1982) roughness model or the new roughness model is used to estimate the resuspension coefficient. The neglect of stratification and sediment composition effects may be also partially responsible for the decline in γ_0 with increasing excess shear stress. It is also important to know which grain size should be used in estimating the resuspension coefficient. This require the knowledge of the composition of the suspended and the bed sediments. Our limited data show that when a concentration above the wave boundary layer is used, the settling velocity of silt and clay, instead of the settling velocity of the mean grain size, should be used. The resuspension coefficient for the silt and clay may be a constant between 0.2×10^{-3} and 0.5×10^{-3}.

7. CONCLUSIONS

This thesis has studied three related subjects via the application of a wave-current-sediment boundary layer model and field data obtained from a deployment of the VIMS instrumented tripod during the 1991 Halloween storm. First, bottom roughness models were tested in Chapter 4 and a new roughness model was developed and tested. Secondly, the effect of both stratification and sediment composition on the concentration profiles were examined in Chapter 5. A qualitative relationship between these two effects was clarified. Finally, the resuspension coefficient was studied in Chapter 6. The major conclusions drawn from the study are as follows:

(1). It is shown in Chapter 4 that the roughness values used in boundary layer models are important in determining bottom shear stress, sediment suspension and wave energy dissipation. It is found that the Grant and Madsen (1982) roughness model over-estimates the sediment motion roughness under high energy conditions (storm) even though it can predict the ripple roughness under low and moderate energy conditions quite well. It is also found that the Madsen et al (1993, in press) roughness model, used only under high energy conditions, give the best prediction of concentration and velocity profiles compared to the measurements. Based on comparisons between the measured and calculated concentration as well as velocity profiles, a new roughness model, which combine the Grant and Madsen (1982) ripple roughness model and a new sediment motion roughness model, is established

(equation 4.34). The new roughness model is partitioned into three components: grain roughness, ripple roughness and sediment motion roughness. The sediment motion roughness is defined in such a way that it is proportional to the maximum skin friction Shields parameter. The calculated profiles of velocity and concentration using the new roughness model compared well to the measured concentration profiles under all energy conditions (measured velocity profiles are available only for 3 bursts of high energy conditions).

(2). It is shown in Chapter 5 that suspended sediment induced stratification reduces the mean concentration of suspended sediment above the wave boundary layer. Stratification can be neglected within the wave boundary layer. The magnitude of the reduction depends on the energy conditions. Under low energy conditions, stratification has much less effect on the profiles of sediment concentration than under high energy conditions. This is so because there is only a small amount of sediment induced stratification in the water column during fair weather because bottom sediments are hardly brought into suspension. Under high energy conditions, large amount of sediments are suspended and stable stratification appears. The reduction of the concentration due to the stratification increases with the energy condition. Whenever the stability parameter is greater than 0.03, ignoring the effect of stratification may cause some errors in the calculations of suspended sediment concentration profiles.

(3). Opposite to the effect of stratification, presence of multiple grain sizes generate higher calculated concentration than would prevail if a single grain size (e.g. the mean grain size) is used in the calculation (there is one special case when the multiple grain size concentration is lower under low energy condition, see the discussion in Section 5.3). This grain size effect always increases the concentration regardless of skewness of the grain size

distribution. The magnitude of this effect is also dependent on the energy conditions. Under low energy conditions, the concentration is sensitive to the Rouse number and the sediment composition effect can make considerable difference in the calculated concentration profiles. Ignoring the sediment composition effect may cause a considerable under-estimate of the suspended sediment concentration under low energy conditions. Under high energy conditions, however, the shear velocity is much greater than the settling velocity and the Rouse number is always small no matter what the settling velocities are. Therefore, sediment composition has less effects on the concentration profiles for high energy conditions.

(4). The skewness of grain size distribution does not change the sign of the sediment composition effect. For both positively and negatively skewed grain size distributions, the effect of sediment composition increases the sediment concentration relative to the single grain size prediction. However, since there is more finest (0.005 cm) sediment in positively skewed sediment than in negatively skewed sediment, the effect of sediment composition is stronger when the grain size distribution is positively skewed than negatively skewed.

(5). Stratification and sediment composition are opposing effects. Which effect is dominant depends on the energy condition. Under low energy conditions, the effect of sediment composition outweighs the effect of stratification. Under high energy conditions, this relation is reversed.

(6). It is shown in Chapter 6, and supported by other investigations (Drake and Cacchione, 1989; Madsen et al, 1993, in press) that because use of the Grant and Madsen (1982) roughness model over-predicts the bed roughness under high energy condition, the

resuspension coefficient will be under-predicted when this roughness model is used. This under-prediction of suspension coefficient under high energy condition appears to contribute to the formerly claimed relation that shows the suspension coefficient decreases with increasing excess shear stress.

(7). Since both the stratification and sediment composition affect the calculation of suspended sediment concentration profile, they also affect the estimate of the resuspension coefficient when the concentration profile technique is used in calculating the γ_0. The effects of stratification and sediment composition on the suspended sediment concentration may also be responsible to the decline of γ_0 with increasing excess shear stress. Under low energy conditions, the combined effect of stratification and sediment composition increases the concentration. Smaller reference concentration (and smaller γ_0) is needed to match the calculated and measured concentration at a certain elevation above the wave boundary layer. Therefore, neglecting the combined effect will create over-estimated values. Under high energy conditions, conversely, the combined effect will reduce the calculated concentration. So, γ_0 value will be under-estimated if the effect is ignored.

(8). If the concentration profile technique is used in estimating the resuspension coefficient, it is important to know which grain size (settling velocity) should be used in the calculations. Unless the bottom sediment contains only one grain size, the percentage of each grain size in suspension needs to be determined. When one grain size is dominant at the elevation where the measurement is made, it is suggested that this dominant grain size should be used in calculating the resuspension coefficient.

(9). When the settling velocity of silt and clay (which are dominant at the elevation (120 cm) where OBS sensor is located) is used, the calculated γ_0 values are no longer a function of the excess shear stress. This may indicate that the resuspension coefficient is only a function of the sediment itself. Our limited data shows that $\gamma_0 = 0.2 \sim 0.5 \times 10^{-3}$ for the silt and clay.

Our understanding of sediment resuspension and suspended sediment concentration profiles in the bottom boundary layer has been increased through this, and many others, combined field experiments and modeling research. It is the author's hope that this increased understanding can be used to help design future field experiments and modeling works. One fundamental problem in suspended sediment research is the resuspension of the bottom sediment within the bottom boundary layer. Because of the limitation of the instruments available, the resuspension studies are still at the stage of combined theoretical model (e.g., Smith and McLean, 1977) and measurements some distance above the bottom. If the model were "correct", the accuracy of measurements becomes crucial. This measurement, normally way above the bottom, is used to create the reference concentration. How accurate the measurements are depends on the calibration of the instruments (OBS) used in the measurements. As stated in Chapter 2, the response of OBS to suspended sediment concentration is influenced by the sediment composition. Therefore, OBS, or other similar instruments, calibrations should include the effects of sediment composition in order to have accurate measurements in natural environments.

In creating the reference concentration by using a measurement some distance above the bottom, the Rouse type equation is used. Effects of stratification and sediment

composition need to be considered unless the measurement is made within the wave boundary layer where the stratification effect may be ignored and the effect of sediment composition is also relatively small. Otherwise, the reference concentration will be either over-estimated (if sediment composition effect is ignored) or under-estimated (if stratification effect is ignored). It may be necessary in the future to measure the composition of suspended sediments directly. If so, the sediment composition effect on the concentration profile can be treated more accurately than modeling the suspended sediment composition as in Chapter 5.

One question needing to be addressed in the future suspended sediment transport studies is how the resuspension coefficient is associated with the shear stress and sediment physical properties (e.g., grain size, density, etc.). Results from this study have shown two patterns of γ_0 values. One is that γ_0 is a function of shear stress, i.e., γ_0 decreases with increasing excess shear stress, when the mean grain size is used in estimating the γ_0 values. Another pattern indicates that the resuspension coefficient does not show a clear trend to vary with the shear stress and its values are scattered in a 'constant' range. The latter pattern is obtained when the settling velocity of silt and clay is used in the calculations. Although these two results conflict to each other, they may show us the way on which the future study should go. As explained in Chapter 6, the 'constant' γ_0 values for the silt and clay may be more applicable because the OBS sensors were calibrated using the fine fraction. Our model results in Chapter 5 also show that silt and clay are dominant at the elevation where the OBS is located. This means that the grain size plays an important role. If a constant γ_0 value is appropriate for silt clay, how will the γ_0 values be for other grain sizes? Are they also constants? Are these constants equal to each other? If they are different, do they need to be treated separately in calculating the concentration? Laboratory and field experiments as well

as modeling studies are needed in order to answer these questions. The answers, if achievable, would be significant in understanding the sediment resuspension in a natural multiple grain size environment. It is more so when the bottom sediments are interbedded and each layer has a different sediment grain size distribution.

LITERATURE CITED

Abou-Seida, H. M., Bedload function due to wave action. Rep. HEL-2-11, Hydraul. Eng. Lab., Univ. California, Birkeley, California, 78pp, 1965.

Adams, C. E., and G. L. Weatherly, Some effects of suspended sediment stratification on an oceanic bottom boundary layer, J. Geophys. Res., 86, 4161-4172, 1981.

Bailard, J. A., An energetics total load sediment transport model for a plane sloping beach. J. Geophys. Res., 86, 10938-10954, 1981.

Bailard, J. A., Modeling on-offshore sediment transport in the surfzone, Coastal Eng., 1981, ASCE, 1419-1438, 1982.

Bailard J. A. and D. L. Inman, An energetics bedload model for a plane sloping beach; local transport. J. Geophys. Res., 86, 2035-2043, 1981.

Bijker, E. W., Longshore transport computations, Proc. ASCE, J. Waterways, Harbors and Coastal Eng. Div., 97, 687-701, 1971.

Birkemeier, W. A., A. W. DeWall, C. S. Corbics and H. C. Miller, A user's guide to C.E.R.C.'s Field Research Facility, U.S. Army Corps of Engineers, CERC, MR 87-7, 1981.

Birkemeier, W. A., H. C. Miller, S. D. Eilhelm, A. W. DeWall, and C. S. Corbics, A user's guide to the Coastal Engineering Research Center's (CERC's) Field Research Facility, Instruction Rep. CERC-85-1, U.S. Army Corps of Engineers, Waterways Ecpert. Station, Vicksburg, Miss. 121pp, 1985.

Bowen, A., Simple models of nearshore sedimentation; beach profiles and longshore bars. (ed. by McCann, S. B.) The coastaline of Canada, Geol. Surv. of Canada, paper 80-10, 1-11, 1981.

Brevik, I., Oscillatory rough turbulent boundary layers. J. Waterways, Port, Coastal and Ocean Div., ASCE, 107, 175-188, 1981.

Carstens, M. R., F. M. Neilson, and H.D. Altinbilek, Bed forms generated in the laboratory under and oscillatory flow: analytical and experimental study, TM-28, U.S. Army Corps of Engineers, Coastal Engineering Research Center, 1969.

Christofferson, J. B. and I. G. Jonsson, Bed friction and dissipation in a combined current and wave motion, Ocean Eng., 12, 3887-423, 1985.

Coleman, N. L., Discussion: Velocity profiles with suspended sediment, J. Hydraul. Res., 22, 263-289, 1984.

Davis, A. G., R. L. Soulsby and H. L. King, A numerical model of the combined wave and current bottom boundary layer, J. Geophys. Res., 93, 491-508, 1988.

Diaz R. J. and L. C. Schaffner, Comparison of sediment landscapes in Chesapeake Bay as seen by surface and profile imaging, In: Understanding the Estuary, Advances in Chesapeake Bay Research (ed. by Lynch, M. P. and E. C. Krome), Chesapeake Bay Res. Consortium, CBP/TRS, 24/88, 222-240, 1988.

Dingler, J. R., Wave formed ripples in nearshore sands, Ph.D. thesis, University of California, San Diego, 1974.

Drake, D. E. and D. A. Cacchione, Estimates of the suspended sediment reference concentration (C_a) and resuspension coefficient (γ_0) from near-bottom observations on the California shelf, Continental Shelf Res., 9(1), 51-64, 1989.

Glenn, S. M., A continental shelf bottom boundary layer model: The effects of waves, currents, and a movable bed, Sc.D. thesis, 237pp., Mass. Inst. of Technol., Cambridge, 1983.

Glenn, S. M. and W. D. Grant, A suspended sediment stratification correction for combined wave and current flows, J. Geophys. Res., 92, 8244-8264, 1987.

Goda, Y., Random seas and design of maritime structure, Univ. Tokyo Press, 1985.

Grant, W. D. and O. S. Madsen, Combined wave and current interaction with a rough bottom, J. Geophys. Res., 84, 1797-1808, 1979.

Grant, W. D. and O. S. Madsen, Movable bed roughness in unsteady oscillatory flow, J. Geophys. Res., 87, 469-481, 1982.

Grant, W. D. and O. S. Madsen, The continental shelf bottom boundary layer, Annu. Rev. Fluid Mech., 18, 265-305, 1986.

Green, M. O., Low-energy bedload transport by combined wave and current flow on a southern Mid-atlantic Bight shoreface, Ph.D Thesis, The College of William and Mary. 162 pp, 1987.

Hickey, B. M.,E. T. Baker and N. B. Kachel, Suspended particle movement in and around Quinault submarine canyon, Mar. Geol., 71, 35-83, 1986.

Inman, D. L., Wave generated ripples in nearshore sands, TM-100, U.S. Army Corps of Engineers, Bash Erosion Board, 1957.

Inman, D. L. and R. A. Bagnold, Beach and nearshore processes. Part II. Littoral processes. (ed. by Hill, M. N.) The Sea, Interscience, vol. 3, 529-553, 1963.

Jonsson, I. G., Wave boundary layer and friction factors, Proc. 10th Coast. Eng. Conf., ASCE, 127-148, 1966.

Kachel, N. B. and J. D. Smith, Geological impact of sediment transporting events on the Washington Continental Shelf. (ed. by Knight, R. J. and McLean, J. R.) Canadian Soc. Petroleum Geologist, Memoir II, 145-162, 1986.

Kajiura, K., On the bottom friction in an oscillatory current, Bull. Earthquake Res. Inst., Univ. Tokyo, 42, 147-174, 1964.

Kajiura, K., A model of the bottom boundary layer in water waves, Bull. Earthquake Res. Inst., Japan, vol. 46, 75-123, 1968.

Kalkanis, G., transportation of bed material due to wave action. Tech. Memo. No. 2, U.S. Army Corps of Engineers, coastal Eng. Res. Center, 38 pp, 1964.

Katori, S., A. Watanabe, and K. Horikawa, Laboratory study on sediment movement in the sheet flow regime, Coast. Eng. Japan, 24, p235, 1981.

Kim, S. C., Inner continental shelf benthic boundary layer dynamics and suspended sediment transport, Ph.D. thesis, Va. Inst. of Mar. Sci. Gloucester point, 1991.

Kineke, G., and R. sternberg, The effect of particle settling velocity on computed suspended sediment concentration profiles, Mar, Geol., 90, 159-174, 1989.

Komar, P. D., Boundary layer flow under steady unidirectional current, In: Marine Sediment Transport and Environment Management (ed. by Stanley, D. J. and D. J. P. Swift), Wiley-Intersciences, New York, 91-106, 1971.

Komar, P. D., Beach sand transport: distribution and total drift, Proc. ASCE, J. Waterways, Port, Coastal and Ocean Div., 103, 225-239, 1977.

Kundu, P. K., Fluid mechanics, Academic Press, Inc., San Diego, California, 1990.

Lofquist, K. E. B., Sand ripple growth in an oscillatory flow water tunnel, TP-78-5, U.S. Army Corps of Eng., CERC, 1140-1151, 1978.

Lumley, J. L., Two-phase and non-Newtonian flows, Top. Appl. Phys., 12, 289-324, 1978.

Lundgren, H., Turbulent currents in the presence of waves, Proc. 13th Int'l. Conf. Coastal Eng., Vancouver, 623-634, 1972.

Madsen, O. S. and W. D. Grant, Quantitative description of sediment transport by waves, Proc. 15th International Conf. on Coastal Engineering, ASCE, 2:1093-1112, 1976.

Madsen, O. S. and P. N. Wikramanayake, Simple model for turbulent wave-current bottom boundary layer flow, Rep. DRP-91- , 150pp., Ralph M. Parsons Laboratory, MIT, Cambridge, Ma., 1991.

Madsen, O. S., L. D. Wright, J. D. Boon, and T. A. Chisholm, Wind stress, bed roughness, and sediment suspension on the inner shelf during an extreme storm event, 1993, (in press).

Mason, C., W. A. Birkemeier and P. A. Howd, Overview of Duck85 nearshore processes experiment. (ed. by Kraus, N.) Coastal sediments '87, ASCE, 818-833, 1987.

Mathisen, P. P., Experimental study on the response of fine sediments to wave agitation and associated wave attenuation, M.S. Thesis, MIT, 1989.

McLean, S. R., On the calculation of suspended load for noncohesive sediments, J. Geophys. Res., 97, 5759-5770, 1992.

Miller, M. C. and P. D. Komar, Oscillation sand ripples generated by laboratory apparatus, J. Sed. Petro., 50, 173-182, 1980a.

Miller, M. C. and P. D. Komar, A field investigation of the relationship between oscillation ripple spacing and the near-bottom water orbital motion, J. Sed. Petro., 50, 183-191, 1980b.

Myrhaug, D., On a theoretical model of rough turbulent wave boundary layers, Ocean Eng., 9, 547-565. 1982.

Nielsen, P., A note on wave ripple geometry, Prog. Rep., 43, 17-22, Tech. Univ. Denmark, Lyngby, 1977.

Nielsen, P., Some basic concepts of wave sediment transport, Series paper No. 20, Inst. of Hydrodynamics and Hydraulic Eng., Technical University of Denmark, 1979.

Nielsen, P., Dynamics and geometry of wave generated ripples, J. Geophys. Res., 86, 6467-6472, 1981.

Nielsen, P., Explicit formulae for practical wave calculations, Coastal Eng., 6, 389-398, 1982.

Nielsen, P., Entrainment and distribution of different sand sizes under water waves, J. Sed. Petrol., 53, 423-428, 1983.

Nielsen, P., Field measurements of the time-averaged suspended sediment concentration under waves, Coastal Eng., 8, 51-72, 1984.

Nielsen, P., On the structure of oscillatory boundary layers, Coastal Eng., 9(3), 261-276, 1985.

Nielsen, P., Local approximations: a new way of dealing with irregular waves, Proc. 20th Int'l, Conf. on Coastal Eng., Taipei, 1986.

Nielsen, P., Coastal bottom boundary layer and sediment transport, Vol. 4 of Advanced Series on Ocean Engineering, (editor-in-chief Philip L-F Liu), World Scientific Publishing, Singapore, 1992.

Owen, P. R., Saltation of uniform grains in air, J. Fluid Mech., 20, 225-141, 1964.

Rosengaus, M., Experimental study on wave generated bedforms and resulting wave attenuation, Ph.D. Thesis, MIT, 1987.

Rouse, H., Experiments on the mechanics of sediment suspension. (ed. by Hartog, J. P. D. and Peters, H.) Proc. 5th Int'l Congr. for Applied Mech., Wiley and Sons, New York, 550-554, 1939.

Sato, S. and K. Horikawa, Sand ripple geometry and sand transport mechanism due to irregular flows, Proc. 21st Coastal Eng. Conf., 1748-1762, 1988.

Shi, N. C., L. H. Larsen and J. P. Downing, Predicting suspended sediment concentration on continental shelves, Mar. Geol., 62, 225-275, 1985.

Smith, J. D., Modeling of sediment transport on continental shelves, in The Sea, Vol. 6, edited by E. D. Goldberg, I. N. McCave, J. J. O'brien, and J. H. Steele, pp. 539-577, Interscience, New York, 1977.

Smith, J. D. and S. R. McLean, Spatially averaged flow over a wavy surface, J. Geophys. Res., 82, 1735-1746, 1977a.

Smith, J. D. and S. R. McLean, Boundary layer adjustments to bottom topography and suspended sediment, in Bottom Turbulence, edited by J. C. J. Nihoul, pp. 123-151, Elsevier, New York, 1977b.

Sternberg, R. W., D. A. Cacchione, D. E. Drake and K. Kranck, Suspended sedient transport in an estuarine tidal channel in San Francisco Bay, California, Mar. Geol., 63, 331-361, 1985.

Swart, D. H., Coastal sediment transport: Computation of longshore transport, Rep. No. R968, Delft Hydr. Lab., Netherland, 61pp, 1976.

Tanaka, H. and H. Shuto, Friction for a wave-current coexisting system, Coastal Eng. Japan, 24, 105-108, 1981.

Taylor, P. A., and K. R. Dyer, Theoretical models of flow near the bed and their implications for sediment transport, in The Sea, vol. 6, edited by E. D. Goldberg, I. N. McCave, J. J. O'Brien, and J. H. Steele, pp. 579-601, Interscience, New York, 1977.

Thornton, E. B., Distribution of sediment transport across the surfzone, Proc. 13th Int'l. Coastal Eng. Conf., Vancouver, ASCE, 1049-1068, 1973.

Vanoni, V. A., Transportation of suspended sediment by water, Trans. ASCE, III, 67-133, 1946.

Vincent, C. E., R. A. Yong and D. J. P. Swift, Bed-load transport under waves and currents, Mar. Geol., 39, 71-80, 1981.

Vincent, C. E., and M. O. Green, Field measurements of the suspended sand concentration profiles and fluxes and of the resuspension coefficient γ_0 over a rippled bed, J. Geophys. Res., 95, 11591-11601, 1990.

Vincent, C. E., D. M. Hanes, and A. J. Bowen, Acoustic measurements of suspended sand on the shoreface and the control of concentration by bed roughness, Marine Geology, 96, 1-18, 1991.

Wiberg, P. L. and J. D. Smith, A comparison of field data and theoretical models for wave-current interactions at the bed on the continental shelf, Cont. Shelf Res., 2, 126-136, 1983.

Wiberg, P. L. and J. M. Nelson, Unidirectional flow over asymmetric and symmetric ripples, J. Geophys. Res., 97, 12745-12761, 1992.

Wikramanayake, P. N. and O. S. Madsen, Calculation of movable bed friction factors, Rep. XXXXX 105pp. Ralph. M. Parsons Laboratory, MIT, Cambridge, Ma., 1991.

Wilson, K. C., Bed-load transport at high shear stress, ASCE J. Hydraulics Div., 92 (HY6), 49-59, 1966.

Wilson, K. C., Friction behavior of sheet flow, Progress Report No. 67, Inst. Hydrodynamics and Hydraulic Eng., Technical University of Denmark. 1988.

Wilson, K. C., Friction of wave-induced sheet flow, Coastal Eng., 12, 371-379, 1989.

Wright, L. D., J. D. Boon, M. O. Green and J. H. List, Response of the mid shoreface of the southern Mid-Atlantic Bight to a "Northeaster", Geo-Mar. Let., 6, 153-160, 1986.

Wright, L. D., J. D. Boon, S. C. Kim, and J. H. List, Modes of cross-shore sediment transport on the shoreface of the Middle Atlantic Bight, Marine Geology, 96, 19-51, 1991.

Wright, L. D., J. D. Boon, J. P. Xu, and S. C. Kim, The bottom boundary layer of the bay stem plains environment of lower Chesapeake bay, Estuarine, Coastal and Shelf Science, 35, 17-36, 1992.

Yalin, M. S., An expression for bedload transportation, Proc. ASCE, J. Hydr. Div., 89, 221-250, 1963.

Yalin, M. S., Mechanics of sediment transport. 2nd ed., Pergamon Press, Oxford, U.K., 290pp., 1977.

VITAE

Jingping Xu

Born in Shandong, China on January 14, 1963. Entered Shandong College of Oceanography (currently called Ocean University of Qingdao - What a change! Sound like a Community college now. Is UNIVERSITY necessarily better than COLLEGE?) to study Marine Geology in 1980. Graduated with a B.S. in 1984 and a M.S. in 1987. Employed by the Institute of Environmental Protection, State Oceanic Administration, as a research assistant for one year. Came to Virginia Institute of Marine Science for the Ph.D. program in January 1989.